Computational Studies of Model Glass-Forming Systems

Zane Shi

A Dissertation
Presented to the Faculty
of Princeton University
in Candidacy for the Degree
of Doctor of Philosophy

Recommended for Acceptance
by the Department of
Physics
Adviser: Pablo Debenedetti

June 2014

Abstract

This dissertation presents a collection of computational studies of model supercooled and glass-forming systems. In Chapter 2, we present a family of systematically softened potentials based on the well-known Lennard-Jones potential, and investigate how perturbations to the repulsive exponent can affect the thermodynamic and dynamic properties of a system. The softer liquids have markedly higher entropies and lower Kauzmann temperatures than their Lennard-Jones counterparts, and remain diffusive down to appreciably lower temperatures. Chapter 3 provides a critical analysis of the validity of using a relaxation time as a substitute for viscosity when studying Stokes-Einstein behavior in simulations. For both model atomic (family of softened potentials) and molecular (Lewis and Wahnström model of *ortho*-terphenyl) systems, the validity of this substitution, and assumption of the interchangeability of different relaxations times, are strongly challenged. Chapter 4 contains a comprehensive study of the viscosity of the SPC/E model of water. We map the anomalous region for viscosity (decrease of viscosity upon compression) on the (ρ, T) plane, and extend the discussion of Chapter 3 by applying a similar analysis to water. We also present two studies of properties of free-standing films. Films composed of the binary Lennard-Jones glass-forming mixture (Chapter 5) exhibit substantial compositional inhomogeneity, while films composed of rigid Lewis and Wahnström *ortho*-terphenyl molecules (Chapter 6) show oscillatory orientational preferences induced by the surface. In all cases, diffusivity at the surface is greatly enhanced relative to the interior. Additionally, we perform an energy landscape analysis of these films, and find that molecules at the surface are able to sample the underlying energy landscape more effectively than those in the interior.

Acknowledgements

This dissertation represents the culmination of my graduate studies, and also of my academic career as a whole. Reflecting back, the path to this point, as with any journey though life, has been extensive and non-linear. I want to thank everyone who helped me along the way.

First and foremost, I must thank my advisor, Professor Pablo Debenedetti. His guidance and support have been invaluable throughout my graduate research. His kindness, dedication, and professionalism are inspiring to all of his students. I am truly honored to be able to call Pablo my advisor, my collaborator, and my friend. I would also like to thank Dr. Frank Stillinger, who I was fortunate enough to collaborate with on many of my research projects. To say that Frank is a brilliant scientist is simply greatly conservative, and my projects have benefited immensely from his unique prospectives and creative insights. I can say with certainty that my graduate research was enriched from his involvement.

The PGD research group is a great group to be a part of. I would like to thank Frank Ricci, Harold "Wick" Hatch, Jeremy Palmer, Sumit Sharma, Yang Liu, Amir Haji-Akbari, Sapna Sarupria, Kevin Daly, Santiago Romero, Sang Beom Kim, Elia Altabet, and all the other members of the PGD group that I have met over the years for the numerous useful discussions we had. I also want to acknowledge in particular two then Senior Thesis students, Paul Ginart and Victoria Hwang, who worked on topics closely related to my research. Paul obtained preliminary results on the family of systematically softened potentials, while Victoria was a co-investigator on the study of water viscosity. As undergraduates, Paul and Victoria were both very impressive in the quality and professionalism of their work, and it was a pleasure to work with them both.

From grade school through graduate school, I have been extremely fortunate to have met some of the most excellent teachers. For my undergraduate physics education, I want to thank in particular Professor Wu Hai-Sheng of Minnesota State University, Mankato, and Professors S. Lance Cooper, Russ Giannetta, and Kevin Pitts of the University of Illinois at Urbana-Champaign. While this is a physics Ph.D. dissertation, I think back to the very beginnings of my formal schooling, and I must honor here my first Chinese language teacher, Mrs. Wu Hui Juan. As I spent the bulk of my early childhood in the United States, when I returned to China for grade school after the passing of my father, I spoke and understood very little Chinese. About to enter third grade in the highly competitive and rigorous Chinese grade school system, my language skills were very lacking. In fact, the very first language teacher that I was assigned to did not even want me in her class, fearing that I would bring down the class average. Mrs. Wu not only took me in her class, but also provided me

with crucial private tutoring to catch up with the rest of the students. The time I spent learning from her laid the foundations for the rest of my academic career. By all standards, Mrs. Wu is a model teacher and an extraordinary educator, and certainly she should share in the accomplishment of this dissertation.

I want to thank my family and friends. It was my mother who encouraged me to take my first physics course when I entered high school, and correctly predicted that I would absolutely love it. She has always been supportive of whatever I do. I am also grateful for the support from my extended family in Shanghai, particularly my grandparents. I know they care about me greatly. My dearest friends, from Shanghai, from Minnesota, from Illinois, and from Princeton, I will always hold them close to my heart.

Finally, I want to take a moment to remember my late father, Wen-Zhong Shi, who passed away well too young, at age thirty-four. By all accounts, he had a brilliant mind and was a good man. As I approach closer to the age of his passing, I realize more and more just how tragic of a loss this was to all who knew him. I can only wish that I knew him better, but he inspires me eternally, and I hope he would be proud.

To my father.

Contents

List of Tables

List of Figures

Chapter 1

Introduction

As computer hardware becomes exponentially more powerful[1], computational research has emerged as an increasingly important tool to study liquid and amorphous states. These computational studies fall between what is commonly considered theoretical and experimental research. On the one hand, simulations, when considered as a computational "experiment", can provide numerical solutions to large-scale, multi-bodied problems to which no exact analytical solutions exist. On the other hand, when used as a modeling tool to approximate real experimental data, simulations can provide a molecular level understanding of the particular laboratory result. Indeed, computational studies complement both theoretical modeling and experimental observation.

This dissertation presents a collection of computational studies of model supercooled and glass-forming systems. These studies can be divided into two general categories. The first set, consisting of three studies (Chapters 2, 3, and 4), explores in depth the bulk thermodynamic and dynamic properties of a number of model systems of increasing complexity. The second set, consisting of two studies (Chapters 5 and 6), focus on the properties of free-standing films. In the following sections of this introductory chapter, we provide the motivations and background for each of these studies.

1.1 Computational Modeling: Tuning an Interaction

The well-known Lennard-Jones potential, given by

$$\phi^{LJ}(r) = 4\epsilon \left[\left(\frac{\sigma}{r}\right)^{12} - \left(\frac{\sigma}{r}\right)^{6} \right], \tag{1.1}$$

approximates the interaction between a pair of neutral atoms (Figure 1.1, magenta line). It is characterized by a steep r^{-12} short range repulsion and gradual r^{-6} long range attraction. ϵ corresponds to the well depth, while σ gives the distance where the potential is zero. When used to model a given experimental system, the two parameters ϵ and σ are fitted to reproduce experimental data.

The r^{-6} long range attractive term in Eq. 1.1 is physically justified as having the same r dependence as the London dispersion forces[2]. However, the r^{-12} repulsive term, which describes the short range Pauli repulsions, has no theoretical justification[2]. The exponent of this r^{-12} term is chosen primarily for computational efficiency, as r^{-12} is simply the square of r^{-6}.

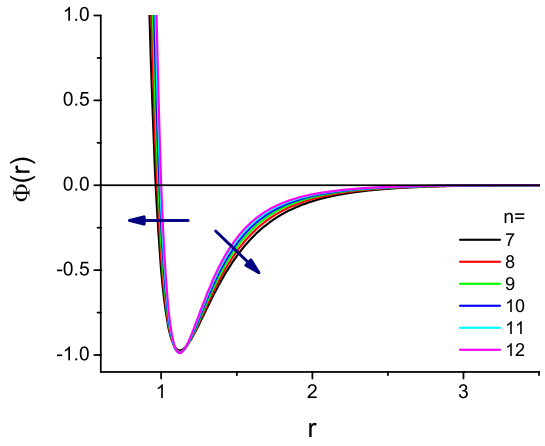

Figure 1.1: The family of "softened" potentials used in Chapter 2. The arrows show the effect of softening.

To date, relatively few investigations have explored systematically the effects of changes in specific features of the interaction potential upon viscous liquid behavior. Specifically, the effects of systematically varying the repulsive force have not been studied. Computational studies are ideally suited to study this type of systematic perturbation of a single variable, as this level of specificity is generally not possible in experiments. In Chapter 2, we create a family of generalized $(n, 6)$ potentials (Figure 1.1),

$$\phi = 4\epsilon \left[\lambda \left(\frac{\sigma}{r} \right)^n - \alpha \left(\frac{\sigma}{r} \right)^6 \right], \tag{1.2}$$

where

$$\lambda = \frac{3}{2} \left(\frac{2^{\frac{n}{6}}}{n-6} \right) \qquad \alpha = \frac{n}{2(n-6)}. \tag{1.3}$$

These potentials can be viewed as a perturbation of the standard $(12, 6)$ Lennard-Jones potential. The repulsive exponent is chosen to range from 7 to 12, and λ and α are chosen such that the well

depth and location coincide across all exponents. In effect, the potential is "softened" as the exponent is decreased. For potentials described by Eq. 1.2, $n = 7$ is the lowest integer value that maintains a simple power law repulsive term. Although the limit of Eq. 1.2 as $n \to 6$ is well behaved and can be obtained by L'Hôpital's rule, the functional form of the repulsive term in this $n = 6$ case becomes $(\frac{\sigma}{r})^6 \ln(\frac{\sigma}{r})$.

Our constructed potentials thus allow us to tune one particular feature of the molecular interaction, the repulsive exponent, or "softness", and study the thermodynamic and dynamic properties as a function of this softness. Over the range of conditions examined, we find only modest dependence of structure on softness. In contrast, decreasing the repulsive exponent from $n = 12$ to $n = 7$ causes the diffusivity to increase by as much as two orders of magnitude at fixed temperature and density, and produces mechanically stable packings (inherent structures) with cohesive energies that are, on average, ca. 1.7 well depths per particle larger than for the corresponding Lennard-Jones ($n = 12$) case. The softer liquids have markedly higher entropies and lower Kauzmann temperatures than their Lennard-Jones ($n = 12$) counterparts, and they remain diffusive down to appreciably lower temperatures. We also find that softening leads to a modest increase in fragility.

1.2 The Stokes-Einstein Equation

In 1851, George Gabriel Stokes derived the drag force, $\mathbf{F}_d$, on a small spherical particle of radius a traveling with velocity $\mathbf{v}$ in a viscous fluid of viscosity η[3]:

$$\mathbf{F}_d = -6\pi\eta a\mathbf{v} = -b\mathbf{v}. \tag{1.4}$$

This is now known as Stokes' law, and $b = 6\pi\eta a$ is the drag coefficient of this velocity-dependent force. Note that while Stokes assumes a no-slip boundary condition at the particle-fluid interface, for a slip boundary condition, the constant 6π in Eq. 1.4 is simply replaced by 4π[4].

The Einstein relation, first presented by Albert Einstein in his papers on Brownian motion in 1905[5], states that for particles suspended in a fluid,

$$D = \mu k_B T. \tag{1.5}$$

Here, D is the diffusion coefficient of the particles, T is the temperature, and k_B is Boltzmann's constant. μ is the mobility coefficient, defined as the ratio of the drift velocity to an applied force,

i.e., $\mu = v/F_d = 1/b$.

Thus, for small spherical objects suspended in a viscous fluid, we can combine Stokes' Law (Eq. 1.4) and the Einstein relation (Eq. 1.5), and obtain the well-known Stokes-Einstein equation,

$$D = \frac{k_B T}{6\pi\eta a}. \tag{1.6}$$

It is important to note that this original derivation describes two interacting components: D and a are properties of the spherical objects in suspension, while T and η are properties of the surrounding fluid.

However, for a uniform fluid, a molecular version of Eq. 1.6, where D now represents the self-diffusion coefficient, and a taken to be an effective hydrodynamic radius, has been found experimentally to be valid over a wide range of temperatures for many liquids[6–13]. Thus, for a given liquid, we can define a quantity, $D\eta/T$, whose constancy, or lack thereof, over a range of thermodynamic conditions, serves as a measure of the validity of the Stokes-Einstein equation at the molecular level. One then says that the Stokes-Einstein equation is valid when

$$\frac{D\eta}{T} = \text{constant}, \tag{1.7}$$

and any deviations away from Eq. 1.7 would indicate a Stokes-Einstein violation.

Computational studies offer us a particularly useful method to study Stokes-Einstein behavior. In a molecular dynamics simulation, with the ability to track the trajectory of each individual molecule throughout the duration of simulation, the self-diffusion coefficient, D, can be easily calculated by the Einstein diffusion equation,

$$D = \frac{1}{6} \lim_{t\to\infty} \frac{\mathrm{d}}{\mathrm{d}t} \left\langle \Delta r(t)^2 \right\rangle, \tag{1.8}$$

where $\left\langle \Delta r(t)^2 \right\rangle$ is the mean squared displacement of the molecules after an interval of time t. The viscosity, η, can also be computed in a straightforward manner by using a Green-Kubo time-correlation relation[14]:

$$\eta = \frac{V}{k_B T} \int_0^\infty \mathrm{d}t \left\langle P_{xy}(0) P_{xy}(t) \right\rangle, \tag{1.9}$$

where P_{xy} is an off-diagonal element of the stress tensor and V is the volume of the system.

Unfortunately, calculating the viscosity by using Eq. 1.9 can be a computationally intensive process[15]. For a given system, as the temperature is lowered, the time needed for the stress correlation product $\langle P_{xy}(0) P_{xy}(t) \rangle$ to decay to zero can increase by many orders of magnitude. Thus,

when compared to the simulation time needed for calculating structural properties or diffusion, a much longer simulation is needed to obtain viscosity.

For efficiency, it has become increasingly common in computational studies to reinterpret the physical meaning of the Stokes-Einstein relation simply as the product of a diffusion coefficient and a relaxation time, which is commonly obtained from the self-intermediate scattering function. This assumes that relaxation time can be related to the viscosity by a simple proportionality. However, the functional form of this proportionality varies across different studies; the two most often used are $\tau \propto \eta$[16–18] and $\tau \propto \eta/T$[19–23]. Furthermore, when we examine the derivations for these proportionalities, it becomes clear that they refer to two *different* relaxation times: one is a *structural* relaxation time, while the other is a *stress* relaxation time.

The validity of using a relaxation time to study Stokes-Einstein behavior has not been throughly addressed. Additionally, it is commonly assumed in the simulation literature that the structural and stress relaxation times are interchangeable; the validity of this assumption has also not been systematically tested. Chapter 3 provides a systematic study of the distinctions between the true Stokes-Einstein equation, where viscosity is used, and the "proxy" Stokes-Einstein equations, where a relaxation time is used instead, and also investigates the validity of the assumption of interchangeability between structural and stress relaxation times. The model systems used in Chapter 3 are the family of atomic systems, developed and first analyzed in Chapter 2, and a molecular system composed of Lewis and Wahnström *ortho*-terphenyl molecules[24–26]. This greatly simplified model of *ortho*-terphenyl is essentially a rigid triangle: each of the three phenyl rings is represented by a Lennard-Jones site, and the three sites are constrained by rigid bonds. In Chapter 4, we also apply a similar analysis of the Stokes-Einstein variants to a system composed of SPC/E water molecules[27].

1.3 Anomalies of Water

Although water is the most common liquid found on Earth, it is also one of the most unique, and exhibits a number of anomalous properties. These include, at atmospheric pressure, a density maximum at 277 K, an isobaric heat capacity minimum at 308 K, and an isothermal compressibility minimum at 319 K[28]. These anomalous properties may have been essential to the development and sustainment of life on Earth, as a density maximum just above the freezing temperature results in a stable environment for life forms at the bottom of lakes and oceans.

Water also exhibits a number of kinetic anomalies that have been observed experimentally. One of these, which will be studied in depth computationally in Chapter 4, is that the viscosity of water,

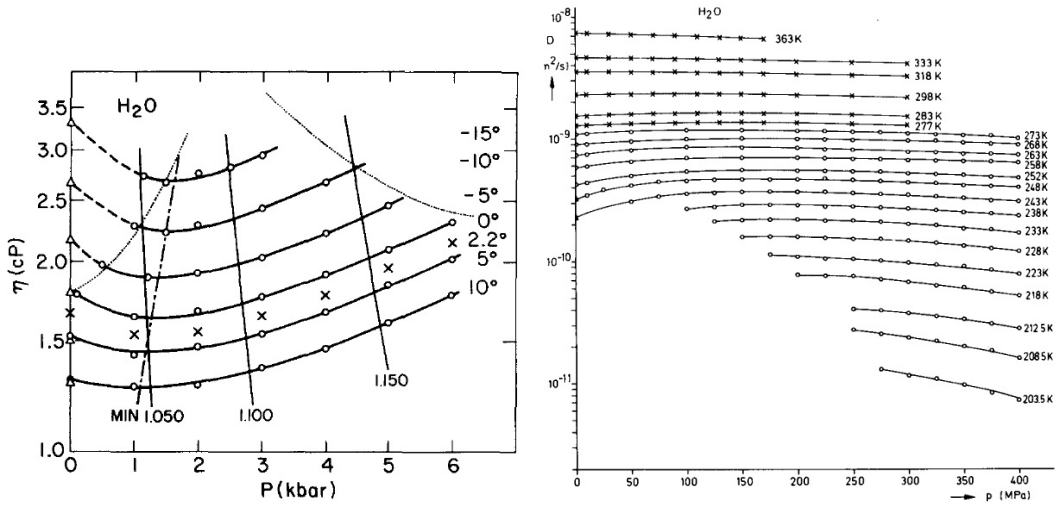

(a) (b)

Figure 1.2: Experimental data showing anomalous kinetic properties of water, where at low enough temperatures, viscosity decreases (a) and diffusion increases (b) upon compression. (a) is reproduced from ref. 29, and (b) from ref. 30. The unit of measurement of the y-axis in panel (b) is m^2/s.

at sufficiently cold temperatures, decreases upon compression (Figure 1.2a)[29]. Meanwhile, the self-diffusivity of water increases upon compression at low enough temperatures (Figure 1.2b)[30]. For both viscosity and diffusivity, the anomalous increase in mobility upon compression is explained by the distortion of the hydrogen bond network[28].

One of the most influential computational studies of the anomalies of water was presented in 2001 by Errington and Debenedetti[31]. That study, which used the SPC/E model of water[27], mapped on a (ρ, T) diagram the regions of structural, kinetic (diffusivity), and thermodynamic anomalous behavior. Structural anomalies, where order decreases upon compression, is observed over the broadest ranges of temperature and densities. The region of diffusivity anomalies, where the diffusion coefficient increases upon compression, is completely contained within the region of structural anomalies. Thermodynamic anomalies, where density decreases upon cooling, occur entirely within the region of diffusivity anomalies. These regions constitute a cascade based on increasing structural order (Figure 1.3a).

Furthermore, within the structurally anomalous region, the orientational and translational order are strongly coupled (Figure 1.3b). Orientational order is defined here as the orientational correlation of a water molecule with its nearest neighbors, while translational order refers to the center-of-mass positional correlation between water molecules. These results further show that the anomalies of water arise from its unique hydrogen bond structure.

While there have been a number of computational studies on water viscosity, to date, the ma-

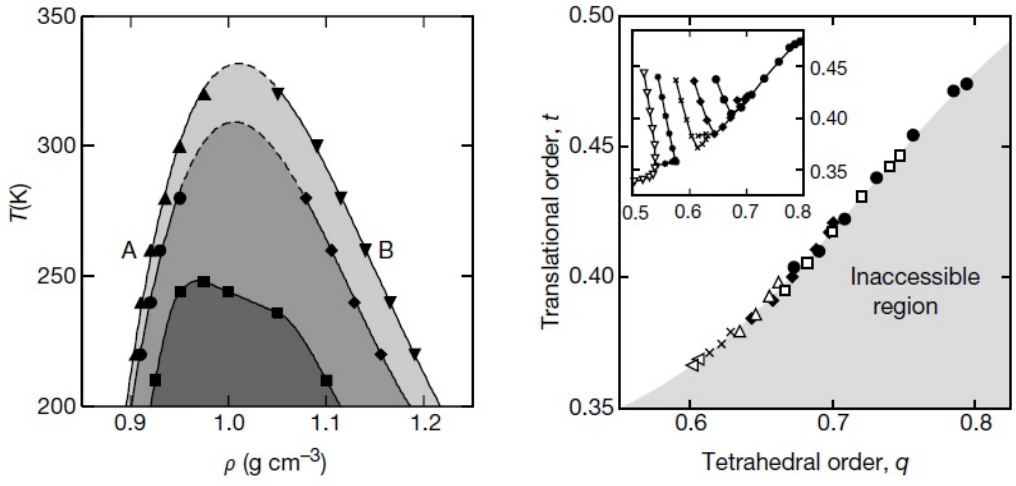

(a) (b)

Figure 1.3: Two main results of the computational study by Errington and Debenedetti on the anomalies of water. (a) The region of anomalies constitutes a cascade; the region of thermodynamic anomalies (squares) is contained within the region of kinetic anomalies (circles and diamonds), which is then contained inside the region of structural anomalies (upward and downward triangles). (b) Within the structurally anomalous region, the orientational and translational order are strongly coupled. The inset shows five isotherms in order-parameter space that span the density range 0.85 to 1.3 g/cm^3 (0.8 to 1.3 g/cm^3 at 400 K), while the data points in the main panel correspond to the subset of thermodynamic states inside the structurally anomalous region. All state points with the structurally anomalous region map onto a single curve. Both figures reproduced from ref. 31.

jority of these only use a limited set of state points. These studies focus on comparisons, between different water models[32–38] or computational methods[39, 40], investigate the effect of different concentration levels of a solute in aqueous solution[41], or study the effects of confinement[42]. In Chapter 4, we instead provide a detailed investigation of the viscosity behavior of SPC/E water across a wide range of temperatures and densities. We then map the region of viscosity anomalous behavior, using a similar approach as the one used in the study by Errington and Debenedetti[31].

The SPC/E (extended simple point charge) model is a rigid 3-site water model. This model has an O-H bond length of 1 Å, and an H-O-H bond angle of 109.47°. The oxygen atom is assigned a point charge of $q_O = -0.8476e$, where is e is the magnitude of the electron charge, and the hydrogen atoms are assigned charges of $q_H = -q_O/2$. Different water molecules also interact via Lennard-Jones sites situated on the oxygen atoms, parameterized by $\sigma = 3.166$ Å and $\epsilon = 0.650$ kJ/mol.

For this model, we provide a comprehensive analysis of viscosity over a wide range of thermodynamic conditions. In agreement with experiment, we observe anomalous behavior at low enough temperatures, where viscosity *decreases* upon compression. This results in another related anomaly: if the viscosity data values along each isochore are fitted to the Vogel-Fulcher-Tammann (VFT)

equation, the asymptotic VTF T_0 values can *decrease* upon compression over a density range. When mapped onto a (ρ, T) plane, the region of the viscosity anomaly is comparable to that of diffusivity.

A comprehensive viscosity data set also allows us to study the Stokes-Einstein behavior of SPC/E water. We observe here another anomaly, where the onset of the low temperature Stoke-Einstein violation can *decrease* upon compression. This also provides us with an additional model system to study the different Stokes-Einstein variants described in Chapter 3. Using the analysis method developed in Chapter 3, we test the validity of using relaxation time to study Stokes-Einstein behavior in SPC/E water, and also continue the discussion of the relationship between the structural and stress relaxation times.

1.4 Films and Interfaces

Ediger and co-workers recently discovered that glass films with exceptional kinetic and thermodynamic stability can be formed by vapor deposition[43–51]. These films are created by using a slow vapor deposition rate onto a substrate. They found that the stability of the resulting glass film is highly dependent on the temperature of the substrate, with an optimal temperature of about $0.85T_g$, where T_g is the glass transition temperature of the substance being deposited. Compared to ordinary glass of the same material formed by quenching, these vapor deposited films have higher density, lower enthalpy, and a higher glass transition temperature (Figure 1.4). These films also exhibit enhanced mobility at the free surface[52, 53] and anisotropic molecular packing[54, 55].

The underlying mechanism causing the enhanced kinetic stability is being actively researched[56–62]. Recently, the de Pablo research group has performed a number of studies that seek to computationally replicate the process of vapor deposition[60–62]. These simulations mimic the experimental process by gradually adding molecules to the free interface of a growing film. While some of these investigations use a simple binary Lennard-Jones mixture[60, 61], a more realistic model, an atomistic molecular model of trehalose, has also been studied[62]. Consistent with experiment, these studies predict the formation of stable glasses having a higher density, a lower enthalpy, and a higher onset temperature when compared to the corresponding ordinary glass formed by quenching.

In our studies of free-standing films in Chapters 5 and 6, we complement these explicit investigations of the Ediger effect by instead focusing on effects inherent to the presence of an interface. These chapters provide two computational studies of free-standing films. The films studied in Chapter 5 are composed of binary Lennard-Jones atoms, while the films of Chapter 6 consist of Lewis and Wahnström *ortho*-terphenyl molecules. We study the structural and configurational preferences of

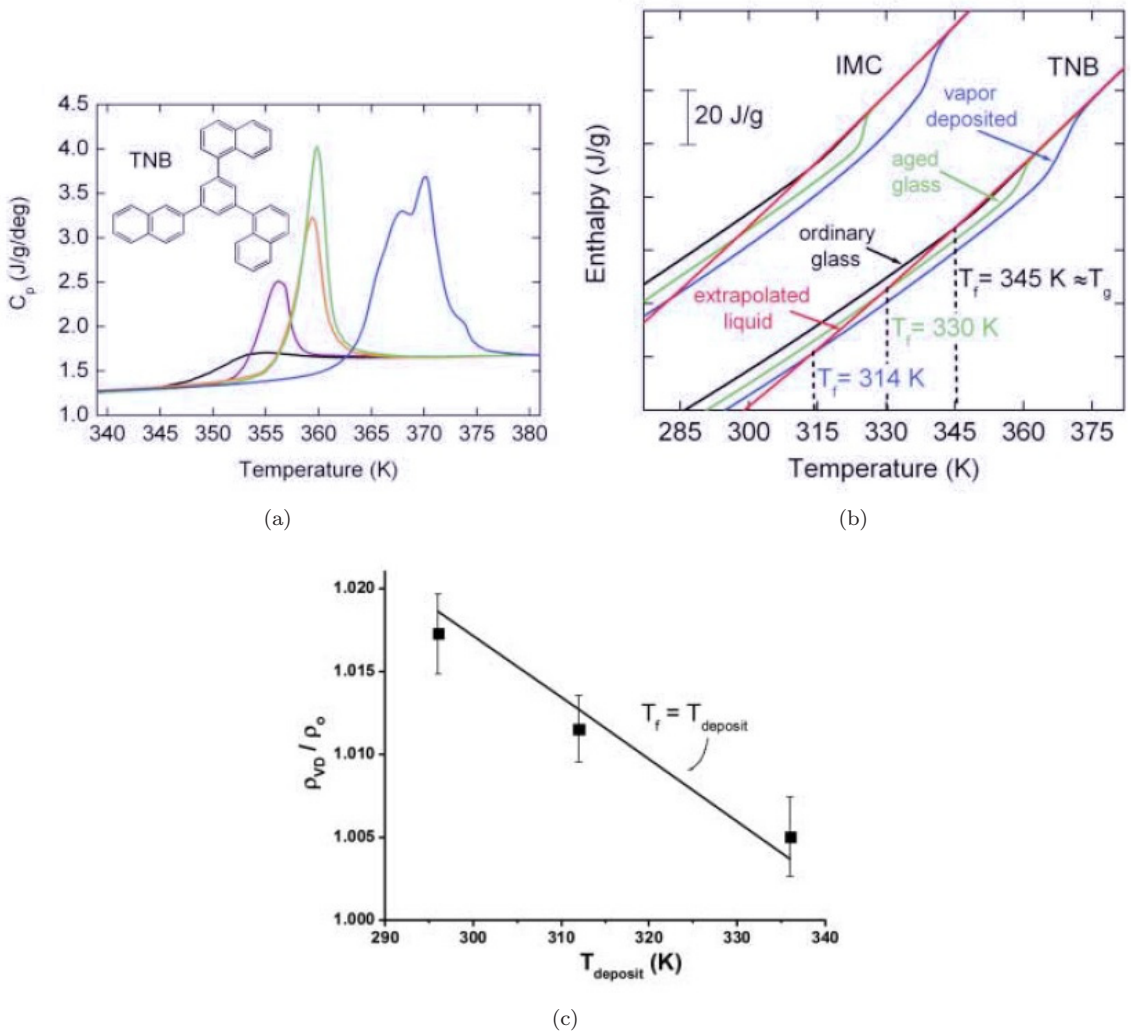

Figure 1.4: Vapor-deposited glasses showing higher glass transition temperature (a), lower enthalpy (b), and enhanced density (c). All three figures report data obtained from vapor deposition of the glass former 1,3-bis-(1-naphthyl)-5-(2-naphthyl)benzene (TNB). Panel (b) additionally shows the enthalpy comparison for indomethacin (IMC). All figures reprinted from ref. 43.

atoms and molecules as a function of film depth, while also comparing the diffusivity at the surface against in the interior.

For these free standing films, the film's interior density and interface width depend solely on temperature, and not the initialization method or the total number of atoms or molecules. For films composed of a binary Lennard-Jones mixture, species segregation occurs at equilibrium, with the smaller minority component preferentially excluded from the surface. For films composed of Lewis and Wahnström *ortho*-terphenyl molecules, we find that the surface biases the orientation of the molecules, and the resulting configurational ordering extends well below the interface to a distance roughly equal to 1.5 times the thickness of the interfacial region. In all cases, diffusivity at the

surface is greatly enhanced relative to the interior. Additionally, we perform an energy landscape analysis of these thin films, and find that molecules at the surface are able to sample the underlying energy landscape more effectively than those in the interior.

1.5 Publications of Research Results

The following chapters of this dissertation are based in full or in part on the following publications:

- Z. Shi, P. G. Debenedetti and F. H. Stillinger, "Properties of Model Atomic Free-Standing Thin Films". J. Chem. Phys. **134**, 114524 (2011).
- Z. Shi, P. G. Debenedetti, F. H. Stillinger and P. Ginart, "Structure, Dynamics, and Thermodynamics of a Family of Potentials with Tunable Softness". J. Chem. Phys. **135**, 084513 (2011).
- Z. Shi, P. G. Debenedetti and F. H. Stillinger, "Relaxation Processes in Liquids: Variations on a Theme by Stokes and Einstein". J. Chem. Phys. **138**, 12A526 (2013).
- Z. Shi, P. G. Debenedetti and F. H. Stillinger, "Interface Induced Processes: A Study of Free Standing Films Composed of Rigid Molecules". *In Preparation* (2014).
- Z. Shi, V. Hwang and P. G. Debenedetti, "Anomalies of Water: Viscosity and Stokes-Einstein Violation". *In Preparation* (2014).

The study presented in Chapter 4,"Anomalies of Water: Viscosity and Stokes-Einstein Violation", is the result of a collaboration between Pablo Debenedetti (PGD), Victoria Hwang (VH), and myself (ZS). The results of this study were also presented in VH's Princeton University Senior Thesis, "Viscosity Anomalies and Violations of the Stokes-Einstein Equation in Molecular Simulations of Water" (2013). For this study, PGD is the principal investigator and corresponding author of the resulting journal article. ZS developed all codes and scripts used to perform the molecular dynamics simulations and subsequent post-processing trajectory analysis. The execution of these codes and scripts were performed by both ZS and VH. Most procedures associated with creating graphs, including plotting of the data points, curve fitting, analytical analysis of the fitted curves, and error bar analysis, were performed by VH, under the guidance of both PGD and ZS.

Bibliography

[1] G. E. Moore, Electronics **38**, 114117 (1965).

[2] J. P. Hansen and I. R. McDonald, *Theory of Simple Liquids*, 2nd ed. ed. (Academic Press, 1986), chap. 1.

[3] G. G. Stokes, Trans. Cambridge Philos. Soc. **9**, 8 (1851).

[4] L. M. Milne-Thomson, *Theoretical Hydrodynamics*, 4th ed. ed. (Macmillan Co., 1960), p. 584.

[5] A. Einstein, Ann. Phys. **17**, 549 (1905).

[6] A. Noda, K. Hayamizu, and M. Watanabe, J. Phys. Chem. B **105**, 4603 (2001).

[7] J. Read *et al.*, J. Electrochem. Soc. **150**, A1351 (2003).

[8] C. Comminges, R. Barhdadi, M. Laurent, and M. Troupel, J. Chem. Eng. Data **51**, 680 (2006).

[9] D. P. Dobson, J. P. Brodholt, L. Vočadlo, and W. A. Crichton, Mol. Phys. **99**, 773 (2001).

[10] E. D. Snijder, M. J. M. te Riele, G. F. Versteeg, and W. P. M. van Swaaij, J. Chem. Eng. Data **38**, 475 (1993).

[11] S. F. Swallen, P. A. Bonvallet, R. J. McMahon, and M. D. Ediger, Phys. Rev. Lett. **90**, 015901 (2003).

[12] M. K. Mapes, S. F. Swallen, and M. D. Ediger, J. Phys. Chem. B **110**, 507 (2006).

[13] F. Mallamace *et al.*, J. Chem. Phys. **124**, 161102 (2006).

[14] J. P. Hansen and I. R. McDonald, *Theory of Simple Liquids*, 2nd ed. ed. (Academic Press, 1986), chap. 8.

[15] J.-L. Barrat, J.-N. Roux, and J.-P. Hansen, Chem. Phys. **149**, 197 (1990).

[16] S.-H. Chen *et al.*, Proc. Natl. Acad. Sci. U.S.A **103**, 12974 (2006).

[17] P. Kumar *et al.*, Proc. Natl. Acad. Sci. U.S.A **104**, 9575 (2007).

[18] L. Xu *et al.*, Nat. Phys. **5**, 565 (2009).

[19] D. Jeong, M. Y. Choi, H. J. Kim, and Y. Jung, Phys. Chem. Chem. Phys. **12**, 2001 (2010).

[20] S. H. Lee and T. Chang, Bull. Korean Chem. Soc. **24**, 1590 (2003).

[21] G. Tarjus and D. Kivelson, J. Chem. Phys. **103**, 3071 (1995).

[22] Y. Jung, J. P. Garrahan, and D. Chandler, Phys. Rev. E **69**, 061205 (2004).

[23] R. Yamamoto and A. Onuki, Phys. Rev. Lett. **81**, 4915 (1998).

[24] L. J. Lewis and G. Wahnström, Solid State Commun. **86**, 295 (1993).

[25] L. J. Lewis and G. Wahnström, J. Non-Cryst. Solids **172-174**, 69 (1994).

[26] L. J. Lewis and G. Wahnström, Phys. Rev. E **50**, 3865 (1994).

[27] H. J. C. Berendsen, J. R. Grigera, and T. P. Straatsma, J. Phys. Chem. **91**, 6269 (1987).

[28] P. G. Debenedetti, J. Phys.: Condens. Matter **15**, R1669 (2003).

[29] T. DeFries and J. Jonas, J. Chem. Phys. **66**, 896 (1977).

[30] F. X. Prielmeier, E. W. Lang, R. J. Speedy, and H.-D. Ldemann, Ber. Bunsenges. Phys. Chem. **92**, 1111 (1988).

[31] J. R. Errington and P. G. Debenedetti, Nature **409**, 318 (2001).

[32] G. Delgado-Barrio *et al.*, Viscosity of liquid water via equilibrium molecular dynamics simulations, in *Frontiers in Quantum Systems in Chemistry and Physics*, edited by S. Wilson, P. Grout, J. Maruani, G. Delgado-Barrio, and P. Piecuch, , Progress in Theoretical Chemistry and Physics Vol. 18, pp. 351–361, Springer Netherlands, 2008.

[33] P. E. Smith and W. F. van Gunsteren, Chem. Phys. Lett. **215**, 315 (1993).

[34] Y. Mao and Y. Zhang, Chem. Phys. Lett. **542**, 37 (2012).

[35] M. A. González and J. L. F. Abascal, J. Chem. Phys. **132**, 096101 (2010).

[36] J. S. Medina *et al.*, Chem. Phys. **388**, 9 (2011).

[37] Y. Wu, H. L. Tepper, and G. A. Voth, J. Chem. Phys. **124**, 024503 (2006).

[38] U. Balucani, J. P. Brodholt, P. Jedlovszky, and R. Vallauri, Phys. Rev. E **62**, 2971 (2000).

[39] B. Hess, J. Chem. Phys. **116**, 209 (2002).

[40] T. Chen, B. Smit, and A. T. Bell, J. Chem. Phys. **131**, 246101 (2009).

[41] E. J. W. Wensink, A. C. Hoffmann, P. J. van Maaren, and D. van der Spoel, J. Chem. Phys. **119**, 7308 (2003).

[42] N. R. Haria, G. S. Grest, and C. D. Lorenz, J Phys. Chem. C **117**, 6096 (2013).

[43] S. F. Swallen *et al.*, Science **315**, 353 (2007).

[44] K. L. Kearns, S. F. Swallen, M. D. Ediger, T. Wu, and L. Yu, J. Chem. Phys. **127**, 154702 (2007).

[45] K. L. Kearns *et al.*, J. Phys. Chem. B **112**, 4934 (2008).

[46] K. J. Dawson, K. L. Kearns, M. D. Ediger, M. J. Sacchetti, and G. D. Zografi, J. Phys. Chem. B **113**, 2422 (2009).

[47] K. J. Dawson, K. L. Kearns, L. Yu, W. Steffen, and M. D. Ediger, Proc. Natl. Acad. Sci. U.S.A. **106**, 15164 (2009).

[48] K. L. Kearns, M. D. Ediger, H. Huth, and C. Schick, J. Phys. Chem. Lett. **1**, 388 (2010).

[49] K. L. Kearns, T. Still, G. Fytas, and M. D. Ediger, Adv. Materials **22**, 39 (2010).

[50] M. Ahrenberg *et al.*, J. Chem. Phys. **138**, 024501 (2013).

[51] K. R. Whitaker, M. Ahrenberg, C. Schick, and M. D. Ediger, J. Chem. Phys. **137**, 154502 (2012).

[52] A. Sepúlveda, S. F. Swallen, and M. D. Ediger, J. Chem. Phys. **138**, 12A517 (2013).

[53] A. Sepúlveda, S. F. Swallen, L. A. Kopff, R. J. McMahon, and M. D. Ediger, J. Chem. Phys. **137**, 204508 (2012).

[54] S. S. Dalal and M. D. Ediger, J. Phys. Chem. Lett. **3**, 1229 (2012).

[55] K. Dawson *et al.*, J. Chem. Phys. **136**, 094505 (2012).

[56] Z. Chen and R. Richert, J. Chem. Phys. **135**, 124515 (2011).

[57] Z. Chen, A. Sepúlveda, M. D. Ediger, and R. Richert, J. Chem. Phys. **138**, 12A519 (2013).

[58] R. L. Jack, L. O. Hedges, J. P. Garrahan, and D. Chandler, Phys. Rev. Lett. **107**, 275702 (2011).

[59] T. Speck, A. Malins, and C. P. Royall, Phys. Rev. Lett. **109**, 195703 (2012).

[60] S. Singh, M. D. Ediger, and J. J. de Pablo, Nature Mater. **12**, 139 (2013).

[61] I. Lyubimov, M. D. Ediger, and J. J. de Pablo, J. Chem. Phys. **139**, 144505 (2013).

[62] S. Singh and J. J. de Pablo, J. Chem. Phys. **134**, 194903 (2011).

Chapter 2

Structure, Dynamics, and Thermodynamics of a Family of Potentials with Tunable Softness

2.1 Introduction

Understanding the microscopic origin of the pronounced temperature dependence of structural relaxation in supercooled liquids, and the laboratory glass transition to which this behavior gives rise, is a major open question in condensed matter physics (see, e.g., refs. 1–16). An important aspect of this question is elucidating how specific features of molecular interactions, such as attractive and repulsive forces, influence the rich variety of phenomena associated with the glass transition[17]. Computer simulations are ideally suited to the pursuit of this question because they allow interactions between particles to be varied in a systematic manner, thereby enabling the investigation of the effects of changes in individual variables to be conducted with a level of specificity not generally possible in experiments.

To date, relatively few investigations have explored systematically the effects of changes in the interaction potential upon viscous liquid behavior. Bordat *et al.*[18, 19] investigated the dynamics of three different binary mixtures: the Kob-Andersen Lennard-Jones mixture[20] (80%A, 20%B, $\epsilon_{AA} = 1.0$, $\epsilon_{BB} = 0.5$, $\epsilon_{AB} = 1.5$, $\sigma_{AA} = 1.0$, $\sigma_{BB} = 0.88$, and $\sigma_{AB} = 0.8$), and two variants thereof in which the AA interaction potential had repulsive and attractive exponents of $(8, 5)$ and

(12, 11), respectively, while the well depth and its location remained fixed. The anharmonicity of the pairwise interaction energy is largest for the (8, 5) case and smallest for the (12, 11) model, with the Kob-Andersen mixture falling in between. These authors found a positive correlation between fragility[21], a measure of the sensitivity of the structural relaxation time to changes in temperature, and the anharmonicity of the interaction potential. Berthier and Tarjus[17, 22] investigated the effect of attractive forces in viscous liquids by comparing the structure and dynamics of the Kob-Andersen binary Lennard-Jones mixture to those of the corresponding Weeks-Chandler-Andersen[23] (WCA) purely repulsive mixture, which lacks the attractive tail. These authors found that at liquid-like densities and at temperatures characteristic of viscous liquid behavior, the dynamics is strongly influenced by attractive forces. De Michele *et al.* investigated the scaling of the dynamics of soft spheres upon varying the repulsive exponent, and found that the temperature dependence of the diffusivity collapses onto a universal curve upon rescaling the temperature[24]. It has recently been shown experimentally that colloidal particles exhibit decreasing fragility with increasing softness[25], in apparent contradiction with the computational studies of Bordat *et al.* Krekelberg *et al.*[26] investigated the effects of short-range attractions on fluid structure and dynamics by comparing the properties of the hard-sphere and square-well systems. Pond *et al.*[27] compared the applicability of the generalized entropy-scaling approach[28, 29] for estimating transport properties in several repulsive models (soft-sphere, Gaussian[30], Hertzian[31]). In addition to the above-mentioned studies, in which explicit perturbations of interparticle interactions were investigated, it should also be mentioned that the accepted liquid-state picture whereby repulsive forces play a dominant role in determining structure, with attractive forces providing a uniform cohesive background[23] underlies important recent work on viscous liquids. This includes the successful temperature and density scaling of supercooled liquid dynamics (e.g., refs. 32–36), and a promising picture of liquid-state regularities based on the notion of strong pressure-energy correlations (e.g., refs. 37–41).

It appears useful, in light of the above-cited work, to formulate models in which specific aspects of interparticle interactions can be perturbed systematically, and to investigate the consequences of such perturbations on structure, dynamics, and thermodynamics, with emphasis on supercooled states. This is the task that we undertake in this chapter. Specifically, we construct a family of generalized Lennard-Jones binary mixtures with tunable softness, fixed well depth, and fixed well location. We investigate computationally a broad spectrum of thermodynamic and dynamic properties as a function of softness. In Section 2.2 we define the model and provide details of the computational methods utilized in our investigation. The thermodynamic properties of the family of mixtures are presented and discussed in Section 2.3, and the corresponding analysis for dynamic

properties is the subject of Section 2.4. The principal conclusions and suggestions for further inquiry are presented in Section 2.5.

2.2 Methods

2.2.1 Definition of Potentials

Starting from the well-known $(12, 6)$ Lennard-Jones (LJ) potential,

$$\phi^{LJ}(r) = 4\epsilon \left[\left(\frac{\sigma}{r}\right)^{12} - \left(\frac{\sigma}{r}\right)^{6} \right], \tag{2.1}$$

we define, for a given repulsive exponent n, a generalized $(n, 6)$ potential with the following functional form:

$$\phi = 4\epsilon \left[\lambda \left(\frac{\sigma}{r}\right)^{n} - \alpha \left(\frac{\sigma}{r}\right)^{6} \right], \tag{2.2}$$

where

$$\lambda = \frac{3}{2}\left(\frac{2^{\frac{n}{6}}}{n-6}\right) \qquad \alpha = \frac{n}{2(n-6)}. \tag{2.3}$$

λ and α are chosen such that the well depth and location of the minimum of the generalized $(n, 6)$ potentials coincide with the minimum of the standard $(12, 6)$ LJ potential (Figure 2.1). The second and third derivatives of ϕ with respect to r, evaluated at $r = 2^{1/6}\sigma$, where $\phi'(r) = 0$, are given by

$$\sigma^2\phi''/\epsilon = 2^{2/3} \cdot 3n, \tag{2.4}$$

$$\sigma^3\phi'''/\epsilon = -2^{1/2} \cdot 3n(n+9). \tag{2.5}$$

Thus, we have a family of potentials of varying softness, with the repulsive exponent n as the tuning parameter, with all members of the family sharing identical characteristic energy and length. It is important to point out that the constraints of invariant energy and length scales (well depth, well depth location) give rise to progressively stronger attractive energies (more negative attractive tails) for $r > 2^{1/6}\sigma$ upon decreasing n (see Figure 2.1). Such constrained softening will be shown to have a pronounced effect, particularly on the energy of the liquid and its inherent structures[42].

In this study, we consider the family of potentials defined by Eq. 2.2, with $n = 7, 8, 9, 10, 11, 12$. Ahmed and Sadus[43] investigated solid-liquid equilibria in a family of potentials closely related to those used in this work. Several authors have investigated vapor-liquid coexistence in $(n, 6)$ or (n, m) potentials[44–47]. The usefulness of such models in coarse-graining applications has also received

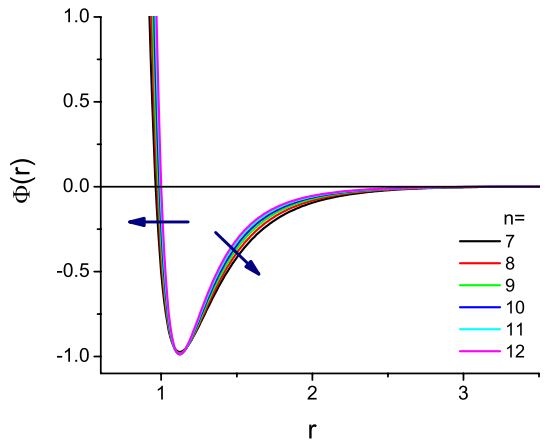

Figure 2.1: The family of potentials used in this chapter. The arrows show the effect of softening.

attention[47, 48].

2.2.2 Simulation Details

For each interaction potential, we study the well-known binary glass-forming mixture as parameterized by Kob and Andersen[20], namely, a mixture of 80%A particles and 20%B particles, with parameters $\epsilon_{AA} = 1.0$, $\epsilon_{BB} = 0.5$, $\epsilon_{AB} = 1.5$, $\sigma_{AA} = 1.0$, $\sigma_{BB} = 0.88$, and $\sigma_{AB} = 0.8$. Both types of particles have the same mass, m. Thoughout this paper, all quantities are expressed in reduced units: length in units of σ_{AA}, temperature in units of ϵ_{AA}/k_B, where k_B is Boltzmann's constant, and time in units of $\sigma_{AA}(m/\epsilon_{AA})^{1/2}$. In order to ensure continuity of the potential and its first derivative at the potential cutoff (continuity needed for energy minimization calculations), we apply a shifted force correction to the potentials:

$$\phi^{sf}(r) = \begin{cases} \phi(r) - \phi(r_c) - (r - r_c)\phi'(r_c) & r \leq r_c \\ 0 & r > r_c \end{cases}, \tag{2.6}$$

where $\phi(r)$ is the pair potential. To minimize the effects of the shift on the shape of the various potentials, we choose a rather large cutoff, $r_c = 3.5$. Our computational cell consists of 500 particles in a box of volume $V = (7.368)^3$, corresponding to a reduced density of $\rho = 1.25$. Periodic boundary conditions are applied in all directions. The velocity Verlet algorithm of numerical integration is used, and the molecular dynamics time step is 0.002. The system is initialized as an fcc lattice, where the identity of a particle is selected at random, while maintaining the overall 4 : 1 ratio of

A to B particles, and is then melted at a high temperature of $T = 5.0$. It is then cooled to the desired temperature, and equilibrated for 2.5×10^5 time steps. A coordinate snapshot is taken every 5000 time steps thereafter. The simulations are run at fixed particle number, total volume, and temperature (N, V, T), with a Nosé-Hoover thermostat[49].

To study the underlying inherent structures[42] embedded in the system's multidimensional energy landscape[1], we perform energy minimization on each coordinate snapshot by applying the Fletcher and Reeves[50] method of conjugate gradients. The particles in the system are moved iteratively along the gradient of the potential energy landscape until $U(\mathbf{r}^N)$, the potential energy as a function of the system's $3N$ translational degrees of freedom, is at a local minimum. The criterion for convergence is satisfied when successive iterations reduce the energy per particle by less than 10^{-7}.

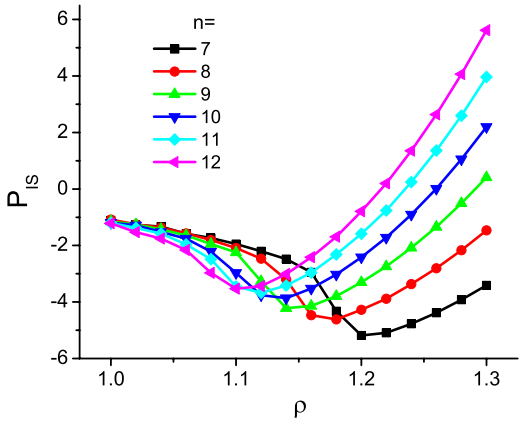

Figure 2.2: Sastry curves showing the dependence of inherent structure pressure upon density. Each point is the average of 100 energy minimizations at constant volume, starting from equilibrated liquid configurations at $T = 1.0$. Note the progressive destabilization of inherent structures upon softening, such that for $n = 7$, inherent structures with $\rho \leq 1.2$ are fractured and spatially inhomogeneous.

The simulation density of 1.25 is slightly higher than used in earlier studies of the same 80-20 Kob and Andersen system interacting via the standard $(12, 6)$ LJ potential[51]. It was found that at a density of 1.2, a system interacting via the $n = 7$ potential cavitates upon isochoric energy minimization, creating fractures in the inherent structure configurations. The reason for this is apparent when we examine the so-called Sastry curves[52] for this family of potentials (i.e., the relationship between inherent structure pressure and density, also called the equation of state of the energy landscape[53])(Figure 2.2). The Sastry density, which corresponds to the minimum pressure along the curve, is the limit of mechanical stability of the inherent structures[54]. Below the Sastry

density, fractures form in the inherent structure because the system cannot simultaneously satisfy mechanical stability and spatial homogeneity. Thus, as the interaction potential is softened, the inherent structures become mechanically unstable at progressively higher densities. We thus choose a density of 1.25 to ensure that the inherent structures are fracture-free for all values of the repulsive exponent used in this work.

2.3 Results and Discussion: Thermodynamic and Structural Properties

2.3.1 Radial Distribution

For each of the six repulsive exponents considered, we calculate the three radial distribution functions, $g_{AA}(r)$, $g_{AB}(r)$, and $g_{BB}(r)$, for both liquid and inherent structure configurations. Representative results for $g_{AA}(r)$, $g_{AB}(r)$, and $g_{BB}(r)$ of the liquid configurations, equilibrated at $T = 1.2$, are shown in the top row of Figure 2.3, for exponents $n = 7, 9, 12$, and the corresponding inherent structure radial distribution functions are shown in the bottom row of Figure 2.3. It can be seen that radial distribution functions are very similar for the three exponents; the inherent structure curves are nearly identical, while the corresponding liquid configuration curves obtained before minimization exhibit only a modest dependence on n. Qualitatively similar results are obtained across the range of temperatures explored in this work ($0.3 \leq T \leq 2.0$). Thus, across the range of conditions investigated in this work, the softening of the interaction potential and the resulting increase in attractive energies beyond the potential minimum have only a modest effect on liquid structure, and a negligible effect on the corresponding inherent structures. This is in contrast with several transport and thermodynamic properties reported in the following sections.

2.3.2 Energy

Figure 2.4 shows the equilibrium potential energy as a function of temperature for $n = 7, \ldots, 12$. The marked decrease in energy upon softening is in sharp contrast with the corresponding insensitivity of structure (compare Figures 2.3 and 2.4). Although surprising at first given that the family of potentials has fixed well depth by construction, the behavior shown in Figure 2.4 is a direct consequence of the progressively stronger attractions upon decreasing n (see Figure 2.1).

The same pronounced energetic stabilization upon softening of the potential (and the consequent increase in attractive energies beyond the potential energy minimum) can also be seen in the inherent

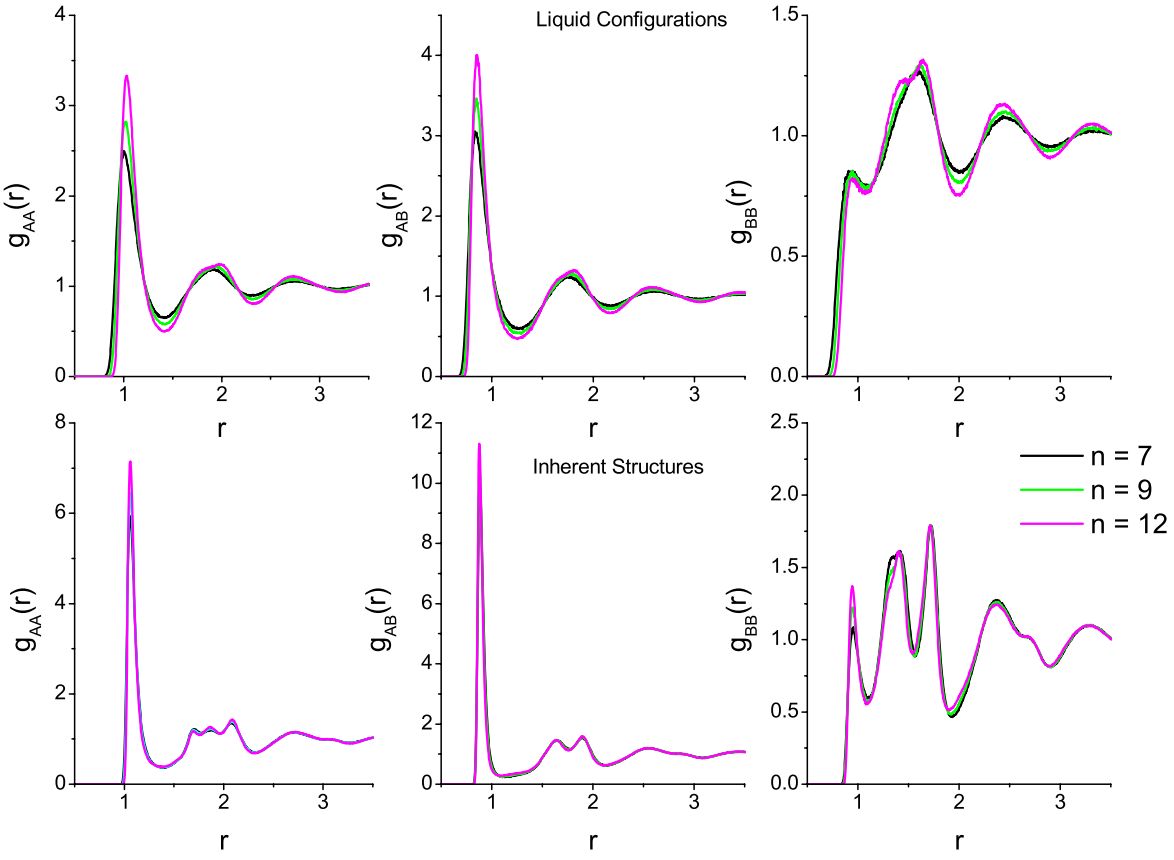

Figure 2.3: The AA, AB, and BB Radial distribution functions for both liquid configurations (top row) and inherent structures (bottom row) at $\rho = 1.25$, for three values of the repulsive exponent. The liquid configurations are equilibrated at $T = 1.2$; the inherent structures are obtained from the corresponding equilibrated liquids at $T = 1.2$.

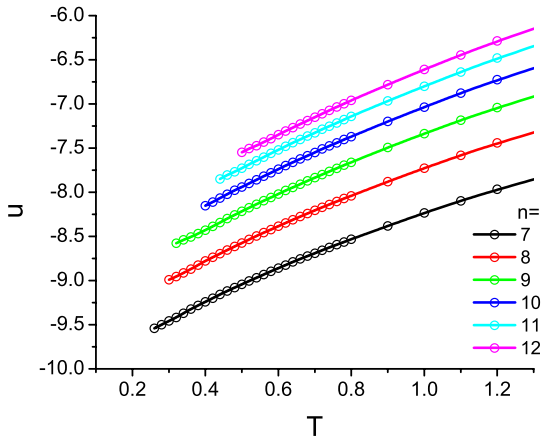

Figure 2.4: Configurational energies per particle, for the equilibrated liquids at $\rho = 1.25$.

structures, as shown in Figure 2.5, where each point is the average of 2000 minimizations. Note that the lowest attainable mean inherent structure energy per particle decreases from -8.28 ($n = 12$) to -9.93 ($n = 7$). It is clear that the increase in attractive energies caused by softening allows the system to sample deeper basins in its energy landscape. In addition, the onset temperature, below which the depth of sampled inherent structures depends sensitively on the temperature at which the liquid is equilibrated prior to minimization, decreases upon softening. Thus, our constrained softening, which preserves the characteristic energy and length scales and thereby gives rise to enhanced attractions at separations exceeding the potential energy minimum, allows the system to more effectively sample its underlying energy landscape at fixed temperature. Equivalently, it enables the extension of liquid-like behavior to progressively lower temperatures. Indeed, a low temperature for $n = 12$ (e.g., $T = 0.55$; see Figure 2.5) still corresponds to a high temperature for $n = 7$.

2.3.3 Entropy

We calculate the entropy associated with sampling different basins in the underlying energy landscape[1], commonly referred to as configurational entropy, S_{conf}, in the literature on supercooled liquids[55, 56]. Following the methodology of Sciortino and co-workers, we approximate this quantity as the difference between the entropy of the equilibrium liquid, S_{liq}, and the harmonic entropy of a disordered solid, S_{sol}. The later is obtained from the eigenfrequency spectrum of inherent structures generated from the equilibrium liquid at the given T and ρ.

The liquid entropy is calculated by thermodynamic integration. We begin with an ideal gas

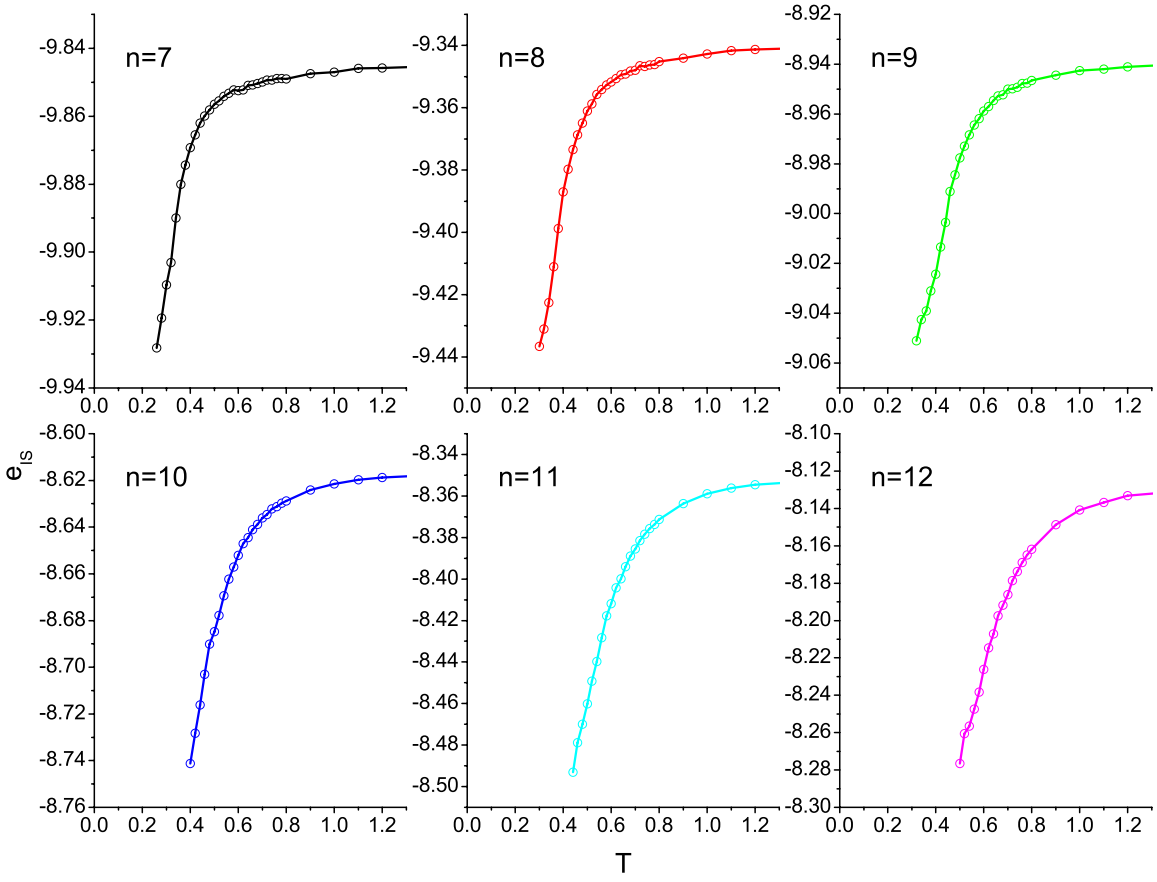

Figure 2.5: Mean inherent structure energies as a function of the temperature prior to energy minimization, at $\rho = 1.25$, for the various potentials investigated in this work.

reference point ($T = 5.0, \rho = 0.01$), where the entropy is known, and integrate along the $T = 5.0$ isotherm to the density studied, $\rho = 1.25$ using the thermodynamic identity

$$S(T,\rho) = S_{ideal\ gas}(T,\rho) + \frac{U(T,\rho)}{T} + \int_{\infty}^{N/\rho} \frac{P_{ex}\mathrm{d}V'}{T}, \tag{2.7}$$

where U is the potential energy and P_{ex} is the excess pressure over the ideal-gas value at the same temperature and density. For a binary ideal gas mixture,

$$\frac{S_{ideal\ gas}(T,\rho)}{Nk_B} = -\frac{N_A}{N}\ln\left(\frac{N_A}{N}\right) - \frac{N_B}{N}\ln\left(\frac{N_B}{N}\right) + \frac{3}{2}\ln\left(\frac{mV^{2/3}}{\beta\hbar^2 2\pi}\right) - \ln N + \frac{5}{2}, \tag{2.8}$$

where N_A and N_B are the number of A and B particles respectively, $N = N_A + N_B$, V is the volume, and $\beta = 1/k_BT$. The last integral in Eq. 2.7 is evaluated numerically (P_{ex} is calculated at discrete steps of the density ρ from 0.01 to 1.25 in steps of 0.01).

Once we have $S(T = 5.0, \rho = 1.25)$, we can then integrate along the isochoric path $\rho = 1.25$ to any temperature T:

$$S_{liq}(T,\rho = 1.25) = S(T = 5.0, \rho = 1.25) + \int_{T=5.0}^{T} \frac{C_V(T')}{T'}\mathrm{d}T', \tag{2.9}$$

where $C_V(T) = \left(\frac{\partial U(T)}{\partial T}\right)_\rho + \frac{3}{2}Nk_B$. For all the interaction potentials considered, we find that $U(T)$ obeys Rosenfeld-Tarazona scaling[57], $U \sim T^{3/5}$ (Figure 2.6). This allows us to compute the integral in Eq. 2.9 analytically and provides a reliable extrapolation below the temperatures studied.

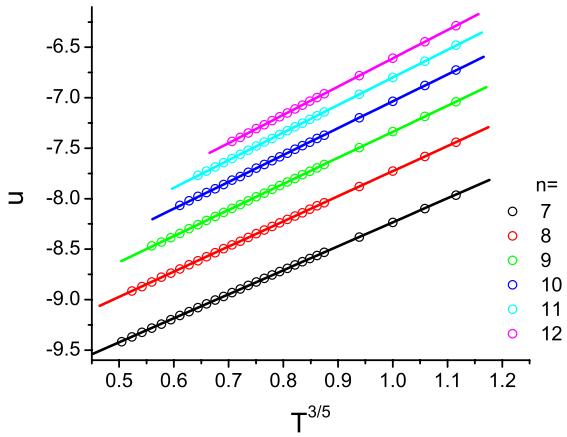

Figure 2.6: Configurational energies of the equilibrated liquids plotted as a function of $T^{3/5}$. Lines are linear fits to the data, showing precise agreement with Rosenfeld-Tarazona scaling, $U \sim T^{3/5}$.

The entropy of the disordered solid, S_{sol} is computed by a normal mode analysis performed on the underlying inherent structures by applying the harmonic approximation:

$$S_{sol}(T,V) = \sum_{j=1}^{3N-3} \left[1 - \ln(\beta\hbar\omega_j)\right], \tag{2.10}$$

where ω_j is the eigenfrequency of the jth normal mode. For each exponent n and temperature T, ω_j was calculated by evaluating the eigenvalues of the Hessian Matrix for 2000 inherent structure configurations. $\sum \ln \omega_j$ was then averaged over all configurations and used in Eq. 2.10 to calculate the solid entropy in the thermodynamic limit. We find that when the explicit T dependence is subtracted from S_{sol}, the resulting difference $S_{sol} - \ln T$ shows a weak T dependence and can be fitted to a simple quadratic function[56]. This fit allows us to also extrapolate S_{sol} to lower temperatures than those studied. To check the validity of the harmonic approximation applied here, we evaluate $u(T) - e_{IS}(T) - \frac{3}{2}k_BT$ for each of our potentials (Figure 2.7). This quantity vanishes for a harmonic system. It can be seen that in the range of temperatures for which entropy calculations were performed (see Figure 2.8), deviations from harmonic behavior are quite minor.

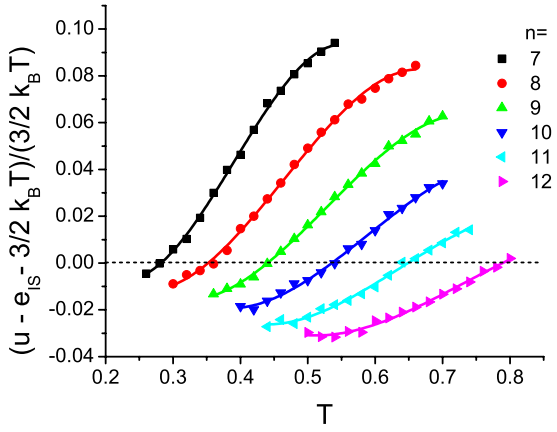

Figure 2.7: Deviation of the difference between the average equilibrium configurational energy $u(T)$ and the average inherent structure energy, $e_{IS}(T)$, from the corresponding quantity for a purely harmonic system, $\frac{3}{2}k_BT$.

Figure 2.8 shows $s_{conf} = s_{liq} - s_{sol}$ as a function of temperature T, where $s = S/N$. We see that softening (lowering n) results in an appreciable increase in configurational entropy for a given temperature. We also see a significant and systematic lowering of the Kauzmann temperature, T_K, defined by the condition[58] $s_{conf}(T_K) = 0$, as the softness of the interaction potential is increased. Furthermore, Figure 2.9 shows that the increase in configurational entropy upon softening is not

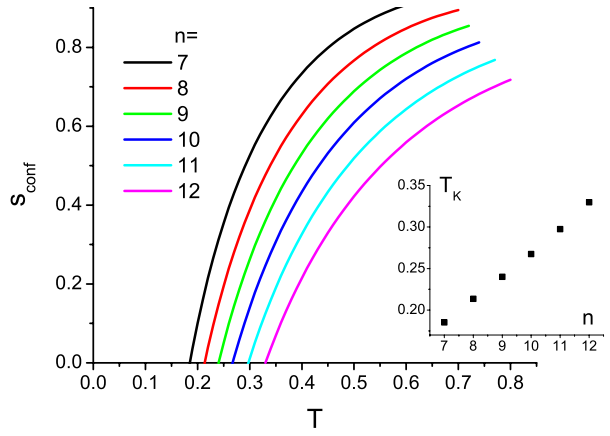

Figure 2.8: Configurational entropies per particle as a function of temperature, at $\rho = 1.25$, for the various potentials investigated in this work. The inset shows the dependence of the temperature where $s_{conf} = 0$, upon the repulsive exponent.

simply a result of a lower Kauzmann temperature; when plotted as a function of T/T_K, s_{conf} increases more rapidly with the scaled temperature as the potential is softened. This shows that softening of the interaction potential results in an increase in the number of basins that the system samples, illustrating the fact that a modest change in the interaction potential has a pronounced effect on the system's low-temperature thermodynamics.

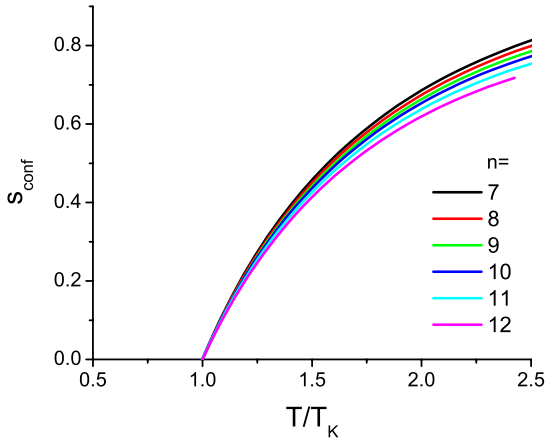

Figure 2.9: Configurational entropies as a function of scaled temperature, at $\rho = 1.25$. The increase in configurational entropy upon softening is evident.

2.4 Results and Discussion: Dynamic Properties

2.4.1 Diffusion

For each repulsive exponent n, we calculate the diffusion coefficient using the standard Einstein equation:

$$D = \frac{1}{6} \lim_{t\to\infty} \frac{\mathrm{d}}{\mathrm{d}t} \left\langle \Delta r(t)^2 \right\rangle, \tag{2.11}$$

where D is the diffusion coefficient, and $\left\langle \Delta r(t)^2 \right\rangle$ is the mean squared displacement of the particles after an interval of time t. Figure 2.10 shows the diffusion coefficient of the A particles for the various potentials, as a function of temperature. While we report here the diffusion results for A particles, we note that the diffusion properties of B particles are qualitatively similar. It can be seen that softening causes a pronounced increase in the diffusion coefficient, resulting in particles interacting via softer potentials to remain diffusive down to appreciably lower temperatures. The inset to Figure 2.10 shows the temperature at which $D = 10^{-4}$, as a function of n (the line though the D vs. T data is a simple logarithmic fit). Note that this characteristic temperature, like T_K (Figure 2.8 inset), decreases by a factor of 2 upon decreasing n from 12 to 7.

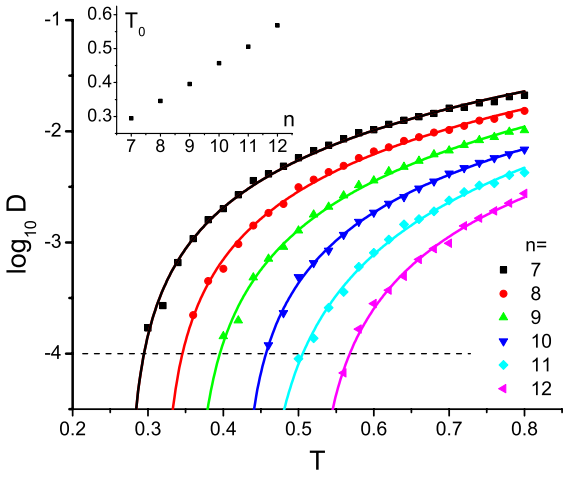

Figure 2.10: Diffusion coefficients of A particles at $\rho = 1.25$, as a function of temperature, for the various potentials studied in this work. Lines are fits of the form $\log D = \log(AT + B)$. The inset shows the dependence of T_0, such that $D(T_0) = 10^{-4}$, upon the repulsive exponent.

2.4.2 Self-Intermediate Scattering Function

To further quantitatively describe the dynamics of the systems under consideration, we compute the self-intermediate scattering function $F_s(k,t) = \langle \exp[i\mathbf{k} \cdot \Delta\mathbf{r}(t)] \rangle$, where $\Delta\mathbf{r}(t)$ is the displacement

experienced by a particle in time t. This quantity, evaluated for A particles, is shown in Figure 2.11. The trajectory of the system was recorded for 1.5×10^7 times steps, with new time origins chosen every 1000 time steps, to provide independent "experiments" over which to average. The wave vector chosen is $k = 7.28\sigma_{AA}^{-1}$, which is close to the first peak of the static structure factor. We shift the time origin to $t_0 = 2.0$ to eliminate the Gaussian time dependence at short t, and normalize $F_s(k,t)$ to the value at t_0. We now define a relaxation time τ such that the shifted and normalized self-intermediate scattering function equals $1/e$.

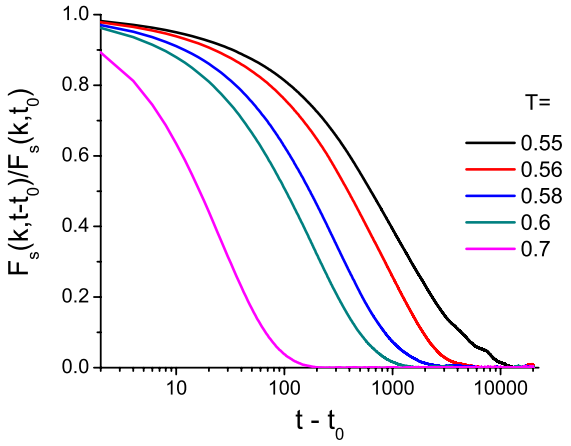

Figure 2.11: Shifted and normalized self-intermediate scattering function for A particles, evaluated at $\rho = 1.25$ and $k = 7.28\sigma_{AA}^{-1}$, with $t_0 = 2.0$. The curves shown correspond to $n = 12$.

Figure 2.12 shows the characteristic relaxation times as a function of temperature for the family of interaction potentials considered in this study. The solid lines are fits to the data using the Vogel-Tammann-Fulcher (VTF) equation,

$$\ln\left(\frac{\tau}{\tau_0}\right) = \frac{B}{T - T_{VTF}}, \tag{2.12}$$

where T_{VTF} is the VTF singular temperature, τ_0 is the high-temperature limit of τ, and $k_B B$ is a characteristic energy (τ_0, T_{VTF}, and B were used as fitting parameters). For each exponent, the τ_0 obtained from fitting is of order 1. The VTF equation is used here simply as a fitting procedure, in order to extract the characteristic temperature where $\tau = 10^4$ (dashed line in figure 2.12). This, as well as T_0 (Figure 2.10) and T_K (Figure 2.8) is used to investigate the dependence of fragility on the repulsive exponent n (see below). In general, for all of the repulsive exponents considered, the fit of the data to the VTF equation is quite good.

Figure 2.13 shows a linear relationship between the logarithm of the characteristic relaxation time,

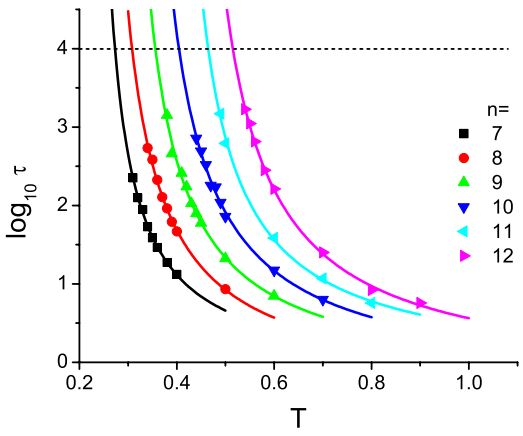

Figure 2.12: Temperature dependence of the structural relaxation times at $\rho = 1.25$, obtained from the self-intermediate scattering function (Figure 2.11), using the condition $F_s(k, t - t_0)/F_s(k, t_0) = e^{-1}$. The lines are VTF fits (see text).

τ, and the inverse of the configurational entropy multiplied by temperature, $1/Ts_{conf}$, calculated in the previous section. Thus, our systems behave in a manner that is consistent with the Adam-Gibbs equation[59]:

$$\tau(T) = A \exp\left(\frac{B}{Ts_{conf}(T)}\right), \tag{2.13}$$

where A and B are constants. This correspondence between dynamics and thermodynamics suggests that relaxation is influenced by the topography of the energy landscape[51].

2.4.3 Fragility

We now examine the effect of softening on the fragility of the family of glass formers. From the previous section, we have two measures of relaxation rates for each repulsive interaction exponent: the inverse of the diffusion coefficient, $1/D$, and the characteristic time τ where $F_s(k, \tau) = 1/e$. These measures can be used to produce the Angell plot[1, 21], in order to compare the fragility of the systems under differing interaction potentials. For inverse diffusion, we choose the characteristic temperature, T_0^D, to be such that $D(T_0^D) = 10^{-4}$ (Figure 2.10). For the characteristic time based on the self-intermediate scattering function (SISF), we investigate two characteristic temperatures: T_0^{SISF}, such that $\tau(T_0^{SISF}) = 10^4$, and T_K.

Figures 2.14–2.16 are the resulting Angell plots. Figure 2.14 shows a clear collapse of all the curves, indicating no effect of softening on fragility when diffusivity is used as a measure of relaxation rate. It remains to be seen whether this trend persists when longer simulations at lower temperatures

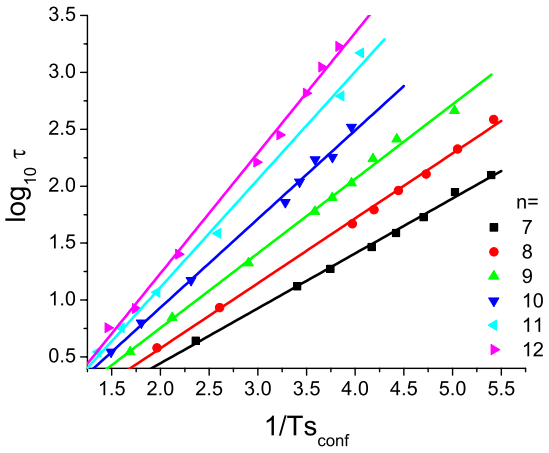

Figure 2.13: Relationship between structural relaxation time obtained from the self-intermediate scattering function, and the configurational entropy. Linear fits to the data show good agreement with the Adam-Gibbs expression, Eq. 2.13.

are used. A modest increase in fragility upon softening can be seen from Figure 2.15 if τ is used as a relaxation measure. Use of T_K as the characteristic temperature accentuates this trend (Figure 2.16), although the effect is not large. It should be noted though, that whereas in Figures 2.14 and 2.15 the attainable range of T_0/T is close to 1, the lowest scaled temperature attained in Figure 2.16 is 0.65.

Figures 2.14–2.16 thus illustrate not only a modest dependence of fragility upon constrained softening, but, more broadly, they point to a challenge inherent in calculating fragility computationally. This arises because, at the temperatures that can be sampled in MD simulations, the system is considerably farther away from structural arrest than in the corresponding experimental determination of fragilities.

2.5 Conclusions

In this chapter we have investigated numerically the structural, thermodynamic and dynamic properties of a family of potentials of variable softness, and fixed well depth and well depth location. In order to explore the low-temperature non-crystalline behavior we considered, for each value of the repulsive exponent, a Kob-Andersen glass-forming binary mixture[20]. Simulations were conducted at a single density, chosen to be high enough to prevent cavitation even for the softer version of the potential investigated here.

Liquid structure, as described by the pair correlation functions, is only moderately sensitive

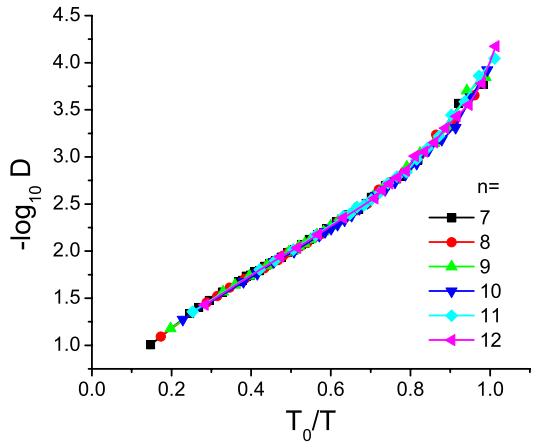

Figure 2.14: Fragility plot using diffusion as a relaxation rate measure, at $\rho = 1.25$. The diffusion coefficients are for A particles (Figure 2.10), and T_0 is chosen such that $D(T_0) = 10^{-4}$.

to constrained variations in softness, and inherent structures are remarkably insensitive to such a perturbation. In sharp contrast, both dynamics and thermodynamics exhibit marked sensitivity to softness. Upon decreasing the repulsive exponent from 12 to 7, the translational diffusion coefficient increases by as much as two orders of magnitude, and liquids interacting via softer potentials remain diffusive down to appreciably lower temperatures. The average configurational energy per particle is larger in magnitude for the softer ($n = 7$) equilibrium liquid mixture than for the Lennard-Jones ($n = 12$) counterpart by more than two full well depths, reflecting the progressively stronger attractions that ensue upon constrained softening, while satisfying the fixed well depth and location constraints (Figure 2.1). Accordingly, the average inherent structure energies are appreciably more negative for the softer mixtures. The lowest-energy mechanically stable packings (inherent structures) that we were able to form, corresponding to the softer extreme considered here ($n = 7$), possess on average an additional cohesive energy of roughly 1.7 well depths per particle relative to their $n = 12$ counterparts (Figure 2.5). This is a consequence of the stronger attractive energies (more negative attractive tails) at separations greater than the well depth that arise as a result of softening.

Progressive softening also results in an increase in entropy, a decrease in the Kauzmann temperature, and a marked extension towards lower temperatures of the conditions at which equilibrium liquid behavior can be observed. Constrained softening, in other words, leads to enhanced entropy and mobility, more stable particle packings, and diffusive behavior at lower temperatures. We find only a modest increase in fragility upon softening, and in order to uncover this trend it is necessary to use both extrapolated relaxation times and extrapolated characteristic temperatures. This points

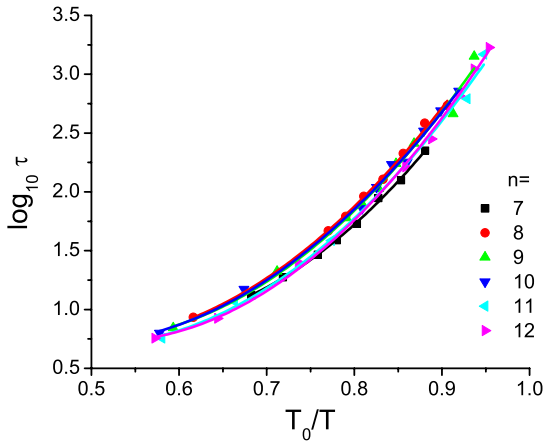

Figure 2.15: Fragility plot using τ as a relaxation rate measure (see Figure 2.11), at $\rho = 1.25$. T_0 is chosen such that $\tau(T_0) = 10^4$ (see Figure 2.12).

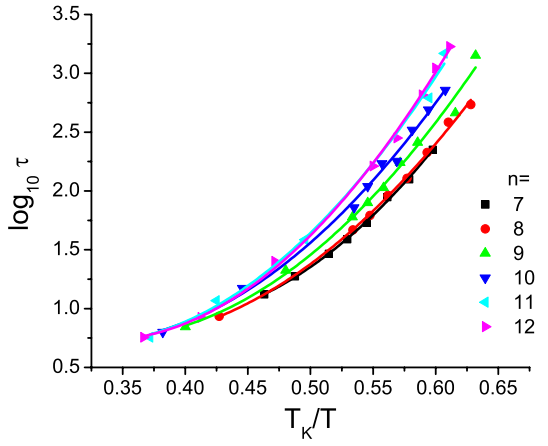

Figure 2.16: Same as Figure 2.15, but using T_K as the characteristic temperature (see Figure 2.8).

to the challenge of calculating fragilities by molecular-based computer simulation, a challenge that originates with the difficulty of sampling low enough temperatures.

The rich behavior identified in the course of this research suggests several directions for future work. In light of the contrast of our results with experimental observations for colloidal particles[25] in which softening leads to a progressive decrease in fragility, it would be interesting to extend the present fragility calculations to other densities. This would allow exploration of regimes in which particles sample different regions of their respective pair potentials. More generally, extending the present structural, dynamic and thermodynamic calculations to a broader range of conditions, including low-density states leading to cavitation in the softer models (Figure 2.2), is important in

order to acquire a fuller picture of this family of potentials. It is also of interest to explore the possibility of scaling behavior, whereby physical properties for the various models may be collapsed into a single curve by appropriate scaling of temperature and/or density. The pronounced sensitivity of inherent structure energy to softness (Figure 2.5) may be of relevance in optimization problems, where strategies involving appropriately-chosen cycles of softness perturbations might be useful for locating deep potential energy minima. Other families of models can be formulated, with an eye to introducing similar systematic perturbations of alternative aspects of the interaction potential, such as attractions. We plan to report our results on several of these topics in future publications.

2.6 Acknowledgments

PGD gratefully acknowledges the support of the Princeton Center for Complex Materials (National Science Foundation Materials Research Science and Engineering Center Grant DMR-0819860) and of the National Science Foundation (Grant CHE-0908265).

Bibliography

[1] P. G. Debenedetti and F. H. Stillinger, Nature **410**, 259 (2001).

[2] V. Lubchenko and P. G. Wolynes, Annu. Rev. Phys. Chem. **58**, 235 (2007).

[3] V. Lubchenko and P. G. Wolynes, J. Chem. Phys. **121**, 2852 (2004).

[4] J. P. Garrahan and D. Chandler, Proc. Nat'l. Acad. Sci. USA **100**, 9710 (2003).

[5] L. O. Hedges, R. L. Jack, J. P. Garrahan, and D. Chandler, **323**, 1309 (2009).

[6] J.-P. Bouchaud and G. Biroli, J. Chem. Phys. **121**, 7347 (2004).

[7] G. Biroli and J.-P. Bouchaud, J. Phys. Condens. Matter **19**, 205101 (2007).

[8] G. Biroli, J. P. Bouchaud, A. Cavagna, T. S. Grigera, and P. Verrocchio, Nat. Phys. **4**, 771 (2008).

[9] R. K. Darst, D. R. Reichman, and G. Biroli, J. Chem. Phys. **132**, 044510 (2010).

[10] G. Tarjus, S. A. Kivelson, Z. Nussinov, and P. Viot, J. Phys. Condens. Matter **17**, R1143 (2005).

[11] A. Heuer, J. Phys. Condens. Matter **20**, 373101 (2008).

[12] A. Widmer-Cooper and P. Harrowell, Phys. Rev. Lett. **96**, 185701 (2006).

[13] A. Widmer-Cooper and P. Harrowell, J. Chem. Phys. **126**, 154503 (2007).

[14] E. J. Saltzman and K. S. Schweizer, J. Chem. Phys. **125**, 044509 (2006).

[15] J. S. Langer, Phys. Rev. Lett. **97**, 115704 (2006).

[16] J. C. Dyre, Rev. Mod. Phys. **78**, 953 (2006).

[17] L. Berthier and G. Tarjus, Phys. Rev. Lett. **103**, 170601 (2009).

[18] P. Bordat, F. Affouard, M. Descamps, and K. L. Ngai, Phys. Rev. Lett. **93**, 105502 (2004).

[19] P. Bordat, F. Affouard, M. Descamps, and K. L. Ngai, J. Non-Cryst. Sol. **352**, 4630 (2006).

[20] W. Kob and H. C. Andersen, Phys. Rev. E **51**, 4626 (1995).

[21] C. A. Angell, K. L. Ngai, G. B. McKenna, P. F. McMillan, and S. W. Martin, J. Appl. Phys. **88**, 3113 (2000).

[22] L. Berthier and G. Tarjus, J. Chem. Phys. **134**, 214503 (2011).

[23] J. D. Weeks, D. Chandler, and H. C. Andersen, J. Chem. Phys. **54**, 5237 (1971).

[24] C. D. Michele, F. Sciortino, and A. Coniglio, J. Phys.: Condens. Matter **16**, L489 (2004).

[25] J. Mattsson *et al.*, Nature **462**, 83 (2009).

[26] W. P. Krekelberg, J. Mittal, V. Ganesan, and T. M. Truskett, J. Chem. Phys. **127**, 044502 (2007).

[27] M. J. Pond, J. R. Errington, and T. M. Truskett, J. Chem. Phys. **134**, 081101 (2011).

[28] Y. Rosenfeld, J. Phys.: Condens. Matter **11**, 5415 (1999).

[29] W. P. Krekelberg *et al.*, Phys. Rev. E **80**, 061205 (2009).

[30] F. H. Stillinger and T. A. Weber, J. Chem. Phys. **68**, 3837 (1978).

[31] L. Berthier, A. J. Moreno, and G. Szamel, Phys. Rev. E **82**, 060501 (2010).

[32] R. Casalini and C. M. Roland, Phys. Rev. E **69**, 062501 (2004).

[33] R. Casalini and C. M. Roland, Phys. Rev. E **72**, 031503 (2005).

[34] C. M. Roland, S. Hensel-Bielowka, M. Paluch, and R. Casalini, Rep. Prog. Phys. **68**, 1405 (2005).

[35] C. M. Roland, S. Bair, and R. Casalini, J. Chem. Phys. **125**, 124508 (2006).

[36] R. Casalini, U. Mohanty, and C. M. Roland, J. Chem. Phys. **125**, 014505 (2006).

[37] U. R. Pedersen, N. P. Bailey, T. B. Schrøder, and J. C. Dyre, Phys. Rev. Lett. **100**, 015701 (2008).

[38] N. P. Bailey, U. R. Pedersen, N. Gnan, T. B. Schrøder, and J. C. Dyre, J. Chem. Phys. **129**, 184507 (2008).

[39] N. P. Bailey, U. R. Pedersen, N. Gnan, T. B. Schrøder, and J. C. Dyre, J. Chem. Phys. **129**, 184508 (2008).

[40] T. B. Schrøder, N. P. Bailey, U. R. Pedersen, N. Gnan, and J. C. Dyre, J. Chem. Phys. **131**, 234503 (2009).

[41] T. B. Schrøder, N. Gnan, U. R. Pedersen, N. P. Bailey, and J. C. Dyre, J. Chem. Phys. **134**, 164505 (2011).

[42] F. H. Stillinger and T. A. Weber, Phys. Rev. A **25**, 978 (1982).

[43] A. Ahmed and R. J. Sadus, J. Chem. Phys. **131**, 174504 (2009), Ahmed and Sadus imposed the constraint of constant well depth but not the constraint of fixed well depth location. It can be shown, however, that the potentials used in this work and in that of Ahmed and Sadus can be mapped onto each other by rescaling σ.

[44] H. Okumura and F. Yonezawa, J. Chem. Phys. **113**, 9162 (2000).

[45] P. Orea, Y. Reyes-Mercado, and Y. Duda, Phys. Lett. A **372**, 7024 (2008).

[46] J. J. Potoff and D. A. Bernard-Brunel, J. Phys. Chem. B **113**, 14725 (2009).

[47] K. A. Maerzke and J. I. Siepmann, J. Phys. Chem. B **115**, 3452 (2009).

[48] X. He, W. Shinoda, R. DeVane, and M. L. Klein, Molec. Phys. **108**, 2007 (2010).

[49] W. G. Hoover, Phys. Rev. A **31**, 1695 (1985).

[50] R. Fletcher and C. M. Reeves, Computer Journal **7**, 149 (1964).

[51] S. Sastry, P. G. Debenedetti, and F. H. Stillinger, Nature **393**, 554 (1998).

[52] S. Sastry, P. G. Debenedetti, and F. H. Stillinger, Phys. Rev. E **56**, 5533 (1997).

[53] P. G. Debenedetti, F. H. Stillinger, T. M. Truskett, and C. J. Roberts, J. Phys. Chem. B **103**, 7390 (1999).

[54] M. Utz, P. G. Debenedetti, and F. H. Stillinger, J. Chem. Phys. **114**, 10049 (2001).

[55] F. Sciortino, W. Kob, and P. Tartaglia, Phys. Rev. Lett. **83**, 3214 (1999).

[56] F. Sciortino, W. Kob, and P. Tartaglia, J. Phys.: Condens. Matter **12**, 6525 (2000).

[57] Y. Rosenfeld and P. Tarazona, Mol. Phys. **95**, 141 (1998).

[58] W. Kauzmann, Chem. Rev. **43**, 219 (1948). The temperature discussed by Kauzmann in his classic article is that at which the entropies of the liquid and crystal phases of a given substance become equal. We use instead the common definition of the Kauzmann temperature in the contemporary literature on the glass transition, namely the temperature at which the entropy

associated with the exploration of distinct configurations appears to vanish. As shown by us [F. H. Stillinger, P. G. Debenedetti, and T. M. Truskett, J. Phys. Chem. B **105**, 11809 (2001)], the former is experimentally attainable and is logically disconnected to the presence of an ideal glass transition.

[59] G. Adam and J. H. Gibbs, J. Chem. Phys. **43**, 139 (1965).

Chapter 3

Relaxation Processes in Liquids: Variations on a Theme by Stokes and Einstein

3.1 Introduction

The well-known Stokes-Einstein equation, which combines Einstein's analysis of the diffusion of small suspended particles[1], and Stokes' formula for the drag on a rigid spherical particle moving through a viscous fluid[2], is given by

$$D = \frac{k_B T}{C \eta a}. \tag{3.1}$$

Here, D is the diffusion coefficient of the macroscopic spheres of radius a, η is the shear viscosity of the surrounding fluid at temperature T, and k_B is Boltzmann's constant. C is a constant that depends on the boundary conditions at the particle-fluid interface, and ranges from 6π for no-slip to 4π for slip boundary conditions[3].

Equation 3.1 has been successfully applied to a wide variety of situations, including enhancement in the thermal conductivity of nano-particle suspensions[4], diffusion of proteins or other macromolecules in solution[5–8], transport in cells[9], and magma flow beneath the Earth's crust[10, 11]. In these cases, a is taken to be an effective hydrodynamic radius[12]. Furthermore, although Eq. 3.1 was derived for a sphere of supermolecular dimensions suspended in a continuum, a molecular-level version of the Stokes-Einstein equation, where D now represents the self-diffusion coefficient of a

uniform fluid, has been found experimentally to be valid over a wide range of temperatures for many liquids[13–20]. Thus, for a given liquid, we can define a quantity, $D\eta/T$, whose constancy, or lack thereof, over a range of thermodynamic conditions, serves as a measure of the validity of the Stokes-Einstein equation at the molecular level. One then says that the Stokes-Einstein equation is valid when

$$\frac{D\eta}{T} = \text{constant}, \tag{3.2}$$

and any deviations away from Eq. 3.2 would indicate a Stokes-Einstein violation.

A well-known condition where Stokes-Einstein violation occurs is when a liquid undergoes deep supercooling[18–23]. As the temperature is decreased into the supercooled regime, the rate at which the viscosity increases can become orders of magnitude larger than that at which the self-diffusion coefficient decreases, and $D\eta/T$ then deviates strongly from Eq. 3.2. Interestingly, the rotational analog of Eq. 3.1 (known as the Stokes-Einstein-Debye equation[24]), $D_r = k_B T/C'\eta a^3$, where D_r is the rotational diffusion coefficient and C' is a numerical constant, can remain valid even when Eq. 3.2 begins to break down[25–27]. This decoupling of translational and rotational diffusion has been explained by invoking dynamic heterogeneity, which refers to the presence of transient spatially separated regions with vastly different relaxation times[24]. The microscopic origin of this supercooled Stokes-Einstein violation, and of the decoupling between translational and rotational motion, is a topic of considerable research interest[28–37].

Molecular dynamics simulation, which has the advantage of being able to track each atom individually, offers a useful and insightful perspective for the microscopic investigation of the mechanisms underlying the Stokes-Einstein violation. Simulations calculating the Stokes-Einstein parameter $D\eta/T$ for soft-sphere systems have shown good qualitative agreement with experiments[38, 39]; Eq. 3.2 is obeyed at moderately high temperatures, but deviations occur as the temperature is progressively decreased. However, because the shear viscosity, η, is a computationally intensive quantity to calculate in simulations[38], it has become increasingly common in computational studies to reinterpret the physical meaning of the Stokes-Einstein relation simply as the product of a diffusion coefficient and a relaxation time. Indeed, many studies of the Stokes-Einstein violation use a structural relaxation time, τ, as a substitute for the viscosity η[25, 40–46]. The functional form of the relation between τ and η varies among different studies; the two most often used are $\tau \propto \eta$[44–46] and $\tau \propto \eta/T$[25, 40–43].

The proportionality between η and τ is based on the expression $\eta = G_\infty \tau$, where G_∞ is the instantaneous shear modulus, and τ is now a *stress* relaxation time. It is commonly assumed in

the simulation literature that the structural and stress relaxation times are interchangeable; the validity of this assumption has not been systematically tested. Although G_∞ does have a slight temperature dependence[47], in the supercooled regime both η and τ can increase by many orders of magnitude as a result of modest decreases in temperature. Thus G_∞ is treated as a constant, leading to the approximate relation $\tau \propto \eta$, which in turn gives $D \propto T/\tau$. The second relation, $\tau \propto \eta/T$ results from the Gaussian solution to the diffusion equation[48], given by $F_s(k,t) = \exp(-k^2 Dt) \equiv \exp(-t/\tau)$, where $F_s(k,t)$ is the self-intermediate scattering function and k is the associated wave vector. It follows then that $D \propto 1/\tau$, which implies $\tau \propto \eta/T$. Yamamoto and Onuki have shown empirical evidence in support of this second relationship[43]. It is important to point out that although the relations $\tau \propto \eta$ and $\tau \propto \eta/T$ differ by a factor of $1/T$, both appear to be reasonable approximations when studying the Stokes-Einstein violation in the deeply supercooled regime, when small temperature changes result in order of magnitude changes in both τ and η.

Although it has become standard in numerical studies to calculate $D\tau/T$ or $D\tau$ as substitutes for $D\eta/T$ when investigating the Stokes-Einstein violation, a systematic study of the various forms of the Stokes-Einstein ratio has not been carried out over broad ranges of thermodynamic conditions. The goal of this chapter is to investigate numerically the temperature and density dependence of the three Stokes-Einstein ratios, $D\eta/T$, $D\tau/T$, and $D\tau$, for selected atomic and molecular model systems. We seek to highlight some non-trivial distinctions between the true Stokes-Einstein equation, where viscosity is used, and the "proxy" Stokes-Einstein equations, where a relaxation time is used instead. We also investigate the validity of the assumption of interchangeability between structural and stress relaxation times. In Section 3.2 we define the models and provide details of the computational methods utilized in our investigation. The qualitative differences that arise between the three variants of the Stokes-Einstein relation are presented and analyzed in Section 3.3. The principal conclusions and suggestions for further study are presented in Section 3.4.

3.2 Methods

3.2.1 Model Atomic System

We seek to investigate the Stokes-Einstein relation in both model atomic and molecular systems. For the model atomic system, we choose a family of systematically softened $(n, 6)$ pair potentials[49]

with the following functional form:

$$\phi(r) = 4\epsilon \left[\lambda \left(\frac{\sigma}{r} \right)^n - \alpha \left(\frac{\sigma}{r} \right)^6 \right], \tag{3.3}$$

where

$$\lambda = \frac{3}{2} \left(\frac{2^{n/6}}{n-6} \right) \qquad \alpha = \frac{n}{2(n-6)}. \tag{3.4}$$

The parameters λ and α are chosen such that the well depth and radial location of the minimum of the generalized $(n, 6)$ potentials coincide with the minimum of the standard $(12, 6)$ Lennard-Jones potential. A detailed discussion of the thermodynamic and dynamic properties of binary mixture systems interacting via this family of potentials is given in Chapter 2[49]. In this chapter, we will use a representative sample of potentials defined by Eq. 3.3, with $n = 7, 9$, and 12. For each interaction potential, we apply the well-known Kob and Andersen binary glass-forming mixture parameterization[50], namely, a mixture of 80% A particles and 20% B particles, with parameters $\epsilon_{AA} = 1.0$, $\epsilon_{BB} = 0.5$, $\epsilon_{AB} = 1.5$, $\sigma_{AA} = 1.0$, $\sigma_{BB} = 0.88$, and $\sigma_{AB} = 0.8$. Both types of particles have the same mass, m. For these atomic systems, all quantities are expressed in reduced units: length in units of σ_{AA}, temperature in units of ϵ_{AA}/k_B, and time in units of $\sigma_{AA}(m/\epsilon_{AA})^{1/2}$. In order to ensure continuity of the potential and its first derivative at a cutoff distance r_c, we apply a shifted force (sf) correction to the potentials:

$$\phi^{sf}(r) = \begin{cases} \phi(r) - \phi(r_c) - (r - r_c)\phi'(r_c) & r \leq r_c \\ 0 & r > r_c \end{cases}. \tag{3.5}$$

To minimize the effects of the shift on the shape of the various potentials, a rather large cutoff of $r_c = 3.5$ is chosen.

3.2.2 Model Molecular System

For our molecular system, we choose the Lewis and Wahnström model for *ortho*-terphenyl[51] (1,2-diphenylbenzene, OTP). In this model each phenyl ring is represented by a Lennard-Jones site ($\epsilon = 5.276$ kJ/mol, $\sigma = 4.83$ Å), and the three sites constitute a rigid isosceles triangle, with a vertex angle of 75° and a bond length of 4.83 Å for the two equal sides. For simplicity, each site is assigned the same mass of $m = 78$ g/mol. Although this is a somewhat simplistic model for OTP, it allows us to observe how the results from the atomic systems change when rotational degrees of freedom are added. The rigid bond constraints are maintained by the SHAKE algorithm, and for

the OTP simulations, all quantities are expressed in real units.

3.2.3 Viscosity and Structural Relaxation Time

In molecular dynamics simulations, the shear viscosity can be calculated by a Green-Kubo time-correlation relation[48]:

$$\eta = \frac{V}{k_B T} \int_0^\infty \mathrm{d}t \, \langle P_{xy}(0) P_{xy}(t) \rangle \,, \tag{3.6}$$

where P_{xy} is an off-diagonal element of the stress tensor, given by

$$P_{xy} = \frac{1}{V} \left[\sum_i m_i v_{ix} v_{iy} + \sum_i \sum_{j>i} (r_{ix} - r_{jx}) F_{ijy} \right], \tag{3.7}$$

where v_{ix} and v_{iy} are respectively the x and y components of the velocity vector for atom i, and F_{ijy} is the y component of the force on atom i due to atom j. We use the "atomic" form of the virial to calculate the pressure tensor[52, 53], i.e., the sums are over each individual "atom" (force center) in the system, and the double summation virial term includes contributions from intra-molecular constraint forces, should any exist.

By exploiting the tensorial properties of the viscosity constant, Daivis and Evans[54] have shown that it is possible to incorporate all elements of the pressure tensor into the calculation of viscosity to improve statistics. The Green-Kubo relation then becomes[55]

$$\eta = \frac{V}{10 k_B T} \int_0^\infty \mathrm{d}t \sum_{\alpha\beta} \langle P_{\alpha\beta}(0) P_{\alpha\beta}(t) \rangle \,, \tag{3.8}$$

where $\alpha\beta = xx, yy, zz, xy, xz, yx, yz, zx, zy$,

$$P_{\alpha\beta} = (\pi_{\alpha\beta} + \pi_{\beta\alpha})/2 - \delta_{\alpha\beta} \left(\sum_\gamma \pi_{\gamma\gamma} \right) /3, \tag{3.9}$$

and

$$\pi_{\alpha\beta} = \frac{1}{V} \left[\sum_i m_i v_{i\alpha} v_{i\beta} + \sum_i \sum_{j>i} (r_{i\alpha} - r_{j\alpha}) F_{ij\beta} \right]. \tag{3.10}$$

The 1/10 prefix in Eq. 3.8 follows from the fact that the stress tensor is symmetric and consists of five independent components[56]: P_{xy}, P_{yz}, P_{xz}, $P_{xx} - P_{yy}$, $P_{yy} - P_{zz}$.

We define a characteristic structural relaxation time by using the self-intermediate scattering function $F_s(k,t) = \langle \exp[i\mathbf{k} \cdot \Delta\mathbf{r}(t)] \rangle$, where $\mathbf{k}$ is a chosen wave vector and $\Delta\mathbf{r}(t)$ is the center-of-mass

displacement experienced by an atom or molecule in time t. In each of the systems, the magnitude of the wave vector $\mathbf{k}$ is chosen to correspond to the first peak of the molecular center-of-mass static structure factor. The relaxation time τ is then defined by $F_s(k,\tau) = 1/e$.

3.3 Results and Discussion

3.3.1 The Stokes-Einstein Relations for a Softened Atomic System

We compute the three forms of the Stokes-Einstein ratio: $D\eta/T$, $D\tau/T$, $D\tau$, for our family of softened potentials for densities of $\rho = 1.2, 1.25$, and 1.3. Here, D corresponds to the diffusion coefficient of the A particles for the various potentials, and the wave number k used to calculate the self-intermediate scattering function corresponds to the first peak of the structure factor for the A-A interactions, $S_{AA}(k)$. While there has been experimental evidence that the Stokes-Einstein relation can break down for one component while holding for others in glass-forming alloys[57], we note that for our system the calculations based on either the A or B components are qualitatively similar, and the results we report here are calculated using the dynamic properties of the A particles.

In each case, we use a high temperature reference point at $T = 1.2$, which is well above the landscape onset temperature, below which mechanically stable packings sampled upon energy minimization begin to depend sensitively on the system's temperature prior to minimization[58]. The condition $T = 1.2$ thus corresponds to a state in which the system can freely sample all portions of energy landscape. Along each isochore we compute the ratio $\chi(T)/\chi(T = 1.2)$, where $\chi = D\eta/T$, $D\tau$, or $D\tau/T$. Any deviation away from the horizontal line of height 1 indicates a violation of the particular Stokes-Einstein relation under investigation.

In Figure 3.1, we plot the temperature dependence of the three ratios at a fixed density of $\rho = 1.25$ for $n = 7, 9$, and 12. Although all three ratios show a Stokes-Einstein violation at low enough temperatures, their behavior at higher temperatures exhibits pronounced differences. In particular, the "true" Stokes-Einstein relation, $D \propto T/\eta$, is in fact valid for a wide range of temperatures, regardless of n. The ratio $D\tau/T$ shows large deviations from unity across the entire temperature range investigated, and hence exhibits qualitatively different behavior. The product $D\tau$ approaches the Stokes-Einstein behavior as repulsions become steeper ($n = 12$). Note, however, that $D\tau$ actually exhibits a negative violation at high temperatures, an effect especially pronounced when the softness of the interaction potential is increased. Here, we use the terminology "negative violation" to denote the *decrease* of a Stokes-Einstein ratio below the high temperature limit, corresponding to an *increase*

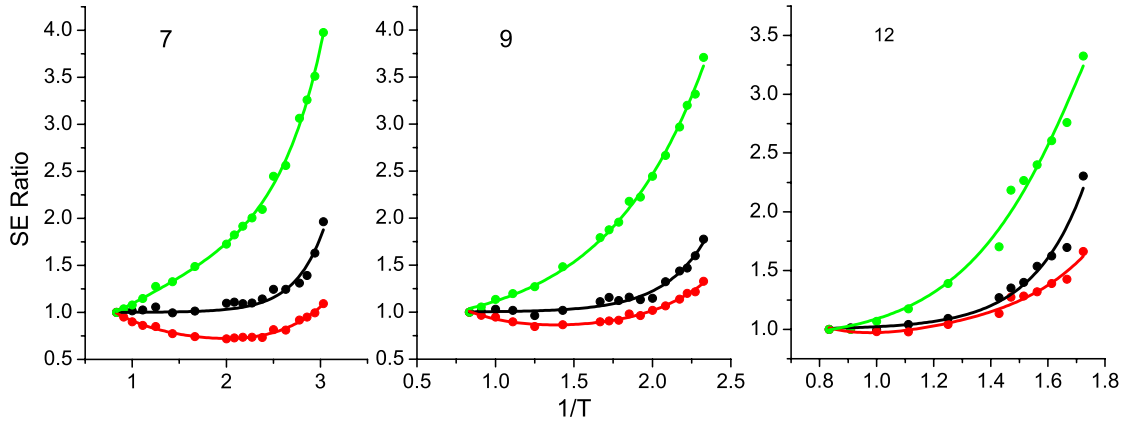

Figure 3.1: The Stokes-Einstein relations as a function of inverse temperature for a system interacting via softened potentials of $n = 7$ (left), 9 (center), and 12 (right). The Stokes-Einstein (SE) ratio is defined and color-coded as follows: $D\eta/T$ (black), $D\tau$ (red), and $D\tau/T$ (green), all normalized to their respective values at $T = 1.2$. Note the wide range in temperature where the Stokes-Einstein relation holds when viscosity is used to calculate the SE ratio.

of the effective hydrodynamic radius upon cooling.

For the case of $n = 7$, we also investigate how the three Stokes-Einstein relations change as the density of the system is varied (Figure 3.2). In all three cases, the large (positive) violation due to supercooling occurs at a higher temperature when the density is increased. This is a direct consequence of the increase in the landscape onset temperature[49] as the density is increased, effectively raising the temperature of the supercooled regime. However, the striking feature here is that the original Stokes-Einstein ratio that uses viscosity is indeed constant over a broad range of temperatures. Note again the negative Stokes-Einstein violation for the quantity $D\tau$, an effect that disappears gradually upon compression. Although $D\tau$ and $D\tau/T$ show the expected violation of Stokes-Einstein behavior at low temperatures, neither shows a range of temperatures where the quantity of interest remains constant, in marked contrast to $D\eta/T$.

3.3.2 The Stokes-Einstein Relations for OTP

In Figure 3.3, we plot the three Stokes-Einstein variants for the Lewis and Wahnström model of OTP. At liquid temperatures, the Stokes-Einstein relation is again valid when $D\eta/T$ is used for the calculation. However, in contrast to the atomic systems, none of the three ratios show a "negative violation" at higher temperatures. In fact, the results of Figure 3.3 suggest that for this particular system, the product $D\tau$ is actually a quite good substitute for the original Stokes-Einstein ratio of $D\eta/T$. This suggests that the validity of using a relaxation time instead of viscosity when studying

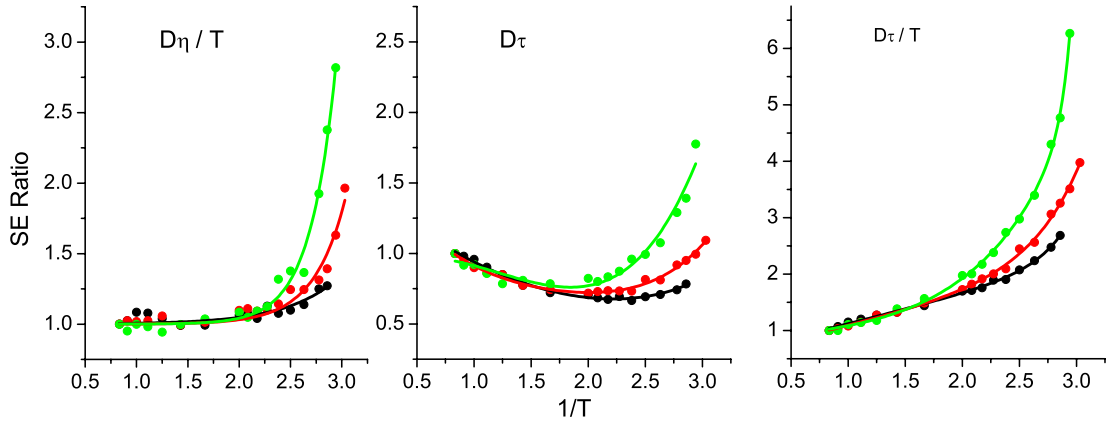

Figure 3.2: The three Stokes-Einstein relations plotted as a function of inverse temperature for a system interacting via a softened potentials of $n = 7$ for a density of $\rho = 1.2$ (black), 1.25 (red), and 1.3 (green). The Stokes-Einstein (SE) ratio is defined as $D\eta/T$ (left), $D\tau$ (center), and $D\tau/T$ (right), and all normalized to their respective values at $T = 1.2$. A horizontal line at 1 would indicate that the Stokes Einstein relation is observed.

Stokes-Einstein behavior depends on the specifics of the system being investigated; a substitution that works well for one system might not work well for another. As was the case for the family of systematically-softened atomic systems, the ratio $D\tau/T$, based on the approximation $\tau \sim \eta$, deviates very substantially from "Stokes-Einstein"-like behavior, $D\tau/T =$ constant, across the range of conditions investigated in this work for OTP.

3.3.3 The Instantaneous Shear Modulus and Stress Relaxation Time

For our atomic systems, neither of the substitutions $\tau \sim \eta$ or $\tau \sim \eta/T$ work very well, and in this section we seek to further clarify the relation between the shear viscosity and relaxation times. We begin by rewriting the Green-Kubo relation for viscosity (Eq. 3.8) as follows[59]:

$$\eta = \frac{V \sum_{\alpha\beta} \langle P_{\alpha\beta}(0) P_{\alpha\beta}(0) \rangle}{10 k_B T} \int_0^\infty \mathrm{d}t \frac{\sum_{\alpha\beta} \langle P_{\alpha\beta}(0) P_{\alpha\beta}(t) \rangle}{\sum_{\alpha\beta} \langle P_{\alpha\beta}(0) P_{\alpha\beta}(0) \rangle}. \tag{3.11}$$

The shear viscosity is commonly written as a product of an instantaneous shear modulus, G_∞ and a characteristic stress relaxation time, τ:

$$\eta = G_\infty \tau. \tag{3.12}$$

G_∞ is often approximated to be constant in temperature at constant density, in particular when studying Stokes-Einstein violation, because when a liquid undergoes supercooling, changes on the

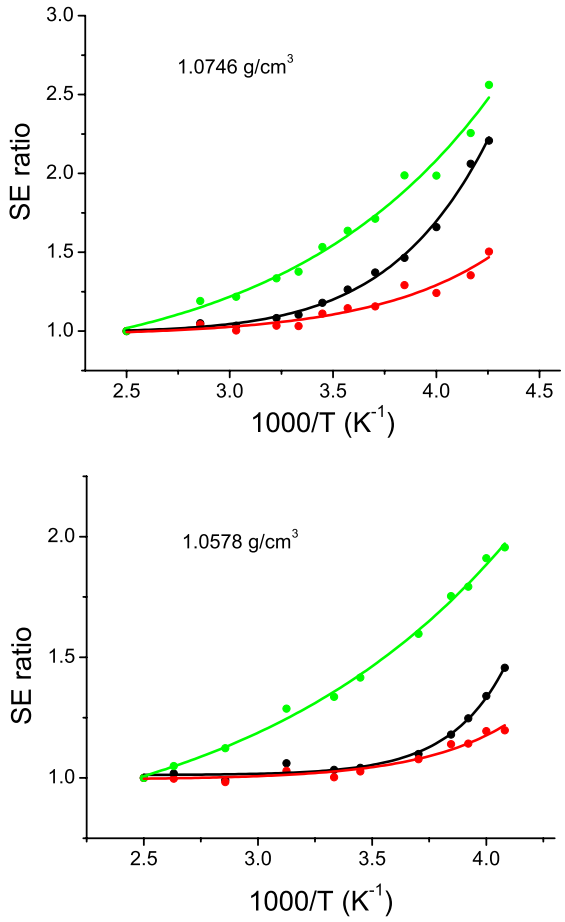

Figure 3.3: The three Stokes-Einstein relations plotted as a function of inverse temperature for a system of Lewis and Wahnström OTP molecules at a density of $\rho = 1.0746$ g/cm^3 (top) and 1.0578 g/cm^3 (bottom). The SE ratio is defined and color-coded as $D\eta/T$ (black), $D\tau$ (red), and $D\tau/T$ (green), all normalized to their respective values at $T = 400$ K. Note again the wide range in temperatures where the Stokes-Einstein relation holds when viscosity is used for the calculation.

right-hand side of Eq. 3.12 are dominated by the order of magnitude increases in τ. However, G_∞ does in fact have a slight temperature dependence[47], and we seek to investigate how this temperature dependence affects the qualitative differences observed at liquid temperatures between the Stokes-Einstein relations using η and those using τ.

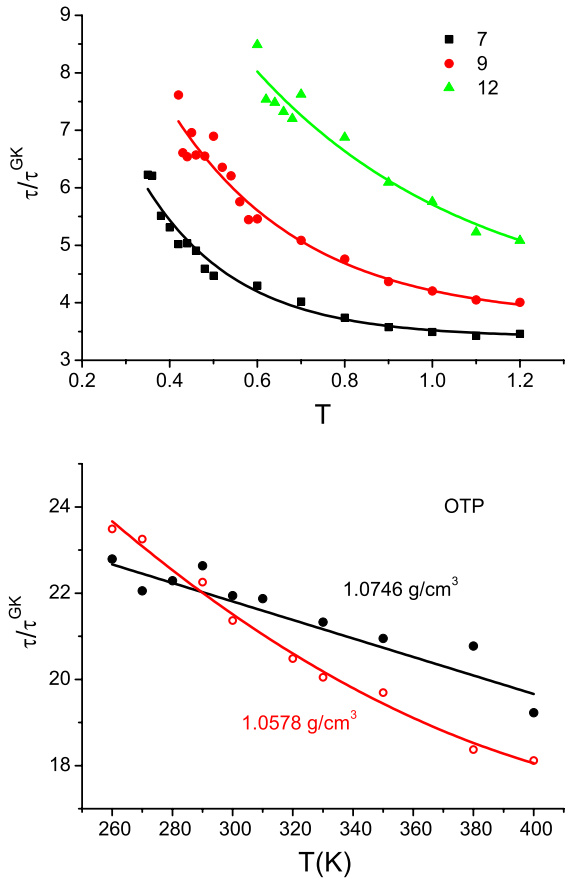

Figure 3.4: The ratio of the structural and stress relaxation times, τ/τ^{GK}, as a function of temperature for the softened potential systems (top, $\rho = 1.25$) and OTP (bottom, $\rho = 1.0746$ g/cm^3 and 1.0578 g/cm^3).

Comparing Eq. 3.11 and Eq. 3.12, we can define $G_\infty(T)$ and a corresponding Green-Kubo stress relaxation time τ^{GK}[59]:

$$G_\infty(T) = \frac{V \sum_{\alpha\beta} \langle P_{\alpha\beta}(0) P_{\alpha\beta}(0) \rangle}{10 k_B T}, \tag{3.13}$$

$$\tau^{GK} = \int_0^\infty \mathrm{d}t \frac{\sum_{\alpha\beta} \langle P_{\alpha\beta}(0) P_{\alpha\beta}(t) \rangle}{\sum_{\alpha\beta} \langle P_{\alpha\beta}(0) P_{\alpha\beta}(0) \rangle}. \tag{3.14}$$

Here, we have defined a new relaxation time, τ^{GK}, which we can now use to calculate Stokes-

Einstein ratios $D\tau^{GK}$ and $D\tau^{GK}/T$. Note that τ^{GK} is a *stress* relaxation time. Figure 3.4 compares τ^{GK} with τ, the *structural* relaxation time derived from the self-intermediate scattering function. It can seen that the temperature dependence of the ratio of relaxation times is non-trivial, with τ/τ^{GK} increasing markedly upon cooling. For the binary atomic mixtures, the ratio τ/τ^{GK} approaches a horizontal asymptote at high temperatures. This suggests a coupling of the structural and stress relaxation times at high temperatures, especially for the softer mixtures, and a progressive breakdown of this coupling as the temperature is decreased[60]. Figure 3.5 shows the resulting Stokes-Einstein ratios based on τ^{GK} for the binary atomic systems. We can see that the behavior of these curves, particularly for the softer mixtures, is qualitatively similar to those in Figure 3.1.

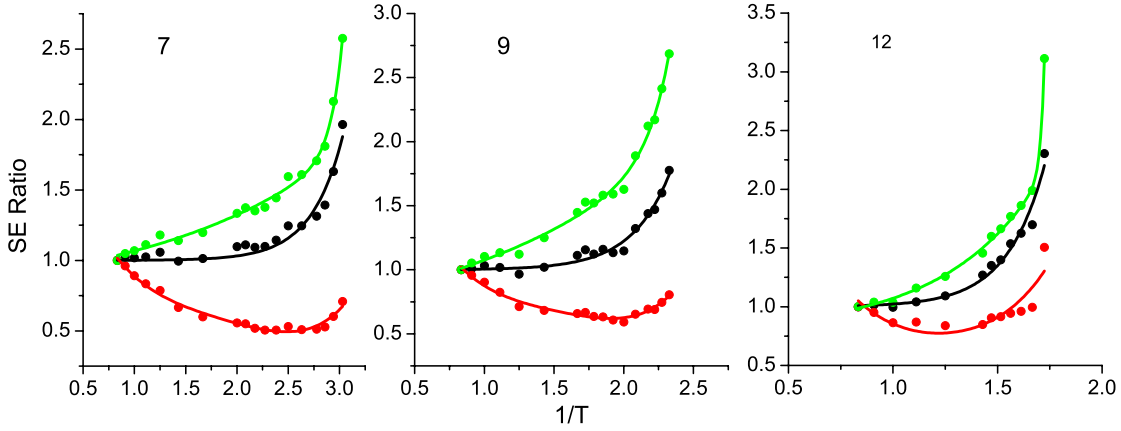

Figure 3.5: The Stokes-Einstein relations as a function of inverse temperature for a system interacting via softened potentials of $n = 7$ (left), 9 (center), and 12 (right). The SE ratio is defined and color-coded as follows: $D\eta/T$ (black), $D\tau^{GK}$ (red), and $D\tau^{GK}/T$ (green), all normalized to their respective values at $T = 1.2$. Here, the characteristic relaxation time τ^{GK} is derived from the Green-Kubo expression for viscosity and defined by Eq. 3.14. These curves behave qualitatively similarly to those of Figure 3.1, where a characteristic relaxation time derived from the self-intermediate scattering function was used in the calculation.

Figure 3.6 shows the temperature dependence of both G_∞ (in units of $\epsilon_{AA}/\sigma_{AA}^3$) and $G_\infty \cdot k_B T$, also for the binary atomic systems. If we substitute the functional forms for the best fit lines into Eq. 3.12, the relation between η and τ^{GK} can then be modeled as either $\tau^{GK} \propto \eta/(T + \text{const.})$ or $\tau^{GK} \propto \eta/T^b$, where $0.2 < b < 0.3$. We note that these models are intermediate between the commonly used proxy relations, $\tau \propto \eta$ and $\tau \propto \eta/T$. Indeed, as has already been discussed in connection with Figure 3.5, $\tau \propto \eta$ overestimates the viscosity contribution to the Stokes-Einstein relation, while $\tau \propto \eta/T$ underestimates it.

Figures 3.7 and 3.8 show the results of the same analysis when applied to the Lewis and Wahnström OTP systems. Similar to the softened potential systems, G_∞ increases with increasing tem-

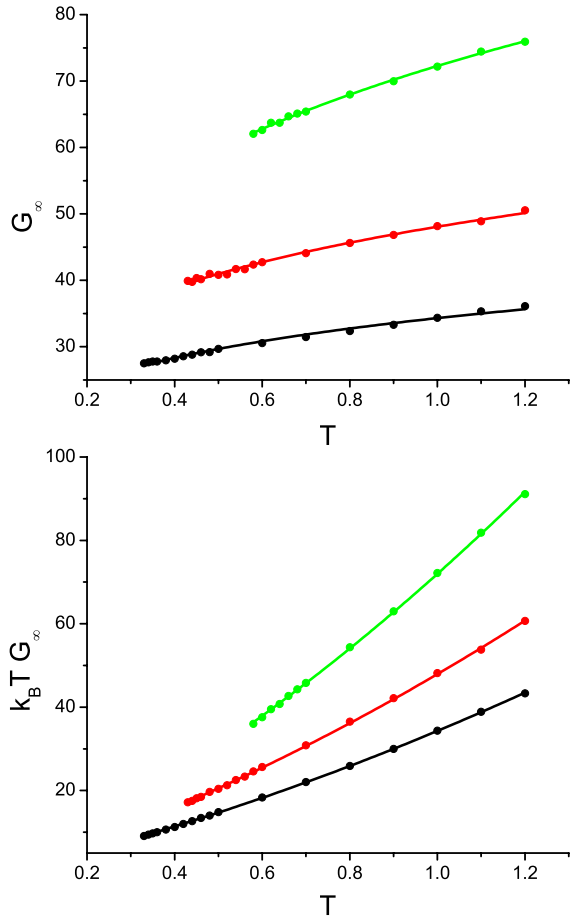

Figure 3.6: The temperature dependence of the instantaneous shear modulus, $G_\infty(T)$, as defined by Eq. 3.13, for a system density of $\rho = 1.25$. The three data sets in each graph correspond to softened potential interactions of $n = 7$ (black), 9 (red), and 12 (green). For the top graph, the fit lines are of the functional form aT^b, resulting in a fitting parameter of $a = 34.311, 48.070, 72.271$ and $b = 0.210, 0.231, 0.275$ respectively for $n = 7, 9, 12$. For the bottom graph, the fit lines are of the functional form $cT(T + d)$. The regressed values of c and d are $9.744, 13.611, 21.952$ and $2.518, 2.520, 2.278$ for $n = 7, 9, 12$, respectively.

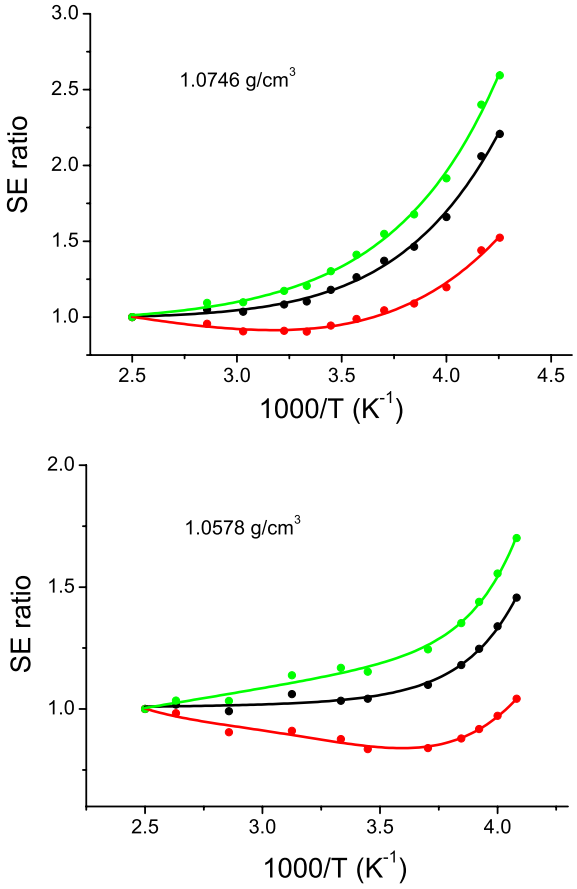

Figure 3.7: The Stokes-Einstein relations as a function of inverse temperature for a system of Lewis and Wahnström OTP molecules at a density of $\rho = 1.0746$ g/cm^3 (top) and 1.0578 g/cm^3 (bottom). The SE ratio is defined and color-coded as follows: $D\eta/T$ (black), $D\tau^{GK}$ (red), and $D\tau^{GK}/T$ (green), all normalized to their respective values at $T = 400$ K. The characteristic relaxation time used here is τ^{GK}, derived from the Green-Kubo expression for viscosity and defined by Eq. 3.14.

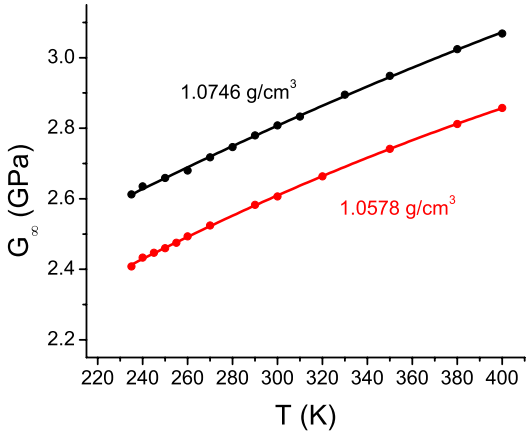

Figure 3.8: The temperature dependence of the instantaneous shear modulus, $G_\infty(T)$, for a system of Lewis and Wahnström OTP molecules at a density of $\rho = 1.0746$ g/cm^3 and 1.0578 g/cm^3. The lines are guides to the eye.

perature. However, $D\tau^{GK}$ now exhibits a negative violation of Stokes-Einstein behavior at higher temperatures. Collectively, these results show that the temperature dependence of G_∞ is non-trivial. Furthermore, when using relaxation time to investigate Stokes-Einstein validity over a broad range of temperatures, using a different relaxation time (e.g., structural or stress relaxation times) can result in a qualitatively different behavior. The validity of using a relaxation time as a substitute for viscosity is dependent on both the particular definition of the relaxation time used, and the specifics of the system under study.

3.4 Conclusions

In this chapter, we have examined three variants of the Stokes-Einstein ratio, namely $D\eta/T$, $D\tau$, and $D\tau/T$, for model atomic and molecular systems, over a broad range of temperatures and densities.

For the family of atomic binary systems investigated here, with τ a structural relaxation time, the ratio $D\tau/T$, based on the approximation $\tau \sim \eta$, increases upon cooling much faster than the true Stokes-Einstein ratio $D\eta/T$. The product $D\tau$, based on the approximation $\tau \sim \eta/T$, exhibits negative Stokes-Einstein violation at moderate temperatures, approaching the true Stokes-Einstein ratio as the repulsive component of the potential becomes progressively steeper. The increase upon cooling exhibited by the three Stokes-Einstein variants occurs at progressively higher temperatures as the fluids are compressed. As can be seen from Figures 3.1 and 3.2, the Stokes-Einstein ratio $D\eta/T$ is constant, to a very good approximation, over a broad range of thermodynamic conditions.

The molecular system we studied, the Lewis-Wahnström model of OTP, exhibits similar behavior, with one important difference: the product $D\tau$ is a reasonably accurate proxy for the Stokes-Einstein ratio across the conditions investigated here, and does not show negative violation of Stokes-Einstein behavior. This is consistent with the trend observed in the atomic systems, where the approximation $\tau \sim \eta/T$ gets better as the close range repulsion becomes steeper, since this OTP model consists of three Lennard-Jones sites connected by rigid bonds. For this system, too, $D\eta/T$ = constant is satisfied over an appreciable range of thermodynamic conditions: $300 \leq T \leq 400$ K at 1.0746 g/cm^3 and $280 \leq T \leq 400$ K at 1.0578 g/cm^3.

Different choices of relaxation times can affect the behavior of the Stokes-Einstein variants in non-trivial ways. In this work we considered two relaxation times. One, denoted simply by τ in this paper, is a structural relaxation time obtained from the decay of the self-intermediate scattering function; the other, τ^{GK}, is a stress relaxation time obtained from the Green-Kubo stress autocorrelation integral. While both relaxation times lead to similar behavior for the atomic binary mixtures, especially for the softer potentials, for the OTP system τ^{GK} leads to negative Stokes-Einstein violations in $D\tau^{GK}$, in contrast to $D\tau$ which does not show negative violations. Furthermore, the relationship between these two relaxation times displays a non-trivial temperature dependence, especially at low temperatures.

The often-invoked simple proportionality between viscosity and relaxation time is predicated on the assumed constancy of the instantaneous shear modulus, G_∞. Our numerical study of this quantity based on the Green-Kubo formalism reveals an appreciable temperature dependence for the two classes of systems investigated here, and G_∞ increases with temperature for both the atomic binary mixtures and OTP.

In this study, we have explored the effects of temperature changes under constant density conditions. Most experiments, on the other hand, are performed under isobaric conditions. It would be interesting to investigate numerically the extent to which the main observations reported here remain valid under the more experimentally-relevant isobaric conditions. Recent experiments suggest that in some glass-forming alloys the product $D\eta$ is constant while Stokes-Einstein violation occurs[61]; it would be interesting to explore computationally the extent to which this scaling applies more broadly to other systems.

The present calculations suggest that commonly-invoked assumptions, such as $\tau \sim \eta$ and $\tau \sim \eta/T$, deserve critical scrutiny when used to construct Stokes-Einstein variants. The behavior of $D\eta/T$, $D\tau$ and $D\tau/T$ needs to be investigated for a wider range of systems than the two considered here, and across as broad a range of temperatures and densities as possible. It is also of interest to

explore numerically the behavior of different relaxation times, only two of which have been considered here. It is hoped that such systematic numerical investigation will lead to a deeper understanding of relaxation processes in liquids at both supercooled and ambient conditions. Our approach in this work has been phenomenological. Numerical studies of the microscopic mechanisms underlying the rich behavior presented here constitute a natural direction for future studies.

We wish to stress in closing the remarkably broad range of conditions across which the Stokes-Einstein equation, meant to apply to supermolecular objects suspended in a fluid continuum, is also valid at the molecular level.

3.5 Acknowledgments

We thank Srikanth Sastry for suggesting to us the importance of exploring possible non-trivial relationships between viscosity and relaxation time. The financial support of the National Science Foundation is gratefully acknowledged (Grant CHE-1213343 to PGD). Calculations were performed at the Terascale Infrastructure for Groundbreaking Research in Engineering and Science (TIGRESS) at Princeton University.

Bibliography

[1] A. Einstein, Ann. Phys. **17**, 549 (1905).

[2] G. G. Stokes, Trans. Cambridge Philos. Soc. **9**, 8 (1851).

[3] L. M. Milne-Thomson, *Theoretical Hydrodynamics*, 4th ed. ed. (Macmillan Co., 1960), p. 584.

[4] D. H. Kumar *et al.*, Phys. Rev. Lett. **93**, 144301 (2004).

[5] M. T. Tyn and T. W. Gusek, Biotechnol. Bioeng. **35**, 327 (1990).

[6] M. E. Young, P. A. Carroad, and R. L. Bell, Biotechnol. Bioeng. **22**, 947 (1980).

[7] S. Rathgeber, M. Monkenbusch, M. Kreitschmann, V. Urban, and A. Brulet, J. Chem. Phys. **117**, 4047 (2002).

[8] M. Terazima, K. Okamoto, and N. Hirota, J. Phys. Chem. **97**, 5188 (1993).

[9] M. R. McCarthy, K. D. Vandegriff, and R. M. Winslow, Biophys. Chem. **92**, 103 (2001).

[10] J. P. Poirier, Geophys. J. **92**, 99 (1988).

[11] B. T. Poe *et al.*, Science **276**, 1245 (1997).

[12] S. G. Schultz and A. K. Solomon, J. Gen. Physiol. **44**, 1189 (1961).

[13] A. Noda, K. Hayamizu, and M. Watanabe, J. Phys. Chem. B **105**, 4603 (2001).

[14] J. Read *et al.*, J. Electrochem. Soc. **150**, A1351 (2003).

[15] C. Comminges, R. Barhdadi, M. Laurent, and M. Troupel, J. Chem. Eng. Data **51**, 680 (2006).

[16] D. P. Dobson, J. P. Brodholt, L. Vočadlo, and W. A. Crichton, Mol. Phys. **99**, 773 (2001).

[17] E. D. Snijder, M. J. M. te Riele, G. F. Versteeg, and W. P. M. van Swaaij, J. Chem. Eng. Data **38**, 475 (1993).

[18] S. F. Swallen, P. A. Bonvallet, R. J. McMahon, and M. D. Ediger, Phys. Rev. Lett. **90**, 015901 (2003).

[19] M. K. Mapes, S. F. Swallen, and M. D. Ediger, J. Phys. Chem. B **110**, 507 (2006).

[20] F. Mallamace *et al.*, J. Chem. Phys. **124**, 161102 (2006).

[21] R. Kind *et al.*, Phys. Rev. B **45**, 7697 (1992).

[22] K. L. Ngai, J. H. Magill, and D. J. Plazek, J. Chem. Phys. **112**, 1887 (2000).

[23] I. Chang *et al.*, J. Non-Cryst. Solids **172-174**, 248 (1994).

[24] T. G. Lombardo, P. G. Debenedetti, and F. H. Stillinger, J. Chem. Phys. **125**, 174507 (2006).

[25] G. Tarjus and D. Kivelson, J. Chem. Phys. **103**, 3071 (1995).

[26] F. Blackburn, M. T. Cicerone, G. Hietpas, P. A. Wagner, and M. Ediger, J. Non-Cryst. Solids **174**, 256 (1994).

[27] C. Rønne *et al.*, J. Chem. Phys. **107**, 5319 (1997).

[28] S. K. Kumar, G. Szamel, and J. F. Douglas, J. Chem. Phys. **124**, 214501 (2006).

[29] J. A. Hodgdon and F. H. Stillinger, Phys. Rev. E **48**, 207 (1993).

[30] M. D. Ediger, Annu. Rev. Phys. Chem **51**, 99 (2000).

[31] V. Lubchenko and P. G. Wolynes, Annu. Rev. Phys. Chem. **58**, 235 (2007).

[32] F. H. Stillinger, Science **267**, 1935 (1995).

[33] R. Zwanzig and A. K. Harrison, J. Chem. Phys. **83**, 5861 (1985).

[34] L. Berthier, D. Chandler, and J. P. Garrahan, Europhys. Lett. **69**, 320 (2005).

[35] K. L. Ngai, J. Phys. Chem. B **103**, 10684 (1999).

[36] G. Diezemann, H. Sillescu, G. Hinze, and R. Böhmer, Phys. Rev. E **57**, 4398 (1998).

[37] F. H. Stillinger and J. A. Hodgdon, Phys. Rev. E **50**, 2064 (1994).

[38] J.-L. Barrat, J.-N. Roux, and J.-P. Hansen, Chem. Phys. **149**, 197 (1990).

[39] D. Thirumalai and R. D. Mountain, Phys. Rev. E **47**, 479 (1993).

[40] D. Jeong, M. Y. Choi, H. J. Kim, and Y. Jung, Phys. Chem. Chem. Phys. **12**, 2001 (2010).

[41] S. H. Lee and T. Chang, Bull. Korean Chem. Soc. **24**, 1590 (2003).

[42] Y. Jung, J. P. Garrahan, and D. Chandler, Phys. Rev. E **69**, 061205 (2004).

[43] R. Yamamoto and A. Onuki, Phys. Rev. Lett. **81**, 4915 (1998).

[44] S.-H. Chen *et al.*, Proc. Natl. Acad. Sci. U.S.A **103**, 12974 (2006).

[45] P. Kumar *et al.*, Proc. Natl. Acad. Sci. U.S.A **104**, 9575 (2007).

[46] L. Xu *et al.*, Nat. Phys. **5**, 565 (2009).

[47] N. B. Olsen, J. C. Dyre, and T. Christensen, Phys. Rev. Lett. **81**, 1031 (1998).

[48] J. P. Hansen and I. R. McDonald, *Theory of Simple Liquids*, 2nd ed. ed. (Academic Press, 1986), chap. 8.

[49] Z. Shi, P. G. Debenedetti, F. H. Stillinger, and P. Ginart, J. Chem. Phys. **135**, 084513 (2011).

[50] W. Kob and H. C. Andersen, Phys. Rev. E **51**, 4626 (1995).

[51] L. J. Lewis and G. Wahnström, Phys. Rev. E **50**, 3865 (1994).

[52] D. N. Theodorou, T. D. Boone, L. R. Dodd, and K. F. Mansfield, Makromol. Chem., Theory Simul. **2**, 191 (1993).

[53] A. P. Thompson, S. J. Plimpton, and W. Mattson, J. Chem. Phys. **131**, 154107 (2009).

[54] P. J. Daivis and D. J. Evans, J. Chem. Phys. **100**, 541 (1994).

[55] S. H. Lee and T. Y. Chang, Bull. Korean Chem. Soc. **24**, 1590 (2003).

[56] D. Nevins and F. J. Spera, Mol. Simulat. **33**, 1261 (2007).

[57] A. Bartsch, K. Rätzke, A. Meyer, and F. Faupel, Phys. Rev. Lett. **104**, 195901 (2010).

[58] S. Sastry, P. G. Debenedetti, and F. H. Stillinger, Nature **393**, 554 (1998).

[59] J. C. Dyre and W. H. Wang, J. Chem. Phys. **136**, 224108 (2012).

[60] We note that as the temperature is further decreased below the data points shown in Figure 3.4, τ/τ^{GK} appears to reach a maximum, and decreases upon further cooling. However, further numerical precision is required to obtain accurate low temperature values of τ/τ^{GK}, and we are presently investigating in detail the low temperature relation between τ and τ^{GK}.

[61] J. Brillo, A. I. Pommrich, and A. Meyer, Phys. Rev. Lett. **107**, 165902 (2011).

Chapter 4

Anomalies of Water: Viscosity and Stokes-Einstein Violation

4.1 Introduction

Although it is the most common of liquids, water is also one of the most peculiar because it exhibits a number of anomalous properties. For example, at atmospheric pressure, it has a density maximum at 277 K, an isobaric heat capacity minimum at 308 K, and an isothermal compressibility minimum at 319 K[1]. Another well-known anomaly is that, at sufficiently cold temperatures, the viscosity of water decreases upon compression[2–4]. However, to date, the majority of the computational studies of water viscosity have only sampled a limited set of state points. Some of these studies focus on comparisons of viscosities calculated using various computational methods[5, 6] or different water models[7–13]. The effects of solution composition[14] and of confinement[15] on the viscosity of water have also been explored. In this study, we focus on the SPC/E model of water[16], but provide a detailed investigation of the behavior of viscosity across a wide range of temperatures and densities.

We choose the SPC/E model for this study to allow us to relate our results to an influential computational work on water anomalies, published in 2001 by Errington and Debenedetti[17]. That work focused on the relationship between the structural order and the transport and thermodynamic anomalies of SPC/E water. Structural anomalies, where order decreases upon isothermal compression, are observed over the broadest range of temperatures and densities. The region of diffusivity anomalies, where the diffusion coefficient increases upon isothermal compression, is completely

contained within the region of structural anomalies. Thermodynamic anomalies, where density decreases upon isobaric cooling, occur entirely within the region of diffusivity anomalies. These regions constitute a cascade triggered by increasing structural order. Furthermore, within the structurally anomalous region, the orientational and translational order are strongly coupled.

A comprehensive viscosity data set for SPC/E water also allows us to study a related phenomenon, namely the breakdown of Stokes-Einstein behavior. The Stokes-Einstein equation[18],

$$D = \frac{k_B T}{C \eta a}, \tag{4.1}$$

was originally derived to describe the diffusion of a macroscopic sphere suspended in a viscous fluid; D is the diffusion coefficient of spheres of radius a, and η is the shear viscosity of the surrounding fluid at temperature T. C is a constant that depends on the boundary conditions at the sphere-fluid interface, and ranges from 6π for no-slip to 4π for slip boundary conditions[19]. However, a molecular-level version of Eq. 4.1, where D now represents the self-diffusion coefficient of a uniform fluid, has been found experimentally to be valid over a wide range of temperatures for many liquids[20–27]. For a given liquid, we can then define a quantity, $D\eta/T$, whose constancy, or lack thereof, over a range of thermodynamic conditions, serves as a measure of the validity of the Stokes-Einstein equation at the molecular level. One then says that the Stokes-Einstein equation is valid when

$$\frac{D\eta}{T} = \text{constant}, \tag{4.2}$$

and any deviations away from Eq. 4.2 would indicate a Stokes-Einstein violation.

A well-known condition where Stokes-Einstein violation occurs is when a liquid undergoes deep supercooling[25–30], where the rate at which the viscosity increases decouples from that at which the self-diffusion coefficient decreases, and $D\eta/T$ deviates strongly from Eq. 4.2. However, the rotational analog of Eq. 4.1 (known as the Stokes-Einstein-Debye equation[31]), $D_r = k_B T/C'\eta a^3$, where D_r is the rotational diffusion coefficient and C' is a numerical constant, can remain valid even when Eq. 4.2 begins to break down[32–34]. This further decoupling of translational and rotational diffusion has been explained by invoking dynamic heterogeneity, which refers to the presence of transient spatially separated regions with vastly different relaxation times[31]. The microscopic origin of this supercooled Stokes-Einstein violation, and of the decoupling between translational and rotational motion, is a topic of considerable research interest[35–44]. Previous studies have invoked the Stokes-Einstein equation for water, and although it has been tested over a limited set

of conditions[45–48], a comprehensive study of the validity, and breakdown, of the Stokes-Einstein equation for water across a wide range of densities is still lacking.

Additionally, in computational studies, it has become increasingly common to reinterpret the physical meaning of the Stokes-Einstein relation simply as the product of a diffusion coefficient and a relaxation time, and many studies of the Stokes-Einstein violation use a structural relaxation time, τ, as a substitute for the viscosity η[32, 46–52]. The main reason underlying this common approximation is computational expediency. The functional form of the relation between τ and η varies among different studies; the two most often used are $\tau \propto \eta$[46–48] and $\tau \propto \eta/T$[32, 49–52]. $\tau \propto \eta/T$ results from the Gaussian solution to the diffusion equation[53], given by $F_s(k,t) = \exp(-k^2 Dt) \equiv \exp(-t/\tau)$, where $F_s(k,t)$ is the self-intermediate scattering function and k is the associated wave vector. It follows then that $D \propto 1/\tau$, which implies $\tau \propto \eta/T$, and replaces $D\eta/T$ in Eq. 4.2 with $D\tau$. The second proportionality, $\tau \propto \eta$, is based on the expression $\eta = G_\infty \tau^{GK}$, where G_∞ is the instantaneous shear modulus, and τ^{GK} is now a *stress* relaxation time. Here, G_∞ is treated as a constant. The relation $\tau \propto \eta$ then gives $D \propto T/\tau$, and thus replaces $D\eta/T$ in Eq. 4.2 with $D\tau/T$.

Many computational studies of Stokes-Einstein behavior focus on temperature ranges where violation is expected to occur, and small temperature changes result in order of magnitude changes in both τ and η. Even though the relations $\tau \propto \eta$ and $\tau \propto \eta/T$ differ by a factor of $1/T$, in the supercooled regime, both can appear to be reasonable approximations that result in a strong Stokes-Einstein violation. Thus, it is then commonly assumed that a relaxation time is an adequate substitute for viscosity when studying Stokes-Einstein behavior, and that the structural relaxation time, τ, and stress relaxation time, τ^{GK} are interchangeable. Both of these assumptions have been challenged in Chapter 3[54] that studied the Stokes-Einstein behavior of model atomic and molecular systems. For those systems, while the ratios $D\eta/T$, $D\tau$, and $D\tau/T$ all show pronounced increases at low enough temperatures, only $D\eta/T$ is constant at higher temperatures. Furthermore, the qualitative behaviors of $D\tau$ and $D\tau/T$ are dependent on which relaxation time (structural or stress) is used.

In this chapter, we present a detailed investigation of the viscosity of SPC/E water[16] over a wide range of thermodynamic conditions, and map the region where viscosity behaves anomalously. Using this viscosity data set, we also provide an analysis of the Stokes-Einstein behavior for SPC/E water. Furthermore, we continue[54] the discussion of the relationship between the structural and stress relaxation times, and the validity of the Stokes-Einstein variants based upon them. In Section 4.2 we provide details of the computational methods utilized in our investigation. The main results

and discussion of SPC/E viscosity, Stokes-Einstein behavior, and relaxation times are presented in Section 4.3. Finally, the principal conclusions and suggestions for further study are presented in Section 4.4.

4.2 Methods

We use a comprehensive set of molecular dynamics simulations, at constant temperature and fixed density (N, V, T), to sample the wide range of thermodynamic conditions needed for this study. Numerical integration of the equations of motion was performed by using the LAMMPS molecular dynamics simulation package[55]. For a given density ρ and temperature T, the position and orientation of 1060 SPC/E water molecules are randomized in a periodic cubic cell of box length $(Nm_w/\rho)^{1/3}$, where $m_w = 18.0$ g/mol is the molecular mass of water. The particle-particle particle-mesh (pppm) method was used for long-range Coulombic interactions, and the target temperature is maintained by a Nosé-Hoover thermostat[56]. The system is first equilibrated for 0.5 ns, after which a 20 ns production run is used for analysis. The length of equilibration corresponds to 100 times the stress relaxation time at the lowest temperature investigated (220 K). To further verify equilibration, we track the total energy of the system, which is found to be within 1.5% of its mean value throughout the production run.

We calculate the shear viscosity by using the Daivis and Evans formulation of the Green-Kubo relation[57], where all elements of the pressure tensor are used in order to improve statistics[54]:

$$\eta = \lim_{t\to\infty} \frac{1}{10}\frac{V}{k_B T}\int_0^t \mathrm{d}t' \sum_{\alpha\beta} \langle P_{\alpha\beta}(0) P_{\alpha\beta}(t')\rangle \,, \tag{4.3}$$

where $\alpha\beta = xx, yy, zz, xy, xz, yx, yz, zx, zy$,

$$P_{\alpha\beta} = (\pi_{\alpha\beta} + \pi_{\beta\alpha})/2 - \delta_{\alpha\beta}\left(\sum_{\gamma} \pi_{\gamma\gamma}\right)/3. \tag{4.4}$$

Here,

$$\pi_{\alpha\beta} = \frac{1}{V}\left[\sum_i m_i v_{i\alpha} v_{i\beta} + \sum_i \sum_{j>i} (r_{i\alpha} - r_{j\alpha}) F_{ij\beta}\right] \tag{4.5}$$

is the virial expression for the stress tensor, where $v_{i\alpha}$ and $v_{i\beta}$ are respectively the α and β components of the velocity vector for atom i, and $F_{ij\beta}$ is the β component of the force on atom i due to atom j[58, 59]. The 1/10 prefix in Eq. 4.3 results from the stress tensor being symmetric and

consisting of five independent components[60]: P_{xy}, P_{yz}, P_{xz}, $P_{xx} - P_{yy}$, $P_{yy} - P_{zz}$. The integral is evaluated numerically, and the upper limit is taken to be the time when the long-term tail of the stress correlation function crosses zero for the third time; the value of this integral corresponds to the limiting value of the running integral in Eq. 4.3. Figure 4.1 gives an example of a typical viscosity calculation, and shows reasonable agreement between the shear viscosity values calculated in our study and experimental values given by the NIST Chemistry WebBook[61](Figure 4.2). Consistent with previous studies[7–10], we find that the SPC/E model slightly underestimates the shear viscosity.

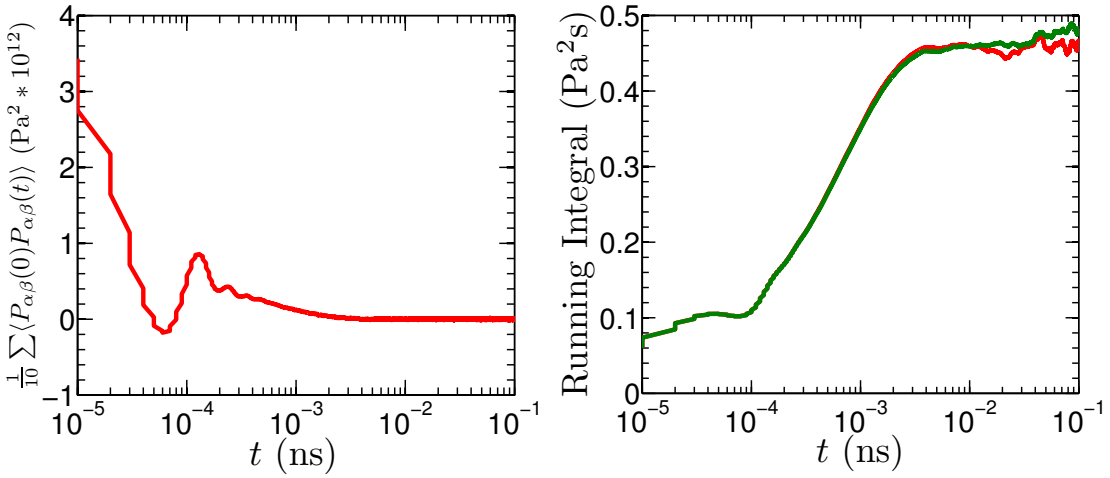

(a) (b)

Figure 4.1: The stress correlation function and associated running integral for a viscosity calculation by using Eq. 4.3, for a system of density 1.0 g/cm^3 and temperature 280 K. The red curves correspond to the calculation by using all elements of the pressure tensor (Eq. 4.3). An equivalent calculation (green curves) which uses only the off-diagonal elements of the pressure tensor is also included for comparison. In this study, the simulation runs are long enough such that the two curves superimpose on top of each other.

Diffusion coefficients are calculated by using the well-known Einstein equation:

$$D = \frac{1}{6} \lim_{t\to\infty} \frac{\mathrm{d}}{\mathrm{d}t} \left\langle \Delta r(t)^2 \right\rangle, \tag{4.6}$$

where D is the diffusion coefficient, and $\left\langle \Delta r(t)^2 \right\rangle$ is the center-of-mass mean squared displacement of water molecules after an interval of time t. Figure 4.3 shows the mean-squared-displacement curves for $\rho = 1.0$ g/cm^3. Diffusive behavior is indicated by the region where a mean-squared displacement curve becomes linear. Here, for any given temperature and density, the diffusion coefficient is

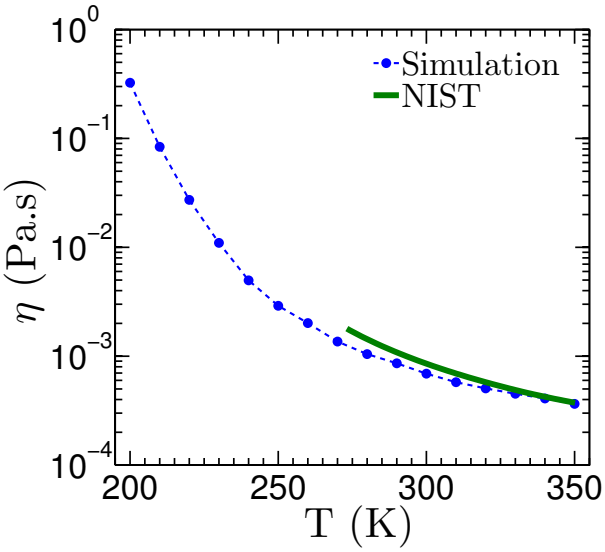

Figure 4.2: Comparison of SPC/E water viscosity calculated by Eq. 4.3 to data obtained from the NIST Chemistry WebBook[61] at a density of 0.983 g/cm^3.

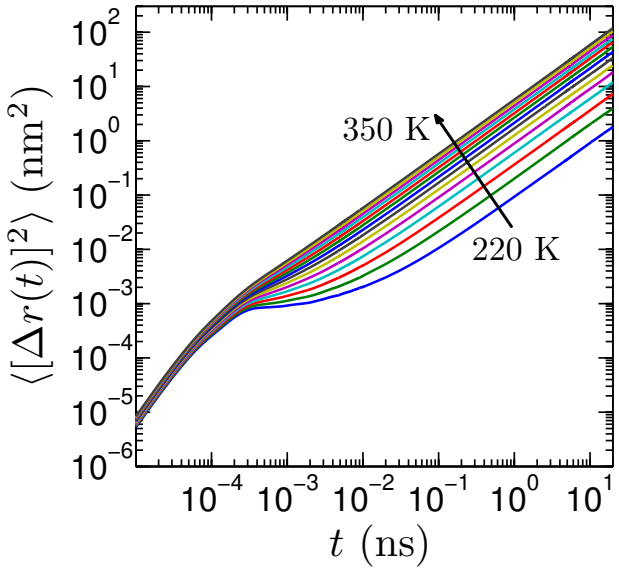

Figure 4.3: Evolution of the mean squared displacement for SPC/E water corresponding to different temperatures at a density of 1.0 g/cm^3. The increment between curves is 10 K. Caging is evident at the lowest temperatures, but becomes less prominent as the temperature is increased. From these curves, the slope of the linear regime is used to compute the diffusion coefficient.

determined by calculating the slope of the linear fit over the interval $t \in [6.67, 13.33]$ ns.

We define two different relaxation times in this study[54]. The first, which we will call the "structural" relaxation time and will label simply as τ, is derived from the self-intermediate scattering function, $F_s(k,t) = \langle \exp[i\mathbf{k} \cdot \Delta\mathbf{r}(t)] \rangle$, where $\mathbf{k}$ is a chosen wave vector and $\Delta\mathbf{r}(t)$ is the center-of-mass displacement experienced by an atom or molecule in time t. The magnitude of the wave vector $\mathbf{k}$ is chosen to be constant, and corresponds to the first peak of the molecular center-of-mass static structure factor of a system at $\rho = 1.0$ g/cm^3. The structural relaxation time τ is then defined by $F_s(k,\tau) = 1/e$.

The shear viscosity is commonly written[62] as a product of an instantaneous shear modulus, G_∞ and a characteristic stress relaxation time, τ^{GK}:

$$\eta = G_\infty \tau^{GK}. \tag{4.7}$$

This relaxation time can be derived by comparing Eq. 4.7 to the Green-Kubo equation for viscosity (Eq. 4.3). This "stress" relaxation time, which we will label as τ^{GK}, is thus defined as

$$\tau^{GK} = \int_0^\infty \mathrm{d}t \frac{\sum_{\alpha\beta} \langle P_{\alpha\beta}(0) P_{\alpha\beta}(t) \rangle}{\sum_{\alpha\beta} \langle P_{\alpha\beta}(0) P_{\alpha\beta}(0) \rangle}, \tag{4.8}$$

and the instantaneous shear modulus as

$$G_\infty = \frac{V \sum_{\alpha\beta} \langle P_{\alpha\beta}(0) P_{\alpha\beta}(0) \rangle}{10 k_B T}. \tag{4.9}$$

4.3 Results and Discussion

4.3.1 Viscosity

In this section, we present the viscosity values for SPC/E water across a wide range of thermodynamic conditions, and then map the region of viscosity anomalies on a (ρ, T) phase diagram. Figure 4.4 shows the temperature (T) dependence of viscosity (η) for various densities (ρ). The solid line fits here are of the Vogel-Fulcher-Tammann (VFT) form:

$$\log \eta = \frac{A}{T - T_0} + B, \tag{4.10}$$

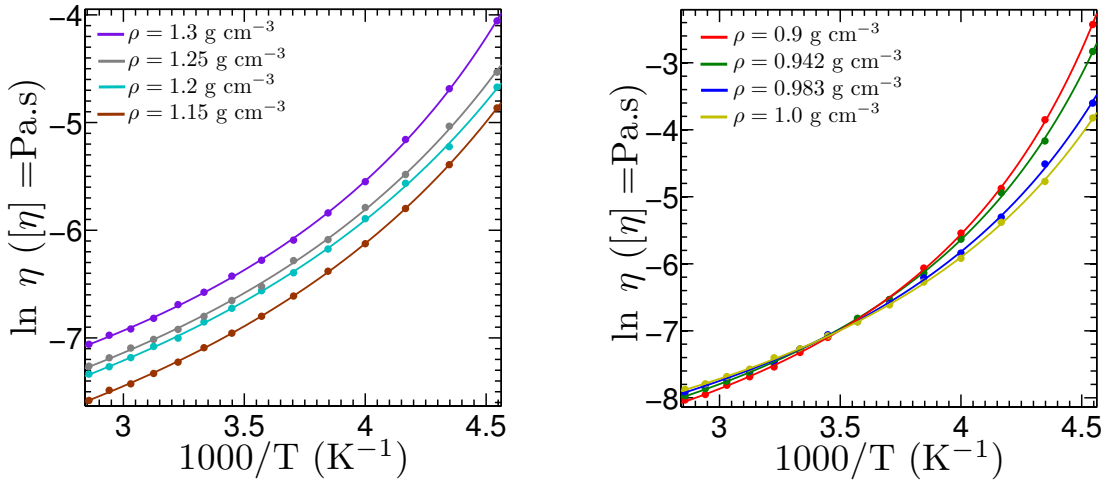

Figure 4.4: Viscosity as a function of inverse temperatures for various densities. The solid lines are VTF fits to the data. (a) High density behavior. (b) Low density behavior.

where T_0, A, and B are fitting parameters. The raw viscosity data values and the associated VTF fit parameters are presented in Appendix 4.A. At high densities (Figure 4.4a), the isochores exhibit "normal" liquid behavior: the viscosity increases with density, or, equivalently, pressure, at fixed temperature. However, at lower densities (Figure 4.4b), intersection occurs between isochores, an indication of anomalous behavior, where now at low enough temperatures, an increase in density results instead in a *decrease* in viscosity. This anomaly is also evident by examining the VTF T_0 values (Figure 4.5). For a typical liquid, these asymptotic values increase monotonically with density, a direct consequence of viscosity decreasing with temperature at fixed density. However, water also behaves anomalously in this regard, and for $\rho \leq 1.1$ g/cm^3, the asymptotic VTF T_0 values *decrease* upon compression.

We can further investigate this anomalous behavior by plotting the collection of viscosity values as a function of density, with each curve now corresponding to a different temperature (Figure 4.6). From this set of curves, the anomalous region for viscosity, where η decreases as ρ increases at fixed temperature, is clearly evident, and becomes particularly pronounced at the lowest temperatures. Using fifth-order polynomial fits, we calculate the locus of the local maxima and minima for these curves. This gives the density range of anomalous viscosity behavior for each given temperature. This set of extrema points can then be collected onto a single curve on the (ρ, T) plane, the interior of which represents the region where water behaves anomalously with respect to viscosity (Figure 4.7a). The method of obtaining the locus of local maxima, and their associated error bars, is explained in Appendix 4.B. For comparison, this dome-shaped curve is overlaid with the loci of structural,

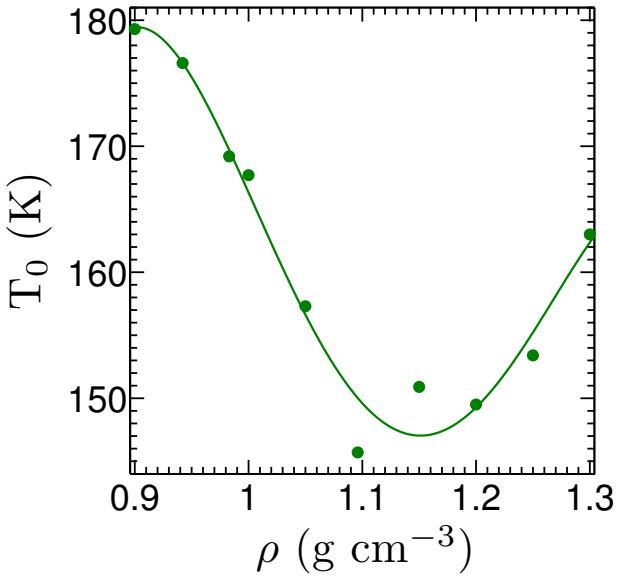

Figure 4.5: VTF asymptotic temperatures, as defined by Eq 4.10. The line is a guide to the eye.

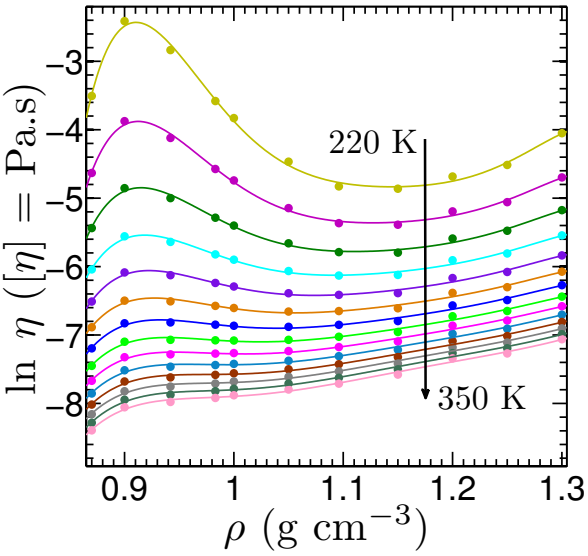

Figure 4.6: Density dependence of the viscosity of SPC/E water at different temperatures. The increment between adjacent curves is 10 K. The solid points here are obtained from the VTF fits (see Appendix 4.A for the raw viscosity data and fitted VTF parameters). The values from the VTF fits are used here to reduce noise, and this smoothing allows us to calculate the local maxima and minima of each curve by using 5th order polynomials, shown in solid lines.

diffusive, and thermodynamic anomalies calculated previously by Errington and Debenedetti[17] (Figure 4.7b).

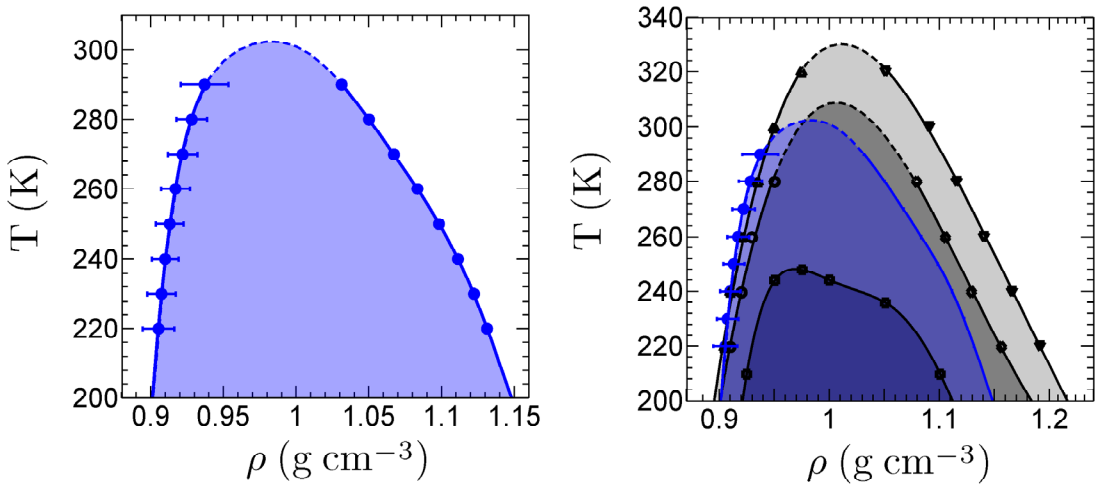

Figure 4.7: (a) Dome of viscosity anomalies for SPC/E water. At each temperature, the points correspond to the local maxima and minima of the $\eta(\rho)$ curves (see Figure 4.6). The shaded region is thus anomalous, in that viscosity *decreases* upon compression. Error bars indicate the range of uncertainties in the location of the low-density onset of viscosity anomalies (see Appendix 4.B for details). (b) The dome of viscosity anomalies shown in conjunction with the domes of structural, diffusivity, and thermodynamic anomalies previously computed by Errington and Debenedetti[17] for SPC/E water.

From the sequence of domes in Figure 4.7b, we see that the onset of anomalous behavior occurs in a specific, hierarchical fashion. The structural anomaly occurs first; here metrics of translational and orientational order both *decrease* upon compression[17]. The next onset of anomalous behavior is that of the kinetic processes, namely diffusivity and viscosity. In this region, mobility increases upon compression, which is caused by pressure-induced distortion of the hydrogen bond network. Finally, the thermodynamic anomaly occurs, where a lowering of the temperature results in volumetric expansion.

4.3.2 Stokes-Einstein Violations

For our system of SPC/E water molecules, we compute the diffusion coefficients by using Einstein's equation (Figure 4.8). These values agree well with those reported previously by Errington and Debenedetti[17], and anomalous behavior is clearly evident by the non-monotonic curves, showing an *increase* in diffusivity upon compression at sufficiently low temperatures. Similar to the viscosity data, we fit the diffusion coefficients along each isochore to the VTF equation; the raw diffusivity

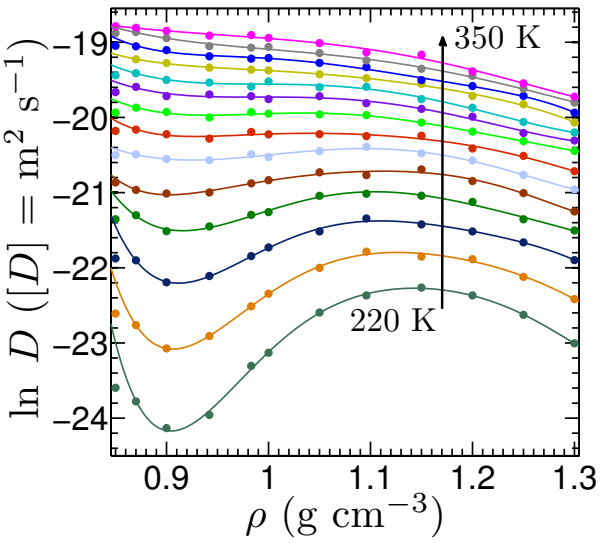

Figure 4.8: Density dependence of the diffusivity of SPC/E water at different temperatures. The increment between adjacent curves is 10 K. For a given isotherm, anomalous behavior corresponds to the density range where diffusivity increases upon compression. The points are diffusion coefficients obtained from the slope of the mean squared displacement curves, and the lines are 6th order polynomial fits that serve as a guide to the eye. Data at 0.85 g/cm^3 is excluded for fitting due to the possibility of cavitation.

data and the fitted VTF parameters are presented in Appendix 4.A. We can now combine the viscosity and diffusivity data, and compute the ratio $\chi(T)/\chi(T = 350\text{ K})$ along each isochore, where $\chi = D\eta/T$. To obtain smooth curves, $\chi(T)$ is computed by using the analytical VTF fits of both η and D for each density. Any deviation of the ratio $\chi(T)/\chi(T = 350\text{ K})$ away from 1 then indicates a violation of the Stokes-Einstein relation (Figure 4.9). As typical of many liquids, SPC/E water obeys the Stokes-Einstein relation fairly well at high temperatures, but a clear violation occurs as it becomes supercooled.

We can further investigate the breakdown of Stokes-Einstein behavior in water by mapping the (ρ, T) region where Eq. 4.1 is valid. In Figure 4.10, the shaded regions, using two different quantitative measures on $\chi(T)/\chi(T = 350\text{ K})$, correspond to state points where Stokes-Einstein behavior is violated, with the boundary corresponding to the onset of this violation. The red shaded region corresponds to the condition $\chi(T)/\chi(T = 350\text{ K}) \geq 1.1$, while the green shaded region corresponds to $\chi(T)/\chi(T = 350\text{ K}) \geq 1.05$. In a normal fluid, the glass transition temperature increases as the density is increased, which results in a higher onset temperature for Stokes-Einstein violation. Here however, the opposite is true for $0.9 \leq \rho \leq 1.15$ g/cm^3, which indicates another anomaly. This density range is comparable to those where the other properties of water behave anomalously, and suggests a correlation of the Stokes-Einstein onset anomaly to the structural

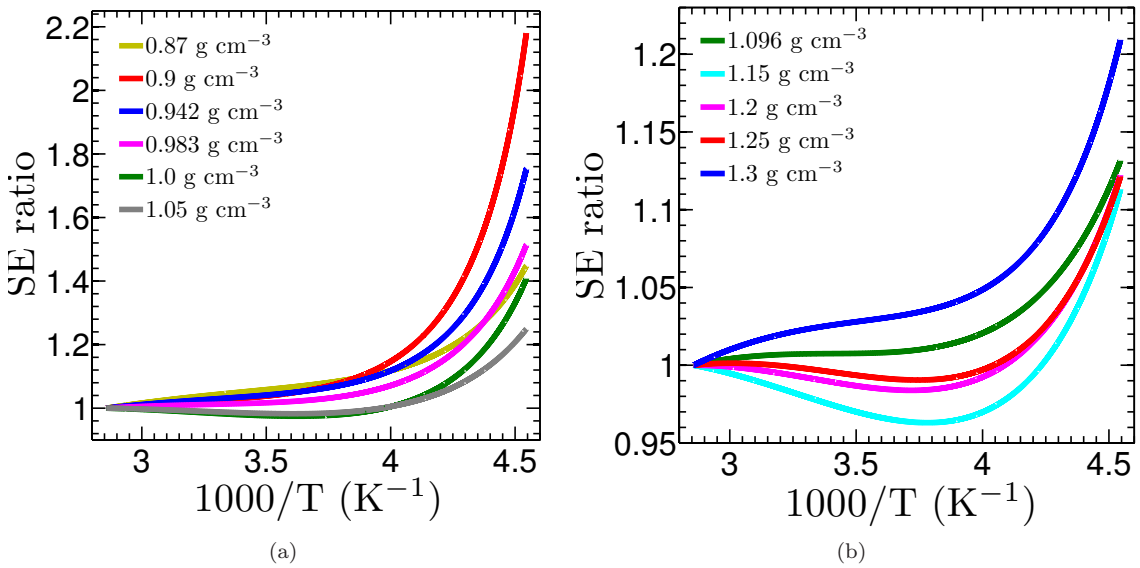

Figure 4.9: The Stokes-Einstein ratio, $D\eta/T$, plotted as a function of inverse temperature for various densities. For each density, the ratio is normalized to its value at 350 K. A horizontal line at 1 would indicate that the Stokes Einstein relation is observed. The smooth curves here are calculated by using the analytic VTF forms for both η and D.

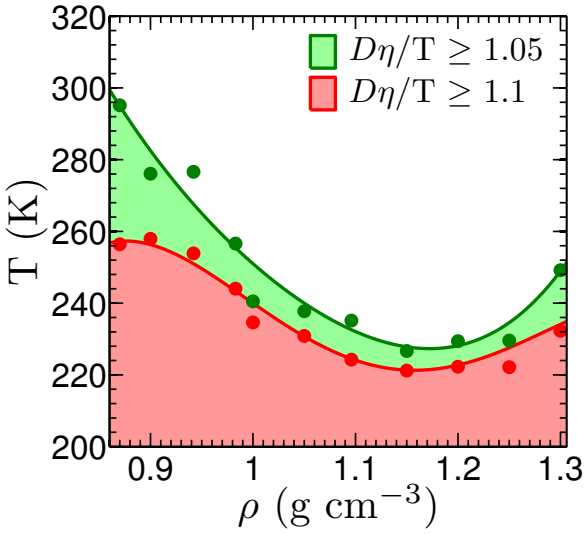

Figure 4.10: The onset of Stokes-Einstein violation by using two objective criteria, when the normalized Stokes-Einstein ratio is 1.05 (green) or 1.1 (red). For a typical liquid, this onset temperature increases with density. Here, we clearly see a range of densities exhibiting the opposite trend, indicating an anomalous property of water.

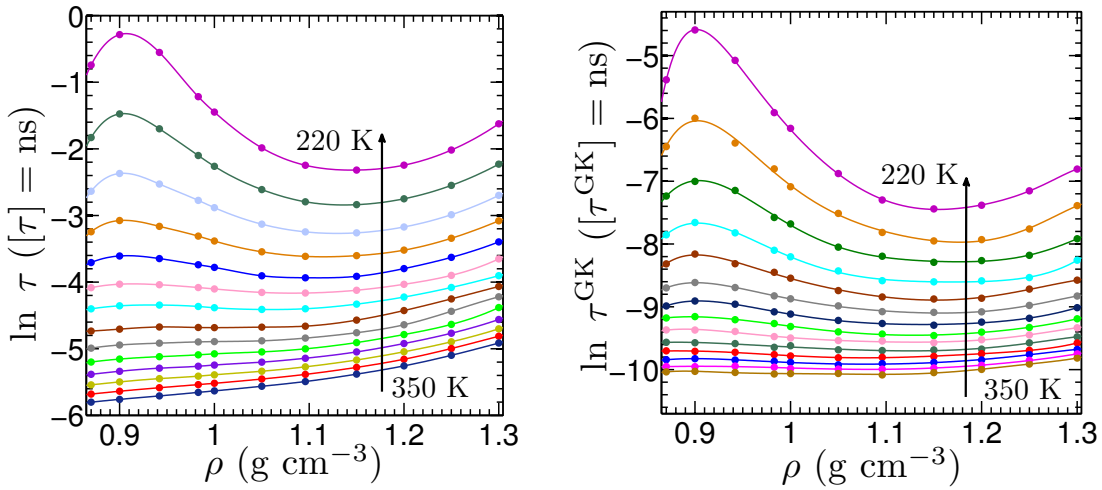

Figure 4.11: The structural (a) and stress (b) relaxation times as a function of density. The increment between adjacent curves is 10 K. The raw data (shown in Appendix 4.A) are fitted to splines and polynomials respectively, which are guides to the eye.

and kinetic anomalies. Stokes-Einstein violation is typically associated with supercooling, where the rapid increase in viscosity becomes decoupled with the rapid decrease in diffusivity. In the density range of the kinetic anomalies, however, compression results in a *decrease* in viscosity and *increase* in diffusivity. Together, this means the temperature of the onset of rapid viscosity and diffusivity changes is then *lowered* upon compression. Consequently, in this region of anomalous kinetic behavior, the onset temperature of Stokes-Einstein violation is also lowered with a density increase.

4.3.3 Relaxation Times

Similar to viscosity and diffusion, we plot the density dependence of relaxation times for various temperatures (Figure 4.11). We again apply VTF fits along each isochore, and the raw data and associated VTF parameters for both the structural and stress relaxation times are also presented in Appendix 4.A. For both types of relaxation times, anomalous behavior is evident by the region of negative slope on these curves, which indicate that the relaxation times *decrease* as the density increases at fixed temperature. Combined with the viscosity (Figure 4.6) and diffusivity (Figure 4.8) data sets, this indicates relaxation processes collectively behave anomalously at low enough temperatures for SPC/E water.

We further investigate the relationship between the structural relaxation time, τ, and the stress relaxation time, τ^{GK}, by plotting their ratio τ/τ^{GK} (Figure 4.12). Here, the curves are obtained

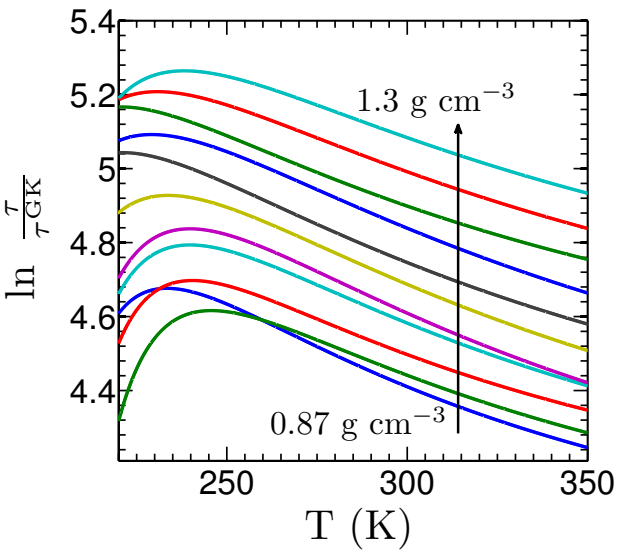

Figure 4.12: The ratio of the structural relaxation time, τ, to the stress relaxation time τ^{GK}. The five lowest densities shown are 0.87, 0.90, 0.942, 0.983, and 1.0 g/cm^3, after which the increment between adjacent curves is 0.05 g/cm^3.

by taking the ratio of the respective analytic VTF forms of τ and τ^{GK} for each density. For a given density, at higher temperatures, $\ln \tau/\tau^{GK}$ appears linear, but this relation breaks down as the temperature is decreased, and a local maximum of the ratio occurs at low temperatures. Additionally, note the crossing of isochores at low enough temperatures. This non-trivial relation directly reflects that τ and τ^{GK} are two distinct relaxation times that are derived and defined differently.

4.3.4 Stokes-Einstein Variants

We further examine the differences between the structural relaxation time, τ, the stress relaxation time, τ^{GK}, and viscosity, η, by comparing the Stokes-Einstein ratios derived from them: $\chi(T)/\chi(T = 350$ K), where $\chi = D\eta/T$, $D\tau$, $D\tau/T$, $D\tau^{GK}$, or $D\tau^{GK}/T$. To obtain smooth curves, we use the analytical VTF forms for η, D, τ, and τ^{GK} when computing these ratios. In Figure 4.13, we plot the temperature dependence of the various Stokes-Einstein ratios at a density of $\rho = 1.0$ g/cm^3. At low enough temperatures, all three variants exhibit a strong violation of the Stokes-Einstein relation. However, only the "true" relation of $D\eta/T$ obeys Stokes-Einstein behavior at higher temperatures. These results are representative of other densities investigated in this work.

Figure 4.13 further illustrates the distinction between the structural relaxation time, τ, and the stress relaxation time, τ^{GK}. The structural relaxation time results from the Gaussian solution to the diffusion equation[53], given by $F_s(k,t) = \exp(-k^2 Dt) \equiv \exp(-t/\tau)$, where $F_s(k,t)$ is the self-intermediate scattering function and k is the associated wave vector. This thus implies $D \propto 1/\tau$,

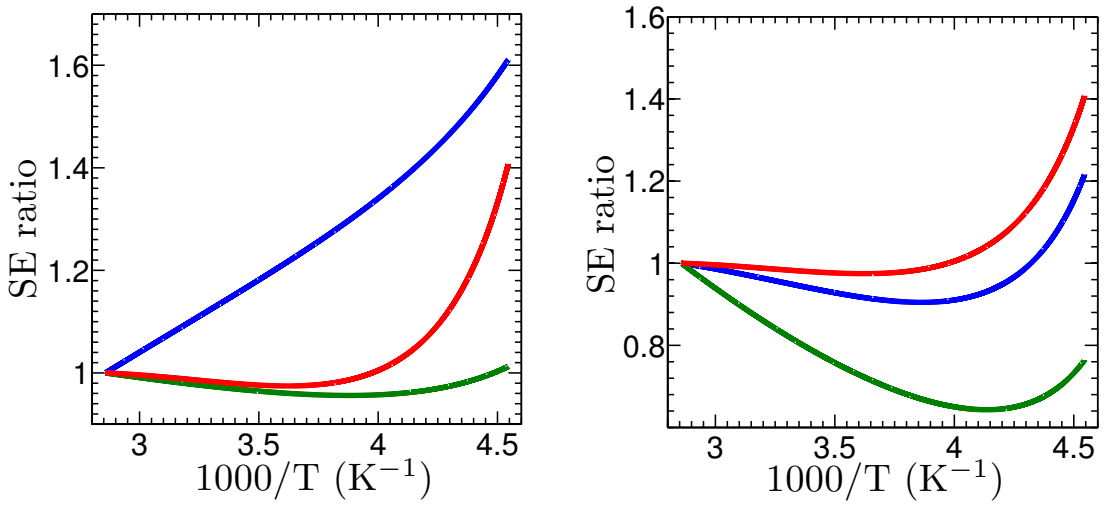

(a) (b)

Figure 4.13: Comparison of different Stokes-Einstein variants. The Stokes-Einstein (SE) ratio is defined and color-coded as follows: $D\eta/T$ (red), $D\tau$ (green), and $D\tau/T$ (blue), all normalized to their respective values at $T = 350$ K. The relaxation time used in (a) is the structural relaxation time, obtained from the self-intermediate scattering function, whereas the one used in (b) is the stress relaxation time, obtained from the Green-Kubo equation.

which then relates to viscosity by $\tau \propto \eta/T$. Indeed, from Figure 4.13a, the Stokes-Einstein ratio of $D\tau$ is a good approximant for $D\eta/T$ at higher temperatures, although at low temperature the Stokes-Einstein violation is not as strong. The ratio $D\tau/T$, however, is not constant over any temperature range, and deviates significantly from $D\eta/T$ for all temperatures.

On the other hand, the proportionality that relates stress relaxation time to viscosity, $\tau^{GK} \propto \eta$, is based on the relation $\eta = G_\infty \tau^{GK}$, where G_∞ is the instantaneous shear modulus and commonly approximated as a constant. Accordingly, from Figure 4.13b, we see that the Stokes-Einstein ratio $D\tau^{GK}/T$ more closely follows $D\eta/T$ than $D\tau^{GK}$ does, with a particularly pronounced low temperature violation. However, because G_∞ does actually have a slight temperature dependence(Figure 4.14), we still observe a slight, but noticeable, deviation of $D\tau^{GK}/T$ from $D\eta/T$.

Collectively, the comparison of these ratios reinforces the findings of Chapter 3[54], namely that the structural relaxation time and the stress relaxation time are not equivalent or interchangeable. Furthermore, when using relaxation times as a substitute for viscosity to study Stokes-Einstein behavior, the relation $\tau \propto \eta/T$ appears to be a reasonable approximation at high temperatures, while $\tau^{GK} \propto \eta$ seems more acceptable at low temperatures. However, over a broad temperature range, neither of these proportionatelies reflect the true Stokes-Einstein behavior. This once again strongly indicates that caution is required when using relaxation time as a substitute for viscosity to study Stokes-Einstein behavior.

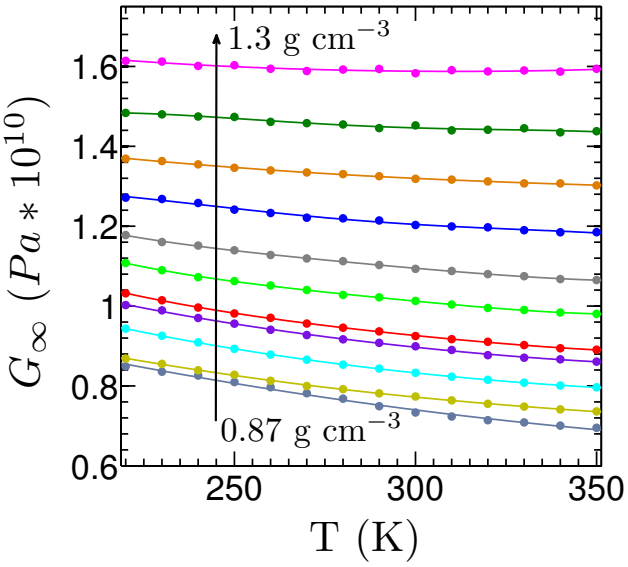

Figure 4.14: The temperature dependence of the instantaneous shear modulus, as defined by Eq. 4.9. The five lowest densities shown are 0.87, 0.90, 0.942, 0.983, and 1.0 g/cm^3, after which the increment between adjacent curves is 0.05 g/cm^3.

4.4 Conclusions

We presented in this chapter, to our knowledge, the first comprehensive analysis of viscosity for SPC/E water over a wide range of thermodynamic conditions. At low enough temperatures, we observe anomalous behavior, where viscosity *decreases* upon compression. When mapped onto the (ρ, T) plane, the region of the viscosity anomaly is comparable to that of diffusivity, and both of these regions are contained within the region of structural anomalies. This suggests that in the anomalous region for viscosity and diffusivity, the mobility increase is caused by pressure-induced distortions of the hydrogen bond network.

We also investigated the Stokes-Einstein behavior for this system. Similar to many liquids, at higher temperatures, SPC/E water is well described by the Stokes-Einstein equation, while at low enough temperatures strong violation is observed. However, the temperature at which violation occurs exhibits anomalous behavior, as for the density range $0.9 \leq \rho \leq 1.15$ g/cm^3, the onset temperature of violation *decreases* upon compression.

We observe anomalous behavior for both the structural and stress relaxation times, which occurs at similar state conditions as the viscosity and diffusivity anomalies. When used as a substitute to study Stokes-Einstein behavior, the relaxation times based upon $\tau \propto \eta/T$ and $\tau^{GK} \propto \eta$ are reasonable approximations for η at high and low temperatures, respectively. However, neither structural or stress relaxation times adequately describe the true Stokes-Einstein behavior over the full

temperature range explored in this investigation. We also find that no trivial proportionality exists between τ and τ^{GK}. These results reinforce those of Chapter 3[54], and further demonstrate that the structural relaxation time and the stress relaxation time are distinct quantities, and are not equivalent or interchangeable.

For our study, we used the SPC/E model of water, one of the many molecular water models currently available for use in computer simulations. While SPC/E shows prominently the structural, kinetic, and thermodynamic anomalies of water, it would be useful to compare the anomalous domains of various water models. When considered together with the results of the earlier study by Errington and Debenedetti[17], the region of anomalous behavior for kinetic processes (viscosity, diffusivity, and relaxation times) is consistently contained within the region of structural anomalies, suggesting that the anomalous increase in mobility upon compression is the result of the distortion of the tetrahedral hydrogen bond structure. Although we can understand the relationship between the structural and kinetic anomalies, the relationship of these anomalies to the corresponding thermodynamic anomaly is a topic of active ongoing investigation[63], and provides a natural direction for future studies.

4.5 Acknowledgments

The financial support of the National Science Foundation is gratefully acknowledged (Grant CHE-1213343 to PGD). Calculations were performed at the Terascale Infrastructure for Groundbreaking Research in Engineering and Science (TIGRESS) at Princeton University.

Appendix 4.A Raw Data and VTF Parameters

This appendix contains the raw data for viscosity (η), diffusivity (D), structural relaxation time (τ), and stress relaxation time (τ^{GK}), for all densities (from 0.85 to 1.3 g/cm^3) and temperatures (from 220 to 350 K) investigated.

Each set of raw data is fit to the VTF equation, and the VTF parameters, A, B, and T_0 are also presented here. The VTF equation is given by

$$\log X = \frac{A}{T - T_0} + B, \tag{4.11}$$

where $X = \eta$, D, τ, or τ^{GK}.

Table 4.1: Viscosity Raw Data ($10^3\,\eta$, in Pa.s)

T (K)	Density (g/cm^3)					
	0.85	0.87	0.9	0.942	0.983	1.0
220	26.2	29.5	88.1	58.9	27.3	21.8
230	8.29	10.0	21.3	15.5	11.0	8.47
240	3.75	4.50	7.63	7.16	4.97	4.60
250	2.11	2.38	3.92	3.58	2.91	2.69
260	1.30	1.47	2.33	2.16	2.01	1.89
270	0.899	0.986	1.45	1.45	1.36	1.34
280	0.720	0.728	1.07	1.10	1.05	1.04
290	0.531	0.587	0.826	0.848	0.860	0.846
300	0.435	0.474	0.660	0.694	0.691	0.695
310	0.366	0.384	0.532	0.566	0.577	0.610
320	0.307	0.331	0.460	0.488	0.506	0.514
330	0.266	0.285	0.405	0.428	0.452	0.460
340	0.236	0.253	0.353	0.385	0.409	0.413
350	0.211	0.230	0.325	0.346	0.365	0.380

T (K)	Density (g/cm^3)					
	1.05	1.096	1.15	1.2	1.25	1.3
220	11.4	7.97	7.72	9.36	10.8	17.3
230	5.96	4.69	4.56	5.38	6.51	9.22
240	3.42	3.18	3.03	3.83	4.16	5.76
250	2.33	2.14	2.19	2.76	3.06	3.89
260	1.68	1.63	1.69	2.08	2.27	2.91
270	1.30	1.28	1.35	1.67	1.87	2.26
280	1.02	1.05	1.12	1.41	1.47	1.88
290	0.847	0.882	0.953	1.20	1.29	1.62
300	0.731	0.783	0.832	1.06	1.11	1.39
310	0.625	0.669	0.728	0.910	0.987	1.24
320	0.546	0.597	0.656	0.843	0.899	1.09
330	0.485	0.538	0.595	0.759	0.830	0.991
340	0.451	0.489	0.561	0.698	0.758	0.935
350	0.419	0.445	0.510	0.652	0.701	0.859

Table 4.2: Diffusivity Raw Data ($10^9\,D$, in m^2/s)

T (K)	Density (g/cm^3)					
	0.85	0.87	0.9	0.942	0.983	1.0
220	0.057	0.047	0.033	0.039	0.076	0.090
230	0.152	0.130	0.095	0.113	0.167	0.198
240	0.316	0.308	0.230	0.250	0.326	0.366
250	0.532	0.562	0.454	0.484	0.564	0.585
260	0.868	0.786	0.749	0.759	0.857	0.895
270	1.25	1.26	1.18	1.17	1.26	1.22
280	1.72	1.75	1.65	1.55	1.70	1.65
290	2.20	2.35	2.22	2.06	2.21	2.17
300	2.88	3.09	2.74	2.80	2.74	2.63
310	3.61	3.71	3.39	3.28	3.11	3.33
320	4.28	4.47	4.25	3.99	3.89	3.86
330	5.34	5.30	5.04	4.65	4.51	4.54
340	6.32	6.42	5.91	5.31	5.21	5.27
350	6.93	6.79	6.51	6.12	6.16	5.93

T (K)	Density (g/cm^3)					
	1.05	1.096	1.15	1.2	1.25	1.3
220	0.154	0.193	0.214	0.193	0.149	0.102
230	0.279	0.346	0.324	0.313	0.247	0.184
240	0.453	0.537	0.497	0.452	0.391	0.309
250	0.727	0.747	0.727	0.670	0.531	0.458
260	0.992	0.957	1.03	0.885	0.754	0.590
270	1.32	1.39	1.28	1.16	0.958	0.791
280	1.65	1.61	1.62	1.36	1.24	1.01
290	2.14	2.12	1.93	1.71	1.50	1.32
300	2.73	2.49	2.31	2.08	1.67	1.52
310	3.08	3.10	2.63	2.35	1.94	1.69
320	3.66	3.47	3.22	2.74	2.46	1.93
330	4.26	4.02	3.39	3.13	2.74	2.19
340	4.85	4.40	3.94	3.58	3.02	2.51
350	5.53	4.90	4.75	3.80	3.24	2.72

Table 4.3: Structural Relaxation Time Raw Data ($10^2\,\tau$, in ns)

T (K)	Density (g/cm^3)					
	0.85	0.87	0.9	0.942	0.983	1.0
220	41.7	47.6	75.2	57.5	29.6	23.5
230	14.6	16.0	22.8	18.3	12.2	10.4
240	6.72	7.16	9.35	7.98	6.24	5.60
250	3.76	3.90	4.62	4.23	3.65	3.39
260	2.36	2.46	2.71	2.61	2.38	2.28
270	1.66	1.69	1.78	1.76	1.69	1.65
280	1.20	1.23	1.28	1.30	1.27	1.25
290	0.864	0.879	0.905	0.934	0.927	0.925
300	0.688	0.680	0.713	0.733	0.747	0.750
310	0.553	0.552	0.577	0.598	0.615	0.624
320	0.454	0.459	0.481	0.503	0.518	0.528
330	0.383	0.392	0.410	0.430	0.447	0.456
340	0.331	0.341	0.356	0.375	0.393	0.401
350	0.293	0.302	0.315	0.332	0.350	0.358

T (K)	Density (g/cm^3)					
	1.05	1.096	1.15	1.2	1.25	1.3
220	13.7	10.6	9.84	10.6	13.3	19.7
230	7.35	6.12	5.86	6.40	7.82	10.8
240	4.37	3.89	3.84	4.19	5.04	6.73
250	2.89	2.69	2.72	2.96	3.54	4.59
260	2.01	1.96	2.00	2.24	2.66	3.35
270	1.57	1.56	1.62	1.77	2.03	2.59
280	1.21	1.23	1.32	1.46	1.69	2.02
290	0.932	0.946	1.04	1.20	1.42	1.72
300	0.759	0.790	0.857	0.965	1.18	1.47
310	0.643	0.673	0.739	0.834	0.971	1.25
320	0.551	0.584	0.643	0.729	0.851	1.05
330	0.481	0.514	0.569	0.644	0.748	0.909
340	0.428	0.459	0.510	0.576	0.676	0.813
350	0.384	0.412	0.460	0.521	0.611	0.734

Table 4.4: Stress Relaxation Time Raw Data ($10^4\,\tau^{GK}$, in ns)

T (K)	Density (g/cm^3)					
	0.85	0.87	0.9	0.942	0.983	1.0
220	42.6	45.8	101	62.4	27.2	21.2
230	13.7	15.8	24.9	16.7	11.1	8.35
240	6.30	7.20	9.09	7.88	5.12	4.62
250	3.59	3.88	4.73	4.01	3.04	2.74
260	2.25	2.45	2.86	2.45	2.14	1.95
270	1.58	1.67	1.82	1.68	1.47	1.40
280	1.29	1.25	1.35	1.29	1.14	1.10
290	0.968	1.03	1.06	1.00	0.946	0.902
300	0.808	0.854	0.853	0.833	0.768	0.751
310	0.690	0.702	0.696	0.687	0.648	0.664
320	0.594	0.612	0.608	0.598	0.577	0.565
330	0.525	0.531	0.540	0.529	0.519	0.510
340	0.471	0.477	0.475	0.480	0.472	0.461
350	0.427	0.438	0.441	0.434	0.424	0.427

T (K)	Density (g/cm^3)					
	1.05	1.096	1.15	1.2	1.25	1.3
220	10.3	6.76	6.07	6.22	7.25	10.7
230	5.46	4.04	3.59	3.60	4.40	5.72
240	3.19	2.76	2.41	2.58	2.82	3.59
250	2.19	1.87	1.76	1.87	2.08	2.43
260	1.60	1.44	1.37	1.42	1.55	1.83
270	1.25	1.14	1.10	1.14	1.28	1.42
280	0.994	0.947	0.914	0.968	1.01	1.18
290	0.829	0.800	0.785	0.825	0.892	1.02
300	0.721	0.716	0.691	0.731	0.767	0.880
310	0.622	0.615	0.607	0.630	0.685	0.781
320	0.549	0.552	0.547	0.585	0.623	0.689
330	0.490	0.500	0.500	0.529	0.574	0.623
340	0.458	0.458	0.473	0.486	0.528	0.589
350	0.427	0.417	0.430	0.456	0.488	0.539

Table 4.5: VFT Fitting Parameters for Shear Viscosity η.

ρ(g/cm^3)	A(K)	T_0(K)	B
0.85	320.3	171.4	-10.24
0.87	340	169.8	-10.28
0.9	301.6	179.3	-9.823
0.942	297.7	176.6	-9.695
0.983	306.6	169.2	-9.616
1.0	297.1	167.7	-9.51
1.05	309.5	157.3	-9.403
1.096	336.6	145.7	-9.358
1.15	287.5	150.9	-9.023
1.2	288.9	149.5	-8.782
1.25	277.4	153.4	-8.68
1.3	246.9	163	-8.382

Table 4.6: VFT Fitting Parameters for Diffusivity D.

ρ(g/cm^3)	A(K)	T_0(K)	B
0.85	-506	150.8	-16.25
0.87	-453.1	158.3	-16.42
0.9	-444.9	162.2	-16.46
0.942	-427	161.6	-16.65
0.983	-475.4	149.7	-16.57
1.0	-513.5	142.8	-16.47
1.05	-549.1	129.4	-16.54
1.096	-549.2	122.6	-16.7
1.15	-554	118.7	-16.83
1.2	-530.3	120.2	-17.06
1.25	-486.9	128.1	-17.33
1.3	-390	144.8	-17.82

Table 4.7: VFT Fitting Parameters for Structural Relaxation Time τ.

ρ(g/cm^3)	A(K)	T_0(K)	B
0.85	459.4	157.1	-8.206
0.87	440	160.3	-8.126
0.9	414.2	166.7	-8.036
0.942	401.3	165.2	-7.88
0.983	452.7	152.8	-7.962
1.0	463.9	148.5	-7.942
1.05	499.9	135.5	-7.902
1.096	523.5	126.3	-7.839
1.15	508.8	124.1	-7.637
1.2	503.1	123.6	-7.479
1.25	470.4	129.5	-7.226
1.3	431.2	138.5	-6.935

Table 4.8: VFT Fitting Parameters for Stress Relaxation Time τ^{GK}.

ρ(g/cm^3)	A(K)	T_0(K)	B
0.85	275.1	175.5	-11.63
0.87	298.4	173.2	-11.74
0.9	278.7	180.9	-11.71
0.942	273.8	178.3	-11.65
0.983	280.7	171.3	-11.65
1.0	272.4	169.7	-11.58
1.05	285.5	159.4	-11.58
1.096	311.4	148	-11.62
1.15	270.9	152.5	-11.42
1.2	277.6	150.6	-11.39
1.25	270.3	154	-11.31
1.3	247.3	162.7	-11.15

Appendix 4.B Error Bars for Viscosity Anomalous Region

The contents of this appendix is based on Appendix C of Victoria Hwang's Princeton University Senior Thesis "Viscosity Anomalies and Violations of the Stokes-Einstein Equation in Molecular Simulations of Water"[64]. Please see Section 1.5 for a discussion of the collaboration on this study.

The densities simulated in this study range from 0.85 to 1.3 g/cm^3. To check for the possibility of cavitation at the lowest densities, we plot the system pressure as a function of density for a temperature of 200 K, which is lower than the temperature range used throughout the rest of the study (from 220 to 350 K). We observe a minimum in pressure around 0.88 g/cm^3. Although, at a fixed density, cavitation can be suppressed by an increase in temperature, the data points taken along the 0.85 and 0.87 g/cm^3 isochores are near the onset of becoming mechanically unstable, and should be treated with precaution.

Because the data points from 0.85 and 0.87 g/cm^3 are near the local viscosity maxima of Figure 4.6, we use three options to fit the data points to find the local maxima: including the data at 0.85 and 0.87 g/cm^3, excluding the 0.85 g/cm^3 data only, and excluding both the 0.85 and 0.87 g/cm^3 data(Figure 4.15). The values of the resulting viscosity maxima vary slightly between the three options, which then results in slight variations in the shape of the dome of anomalies for viscosity.

In Figure 4.15, we also compare the results of the domes obtained from fitting the raw data versus smoothed data (obtained by using the VTF fits). In this case, the overall shape of the domes does not change, but for each dome, the data points obtained from using the smoothed data have much less noise. This confirms the validity of using VTF fits as a method to decrease the scatter of data.

In Figure 4.7, we consolidate the three options to produce the locus of viscosity maxima: each point represents the average value of the three approaches obtained from the smoothed data, and the error bars correspond to the range of values obtained across the three approaches. These error bars directly result from the uncertainty of the mechanical stability of the systems at 0.85 and 0.87 g/cm^3.

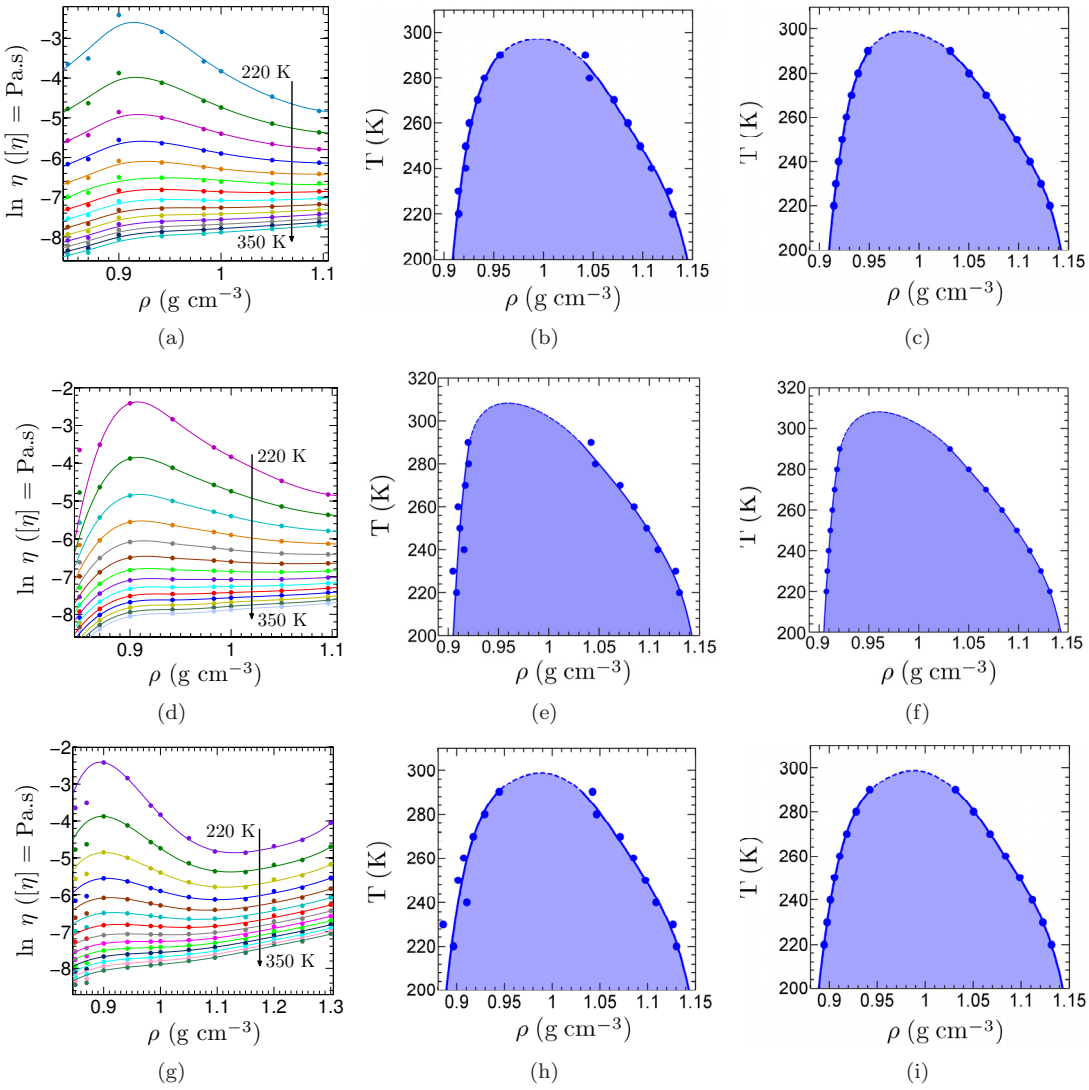

Figure 4.15: Three options for constructing the viscosity dome. Option 1 (a-c): Spline fits through all the data (from 0.85 to 1.3 g/cm^3). Option 2 (d-f): Spline fits excluding the data at 0.85 g/cm^3. Option 3 (g-i): Fifth-order polynomial fits excluding the data at 0.85 and 0.87 g/cm^3. Panels (b,e,h) show the domes found from the raw data, and panels (c,f,i) show the domes from the smoothed data. The blue regions under the domes correspond to the anomalous viscosity behavior. The solid lines are sixth-order (a,g) and eighth-order (d) polynomial fits. The dotted lines represent the estimated shape of the dome at higher temperatures. The points on the left side of the domes correspond to the set of local maxima of the $\eta(T)$ curves, while those on the right correspond to the set of local minima.

Bibliography

[1] P. G. Debenedetti and H. E. Stanley, Physics Today **56**, 40 (2003).

[2] K. E. Bett and J. B. Cappi, Nature **207**, 620 (1965).

[3] T. DeFries and J. Jonas, J. Chem. Phys. **66**, 896 (1977).

[4] J. C. Hindman, J. Chem. Phys. **60**, 4488 (1974).

[5] B. Hess, J. Chem. Phys. **116**, 209 (2002).

[6] T. Chen, B. Smit, and A. T. Bell, J. Chem. Phys. **131**, 246101 (2009).

[7] G. Delgado-Barrio *et al.*, Viscosity of liquid water via equilibrium molecular dynamics simulations, in *Frontiers in Quantum Systems in Chemistry and Physics*, edited by S. Wilson, P. Grout, J. Maruani, G. Delgado-Barrio, and P. Piecuch, , Progress in Theoretical Chemistry and Physics Vol. 18, pp. 351–361, Springer Netherlands, 2008.

[8] P. E. Smith and W. F. van Gunsteren, Chem. Phys. Lett. **215**, 315 (1993).

[9] Y. Mao and Y. Zhang, Chem. Phys. Lett. **542**, 37 (2012).

[10] M. A. González and J. L. F. Abascal, J. Chem. Phys. **132**, 096101 (2010).

[11] J. S. Medina *et al.*, Chem. Phys. **388**, 9 (2011).

[12] Y. Wu, H. L. Tepper, and G. A. Voth, J. Chem. Phys. **124**, 024503 (2006).

[13] U. Balucani, J. P. Brodholt, P. Jedlovszky, and R. Vallauri, Phys. Rev. E **62**, 2971 (2000).

[14] E. J. W. Wensink, A. C. Hoffmann, P. J. van Maaren, and D. van der Spoel, J. Chem. Phys. **119**, 7308 (2003).

[15] N. R. Haria, G. S. Grest, and C. D. Lorenz, J Phys. Chem. C **117**, 6096 (2013).

[16] H. J. C. Berendsen, J. R. Grigera, and T. P. Straatsma, J. Phys. Chem. **91**, 6269 (1987).

[17] J. R. Errington and P. G. Debenedetti, Nature **409**, 318 (2001).

[18] A. Einstein, Annalen der Physik **322**, 549 (1905).

[19] L. M. Milne-Thomson, *Theoretical Hydrodynamics*, 4th ed. ed. (Macmillan Co., 1960), p. 584.

[20] A. Noda, K. Hayamizu, and M. Watanabe, J. Phys. Chem. B **105**, 4603 (2001).

[21] J. Read *et al.*, J. Electrochem. Soc. **150**, A1351 (2003).

[22] C. Comminges, R. Barhdadi, M. Laurent, and M. Troupel, J. Chem. Eng. Data **51**, 680 (2006).

[23] D. P. Dobson, J. P. Brodholt, L. Vočadlo, and W. A. Crichton, Mol. Phys. **99**, 773 (2001).

[24] E. D. Snijder, M. J. M. te Riele, G. F. Versteeg, and W. P. M. van Swaaij, J. Chem. Eng. Data **38**, 475 (1993).

[25] S. F. Swallen, P. A. Bonvallet, R. J. McMahon, and M. D. Ediger, Phys. Rev. Lett. **90**, 015901 (2003).

[26] M. K. Mapes, S. F. Swallen, and M. D. Ediger, J. Phys. Chem. B **110**, 507 (2006).

[27] F. Mallamace *et al.*, J. Chem. Phys. **124**, 161102 (2006).

[28] R. Kind *et al.*, Phys. Rev. B **45**, 7697 (1992).

[29] K. L. Ngai, J. H. Magill, and D. J. Plazek, J. Chem. Phys. **112**, 1887 (2000).

[30] I. Chang *et al.*, J. Non-Cryst. Solids **172-174**, 248 (1994).

[31] T. G. Lombardo, P. G. Debenedetti, and F. H. Stillinger, J. Chem. Phys. **125**, 174507 (2006).

[32] G. Tarjus and D. Kivelson, J. Chem. Phys. **103**, 3071 (1995).

[33] F. Blackburn, M. T. Cicerone, G. Hietpas, P. A. Wagner, and M. Ediger, J. Non-Cryst. Solids **174**, 256 (1994).

[34] C. Rønne *et al.*, J. Chem. Phys. **107**, 5319 (1997).

[35] S. K. Kumar, G. Szamel, and J. F. Douglas, J. Chem. Phys. **124**, 214501 (2006).

[36] J. A. Hodgdon and F. H. Stillinger, Phys. Rev. E **48**, 207 (1993).

[37] M. D. Ediger, Annu. Rev. Phys. Chem **51**, 99 (2000).

[38] V. Lubchenko and P. G. Wolynes, Annu. Rev. Phys. Chem. **58**, 235 (2007).

[39] F. H. Stillinger, Science **267**, 1935 (1995).

[40] R. Zwanzig and A. K. Harrison, J. Chem. Phys. **83**, 5861 (1985).

[41] L. Berthier, D. Chandler, and J. P. Garrahan, Europhys. Lett. **69**, 320 (2005).

[42] K. L. Ngai, J. Phys. Chem. B **103**, 10684 (1999).

[43] G. Diezemann, H. Sillescu, G. Hinze, and R. Böhmer, Phys. Rev. E **57**, 4398 (1998).

[44] F. H. Stillinger and J. A. Hodgdon, Phys. Rev. E **50**, 2064 (1994).

[45] M. G. Mazza, N. Giovambattista, H. E. Stanley, and F. W. Starr, Phys. Rev. E **76**, 031203 (2007).

[46] S.-H. Chen *et al.*, Proc. Natl. Acad. Sci. U.S.A **103**, 12974 (2006).

[47] P. Kumar *et al.*, Proc. Natl. Acad. Sci. U.S.A **104**, 9575 (2007).

[48] L. Xu *et al.*, Nat. Phys. **5**, 565 (2009).

[49] D. Jeong, M. Y. Choi, H. J. Kim, and Y. Jung, Phys. Chem. Chem. Phys. **12**, 2001 (2010).

[50] S. H. Lee and T. Chang, Bull. Korean Chem. Soc. **24**, 1590 (2003).

[51] Y. Jung, J. P. Garrahan, and D. Chandler, Phys. Rev. E **69**, 061205 (2004).

[52] R. Yamamoto and A. Onuki, Phys. Rev. Lett. **81**, 4915 (1998).

[53] J. P. Hansen and I. R. McDonald, *Theory of Simple Liquids*, 2nd ed. ed. (Academic Press, 1986), chap. 8.

[54] Z. Shi, P. G. Debenedetti, and F. H. Stillinger, J. Chem. Phys. **138**, 12A526 (2013).

[55] S. Plimpton, J. Comp. Phys. **117**, 1 (1995).

[56] W. G. Hoover, Phys. Rev. A **31**, 1695 (1985).

[57] P. J. Daivis and D. J. Evans, J. Chem. Phys. **100**, 541 (1994).

[58] D. N. Theodorou, T. D. Boone, L. R. Dodd, and K. F. Mansfield, Makromol. Chem., Theory Simul. **2**, 191 (1993).

[59] A. P. Thompson, S. J. Plimpton, and W. Mattson, J. Chem. Phys. **131**, 154107 (2009).

[60] D. Nevins and F. J. Spera, Mol. Simulat. **33**, 1261 (2007).

[61] E. W. Lemmon, M. O. McLinden, and D. G. Friend, Thermophysical properties of fluid systems, in *NIST Chemistry WebBook, NIST Standard Reference Database Number 69*, edited by P. J. Linstrom and W. G. Mallard, National Institute of Standards and Technology, Gaithersburg MD, 20899, 2013.

[62] J. C. Dyre and W. H. Wang, J. Chem. Phys. **136**, 224108 (2012).

[63] J. R. Errington, P. G. Debenedetti, and S. Torquato, Phys. Rev. Lett. **89**, 215503 (2002).

[64] V. Hwang, Senior thesis: Viscosity anomalies and violations of the stokes-einstein equation in molecular simulations of water, 2013.

Chapter 5

Properties of Model Atomic Free-Standing Thin Films

5.1 Introduction

The effect of interfaces on the structure, dynamics and thermodynamics of materials, including supercooled liquids and glasses, is a subject of considerable technical and scientific interest[1]. Important applications of glassy materials, such as organic electronics[2], nanolithography[3], corrosion prevention[4], gas separation[5], and novel nanocomposites[6–8] involve geometries such as supported, free-standing, or confined films, and filler-bulk interfaces, with characteristic dimensions in the 1-100 nm scale. The rational design of these materials and devices requires knowledge of properties such as glass transition temperature[9, 10], physical aging[11], and gas permeation[12], and their underlying basis in the microscopic structure and dynamics of the spatially heterogeneous nanoconfined material.

Numerous studies have probed experimentally the interfacial and confinement-induced properties of glass-forming systems (e.g., refs. 9, 13–23). This remains a very active area of investigation[24], in part because of the interest generated by unresolved differences between the various measurements (e.g., refs. 25–28). A noteworthy recent development is the discovery by Ediger and coworkers that glass films with exceptional kinetic and thermodynamic stability can be formed by vapor deposition[29–35]. Enhanced mobility at the free surface has been invoked as a key mechanism in the formation of such stable glasses[29]. Following Ediger and coworkers' discovery, stable thin film glasses of toluene and ethylbenzene have also been formed by vapor deposition[36–38].

From a theoretical perspective[39], the presence of interfaces, hence of imposed spatial heterogeneity, renders one of the major problems in contemporary condensed matter physics, namely the glass transition, even richer and more challenging. Although some computational studies have addressed the effects of confinement and interfaces on the structure, dynamics and thermodynamics of non-polymeric systems[40–45], the majority of investigations to date have focused on confined polymers (e.g., refs. 46–58). Recently, a schematic facilitated kinetic Ising model representing a thin film, its substrate, and a vapor phase, was shown to reproduce key experimentally-observed characteristics of vapor-deposited glasses, including surface-enhanced relaxation kinetics, and the existence of an optimum substrate temperature for stable glass formation[59].

Motivated by the problem's inherent scientific interest, by the variety of intriguing experimental observations, and in particular the recent findings of Ediger and coworkers on stable glass formation, and by the interesting theoretical predictions on the nature of the glassy surface[39], we have undertaken a systematic computational investigation of the effects of interfaces and geometric confinement on the structure, dynamics and thermodynamics of glass-forming systems. In this chapter we report our results on the simplest system, a free-standing thin film of an atomic glass-forming mixture[60]. In Section 5.2 we describe our system and the numerical techniques employed in this investigation. Results on the film's structure, layer-by-layer dynamics, and energetics, including, importantly, an analysis of minimum-energy configurations (inherent structures)[61–64], are presented in Section 5.3. The major conclusions as well as suggestions for future work are the subject of the concluding Section 5.4.

5.2 Methods

We study the well-known binary Lennard-Jones glass-forming mixture as parameterized by Kob and Andersen[60], namely, a mixture of 80% A particles and 20% B particles, with parameters $\epsilon_{AA} = 1.0$, $\epsilon_{BB} = 0.5$, $\epsilon_{AB} = 1.5$, $\sigma_{AA} = 1.0$, $\sigma_{BB} = 0.88$, and $\sigma_{AB} = 0.8$. Both types of particles have the same mass, m, and interact via a Lennard-Jones potential $U_{\alpha\beta}(r) = 4\epsilon_{\alpha\beta}[(\sigma_{\alpha\beta}/r)^{12} - (\sigma_{\alpha\beta}/r)^{6}]$. Thoughout this chapter, all quantities are expressed in reduced units: length in units of σ_{AA}, temperature in units of ϵ_{AA}/k_B, where k_B is Boltzmann's constant, and time in units of $(\sigma_{AA}m/\epsilon_{AA})^{1/2}$.

In order to ensure continuity of the potential and its first two derivatives at the potential cutoff (continuity needed for energy minimization calculations), we apply a shifted force correction whereby

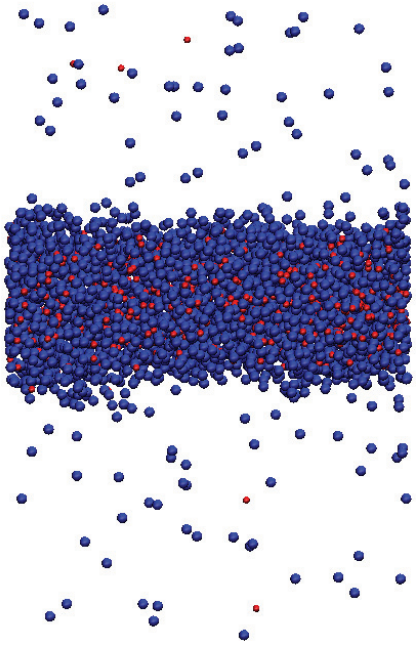

Figure 5.1: Snapshot of 4050 atoms in a $22.4 \times 22.4 \times 35.8$ simulation box at $T = 0.7$. The simulation box is stretched in the z direction so that the resulting film does not self-interact. A particles are shown in blue, and B particles in red.

the force between any two particles, $F_s(r)$ is given by:

$$F_s(r) = \begin{cases} F(r) & r < r_1 \\ F(r) + S(r) & r_1 \leq r < r_c. \\ 0 & r_c \leq r \end{cases} \tag{5.1}$$

Here, $F(r) = -\partial U_{\alpha\beta}(r)/\partial r$ is the unshifted force, and $S(r)$ is a third order polynomial that is switched on between r_1 and r_c, subject to the constraints $S(r_1) = 0$, $S'(r_1) = 0$, $S(r_c) = -F(r_c)$, $S'(r_c) = -F'(r_c)$. Thus, $F_s(r)$ and its first derivative are smooth and continuous everywhere, and vanish at and beyond r_c. For this study, we set $r_1 = 2.0\sigma_{\alpha\beta}$ and $r_c = 2.5\sigma_{\alpha\beta}$ for all interactions.

To simulate a film, we use a computational cell with periodic boundary conditions that is stretched in the z direction. The dimensions of the box are $L_x = L_y = 22.407, L_z = 35.8512$. We initialize the system by placing $N = 4050$ atoms in an fcc lattice of density 1.2 spanning the xy plane, and centered in the z direction. The identity of a particle is selected at random, while maintaining the overall $4:1$ ratio of A to B particles. The simulation length along the z-axis is chosen to be large enough such that the film does not interact with its periodic images in the z

direction (Figure 5.1). The velocity Verlet algorithm of numerical integration is applied, and the molecular dynamics time step used is 0.002. The film is allowed to equilibrate for 2×10^5 time steps, and a coordinate snapshot is taken every 5000 time steps thereafter. The entire simulation is run at fixed particle number, total volume, and temperature (N, V, T), with a Nosé-Hoover thermostat[65]. Our results indicate that some properties of the free standing film, such as the interior density at equilibrium, do not depend strongly on the initialization density, and depend only on the temperature T. The maximum temperature that we can simulate before a significant portion of the particles evaporate from the film is $T = 0.9$. In addition, for any given temperature, there exists a minimum thickness, below which the system fails to form a film (Figure 5.2). We note that the fit line in Figure 5.2 is only a guide to help choose initialization parameters. The precise conditions under which a film is allowed to form is beyond the scope of this paper (the reader is directed to ref. 66 for a comprehensive study on this topic). Here, we simply choose initialization parameters well inside the existence region to ensure that the film maintains its integrity throughout the simulation.

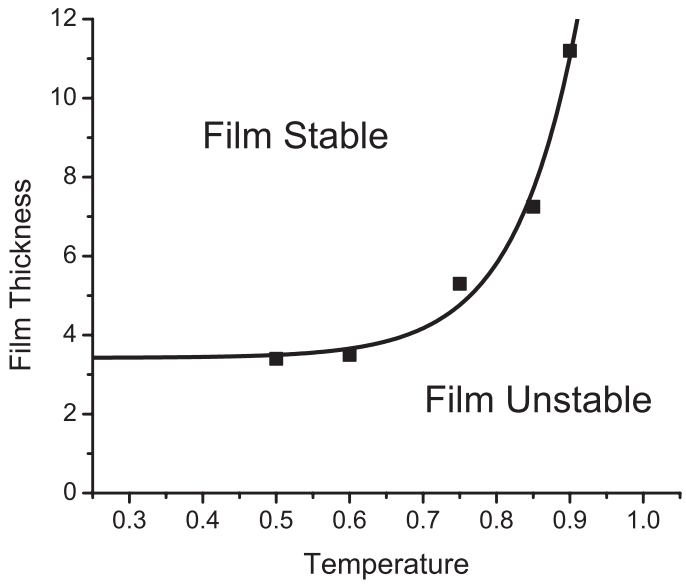

Figure 5.2: Temperature and thickness ranges for stable and unstable film formations. The line is a guide to the eye

Naturally, some of the atoms will leave the film and form a vapor phase in the course of the simulation. As a convenient criterion for differentiating the vapor and liquid phases, we say that an atom i belongs to the film if $u_i < -1$, where $u_i = \frac{1}{2}\Sigma_j U_{\alpha\beta}(r_{ij})$ is the potential energy attributed to an atom, i.e., for every pair interaction between two atoms, half of the potential energy is assigned to one atom and half to the other. We note that this $u_i < -1$ "in film" definition is simply a convenient criterion to identify particles in the film. Indeed, no visually obvious vapor particles have

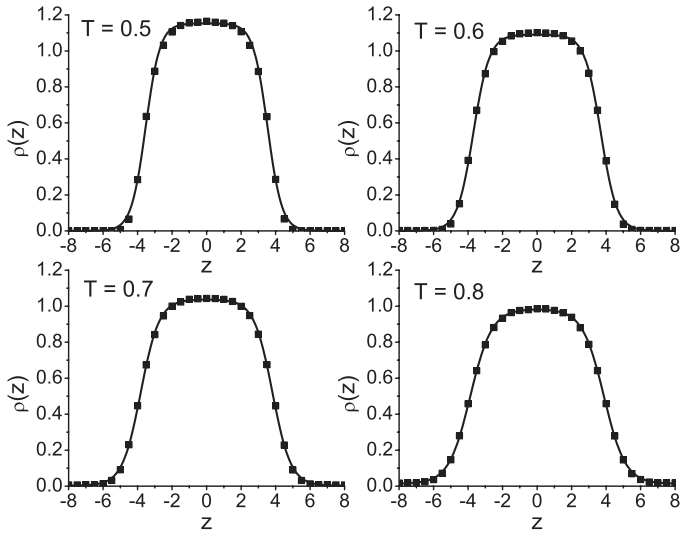

Figure 5.3: Density profiles (both species included) for films of 4050 atoms equilibrated at various temperatures. The hyperbolic tangent fit lines give four defining properties of the density profile: the liquid density ρ_L, the vapor density ρ_V, the location of the center of the interface z_e, and the width of the interface d. The values of ρ_L and d are given in Table 5.1, as a function of temperature.

been observed to obey the "in film" criterion. Since the atoms of the film are only a subset of the total atoms in the simulation box, the center of mass of the film is allowed to shift in the z direction. The magnitude of this shift is on the order of σ_{AA}, and this shift must be subtracted during analysis so that the location of the $z = 0$ plane coincides with the film's center of mass.

Finally, we apply the Fletcher and Reeves[67] method of conjugate gradients to perform energy minimization on each coordinate snapshot to study the underlying inherent structures embedded in the film's multidimensional energy landscape. The particles in the system are moved iteratively along the gradient of the potential energy landscape until $U(\mathbf{r}^N)$, the potential energy as a function of the system's $3N$ translational degrees of freedom, is at a local minimum. The criterion for convergence is satisfied when successive iterations reduce the energy per particle by less than 10^{-7}.

5.3 Results and Discussion

5.3.1 Film Profile

After equilibration, the interior density of a film is dependent only on temperature, and not on the initial density. This is due to the nature of a free-standing film, which is free to expand and contract in the normal direction. The density profile at a given temperature is calculated by partitioning the film into slices of thickness $0.5\sigma_{AA}$ from the center of the film, and then dividing the average number of particles in each slice by the volume of the given slice (Figure 5.3). We perform the following

T	0.5	0.6	0.7	0.8
ρ_L	1.15	1.09	1.04	0.98
d	0.82	0.94	1.07	1.25

Table 5.1: Fitted values of the interior density, ρ_L, and interface thickness, d, for free-standing films of various temperatures, T.

hyperbolic tangent fit[68] to the interfaces of the film:

$$\rho(z) = \frac{1}{2}\left(\rho_L + \rho_V\right) - \frac{1}{2}\left(\rho_L - \rho_V\right)\tanh\left(\frac{2(|z| - z_e)}{d}\right), \tag{5.2}$$

where ρ_L is the interior density of the liquid phase, ρ_V is the density of the vapor phase, z_e is the location where the density is the average of ρ_V and ρ_L, and d is a measure of the thickness of the interface. Thus, the fitting parameters give, in principle, important properties of the film. However, the fitted vapor density is invariably vanishingly small, and z_e depends on the number of particles used in the simulation. Accordingly, in Table 5.1 we report the values of the two physically-relevant, temperature-dependent fitting parameters, ρ_L and d. As shown, with decreasing T, the interior density increases while the thickness of the interface decreases. This is consistent with the simulation results of a pure component Lennard-Jones film as described by Rowlinson and Widom[68].

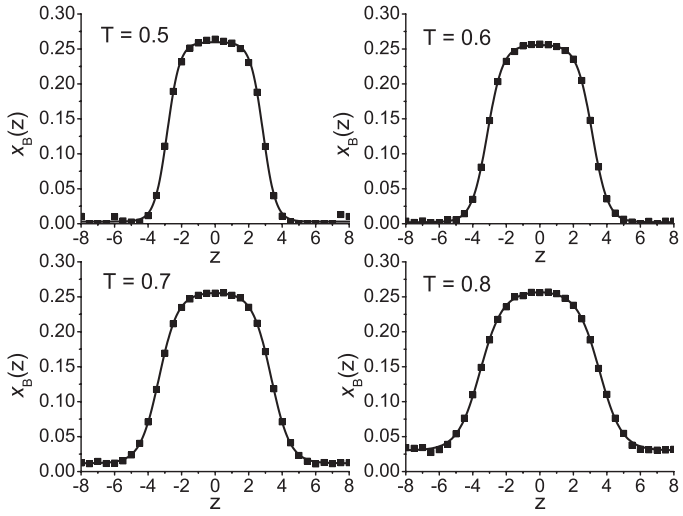

Figure 5.4: Mole fraction of B atoms as a function of film depth z for films at various temperatures. A hyperbolic tangent fit line similar to the form given by Eq. 5.2 is also shown. Species segregation is evident, with a higher concentration of B atoms in the interior of the film.

Another important property is the distribution of the A and B particles as a function of film depth (Figure 5.4). B atoms tend to concentrate towards the center of the film. Since A-A interactions are not as energetically favorable as A-B interactions, the surface is enriched in A atoms. In this way, the system minimizes the energetic cost of forming an interface, namely the loss of half the nearest-

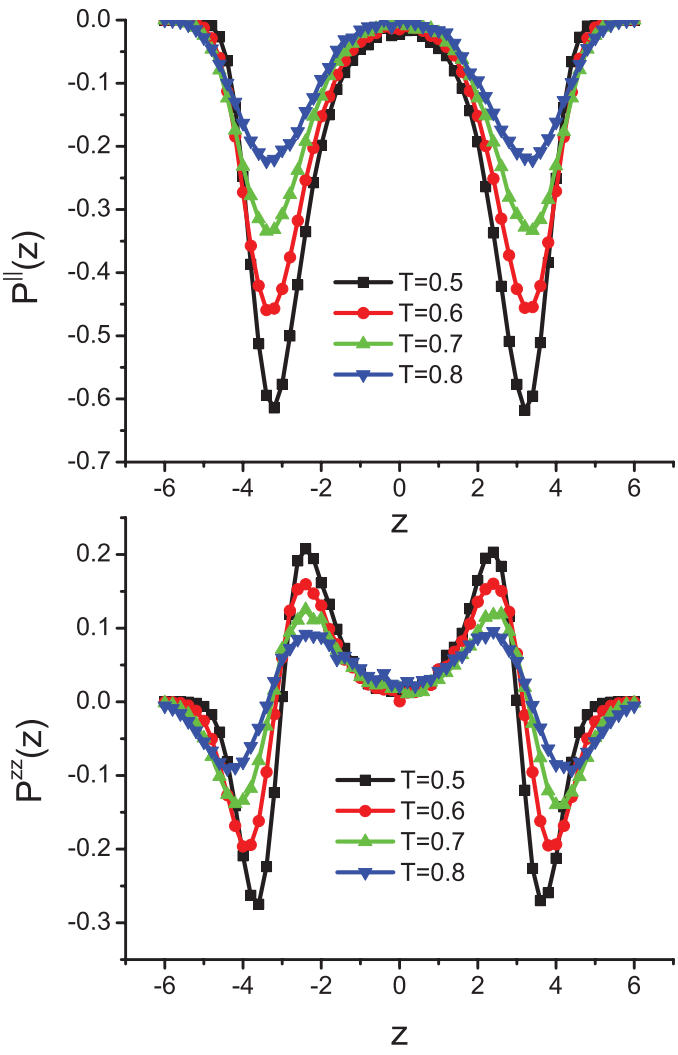

Figure 5.5: The lateral (top) and normal (bottom) stress profiles plotted as a function of film depth z for films of various temperatures. Here, positive values correspond to compression, and negative values to tension.

neighbor interactions for each surface atom. The corresponding segregation of B atoms towards the center preserves the energetically favored A-B interactions. As a consequence, the vapor phase is dominated by A atoms.

5.3.2 Stress

Due to the film's inhomogeneous geometry, the stress varies along the z direction. We consider the pressure normal and parallel to the xy plane, $P^{\perp} = P_{zz}$ and $P^{\parallel} = (P_{xx} + P_{yy})/2$, respectively, and use the virial expression[69] to compute the three diagonal components of the stress tensor in slices of thickness $\Delta z = 0.5\sigma_{AA}$. Figure 5.5 shows the lateral and normal stress profiles for various simulated temperatures. The lateral stress near the center of the film is small, but appreciable

tensile lateral stresses develop in a sub-surface region of thickness $\sim 4\sigma_{AA}$, beginning at a depth of $\sim\sigma_{AA}$ beneath the film's surface. The film's subsurface region is also under tensile normal stress, but appreciable normal compression develops in a region of thickness $\sim 2\sigma_{AA}$ located approximately σ_{AA} away from the center. It can also be seen that the film's center is under slight normal compression, and that the magnitude of all stresses increases upon lowering the temperature. This indicates that the predominant contribution to the film's mechanical properties is configurational.

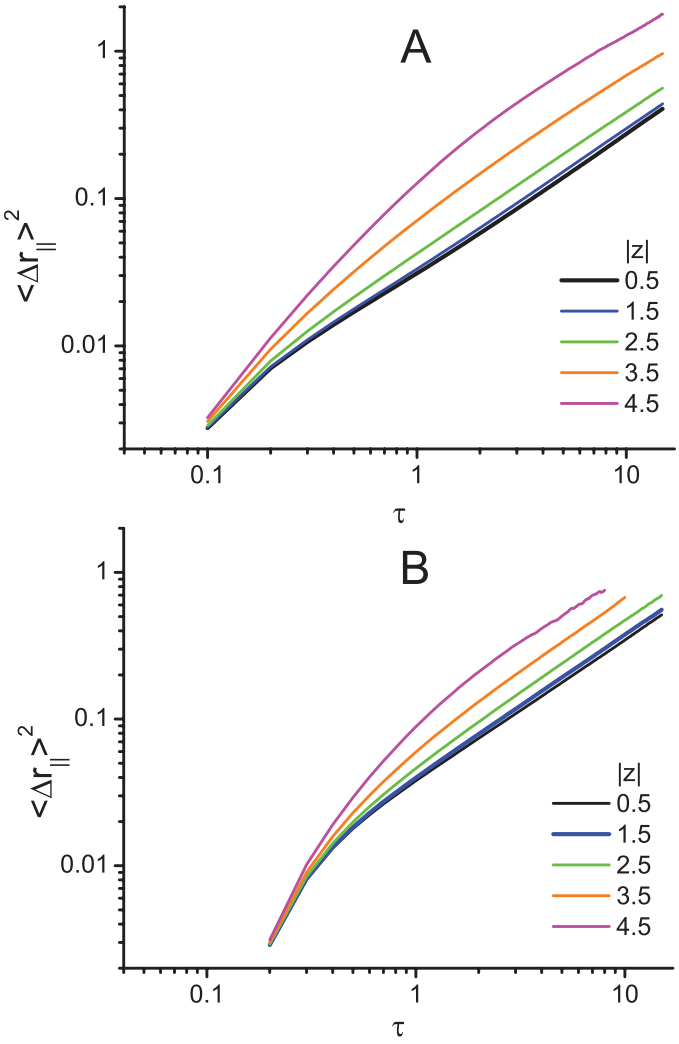

Figure 5.6: The lateral mean squared displacement for A (top) and B (bottom) particles, plotted for various layers in a film of 4050 atoms equilibrated at $T = 0.7$.

5.3.3 Diffusion

Because of the film geometry, particle motion is anisotropic and must be analyzed in the normal and lateral directions. In this study, we are primarily concerned with the lateral diffusion rate. The

trajectory of the system was recorded for 5×10^6 time steps, with new time origins t_0 chosen every 500 time steps, to provide independent "experiments" over which to average. To calculate the lateral diffusion coefficient, we partition the film into slices of thickness σ_{AA} starting from the center of the film, and use the following modified Einstein diffusion equation:

$$D_{||} = \frac{1}{4} \lim_{\tau \to \infty} \frac{d}{d\tau} \left\langle \Delta r_{||}(\tau)^2 \right\rangle_{slice}, \tag{5.3}$$

where $D_{||}$ is the lateral diffusion coefficient, and $\left\langle \Delta r_{||}(\tau)^2 \right\rangle_{slice}$ is the average mean squared displacement of the particles that remain in the slice for the entire interval duration τ. For slices that are contained in the interior of the film, the diffusion coefficient is determined by calculating the slope of $\left\langle \Delta r_{||}(\tau)^2 \right\rangle$ on the interval $\tau \in [2, 12]$. For slices at the interface, $\left\langle \Delta r_{||}(\tau)^2 \right\rangle$ does not become clearly linear until $\tau > 6$, and the slope is calculated on the interval $\tau \in [7, 12]$.

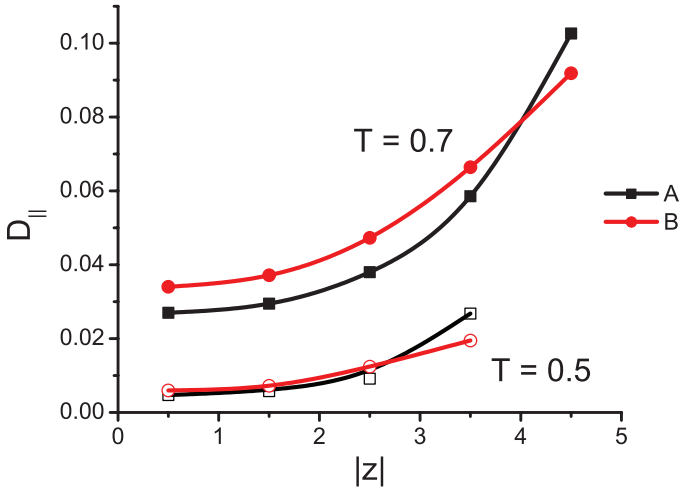

Figure 5.7: Lateral diffusion coefficients for films of 4050 atoms equilibrated at $T = 0.5$ and $T = 0.7$. The diffusion rate at the surface is roughly three times that of the interior.

Figure 5.6 shows the layer-by-layer lateral diffusion of both type A and type B particles for a film at temperature $T = 0.7$. We see that the lateral diffusion coefficient at the surface is roughly three times greater than at the center of the film (Figure 5.7). Further insight can be gained by considering a related quantity, the velocity autocorrelation function (Figure 5.8). A striking difference between the dynamics of the atoms at the surface as compared to the interior is evident. In the interior, after a short time, the atoms on average "rebound" in the opposite direction. Atoms at the surface, on the other hand, on average do not experience this "rebound". As a check of consistency, we also find that both the diffusion coefficient and the velocity autocorrelation function at the center of the film match essentially exactly the corresponding quantities computed for a bulk system with the interior

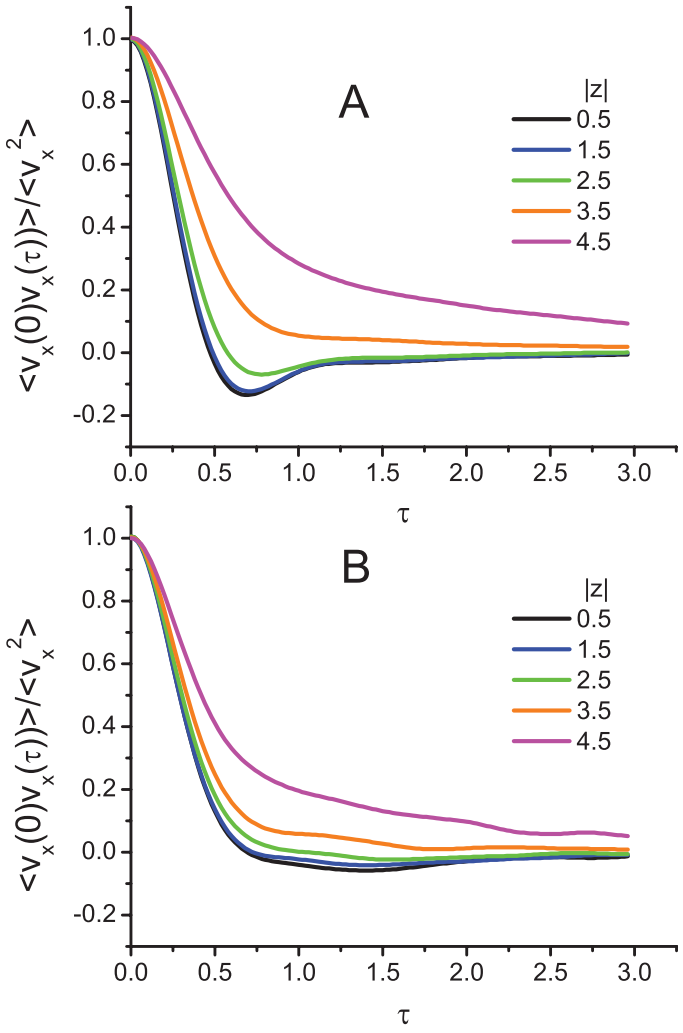

Figure 5.8: Normalized velocity auto-correlation function (VACF) for A (top) and B (bottom) particles plotted for various layers in a film of 4050 atoms equilibrated at $T = 0.7$. For both types of particles, the motion near the surface differs from that in the interior of the film. In the interior, the VACF clearly becomes negative, indicating that the atoms on average "rebound" in the opposite direction after a short time. However, at the surface, the VACF decays monotonically to zero, indicating that, on average, the atoms on the surface do not experience this "rebound". This behavior is qualitatively the same at all other temperatures examined.

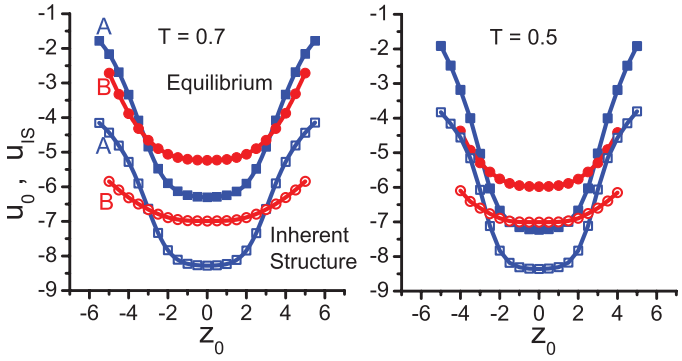

Figure 5.9: Average atomic equilibrium and inherent structure potential energy assigned to an atom, as a function of the initial position before minimization, z_0, for atoms of type A and type B. The potential energy assigned to an atom is calculated by splitting pair interaction energies equally between both participating particles.

film density and composition as parameters.

5.3.4 Inherent Structures

We perform an energy minimization[67] on each coordinate snapshot to study the underlying inherent structures (potential energy landscape)[61] of these films. Here, we will denote by z_0 the z coordinate of a particle before minimization. Figure 5.9 shows the average energy per particle before minimization, u_0, and the corresponding inherent structure quantity, u_{IS}, both plotted against z_0. We also plot the difference $u_{IS} - u_0$ as a function of z_0 (Figure 5.10). At the film interface, the quantity $|u_{IS} - u_0|$ is much larger than in the interior. In other words, on average, the particles at the surface of the film descend more deeply down their portion of the energy landscape than particles in the film's interior. This is in agreement with theoretical predictions[39], and with the interpreta-

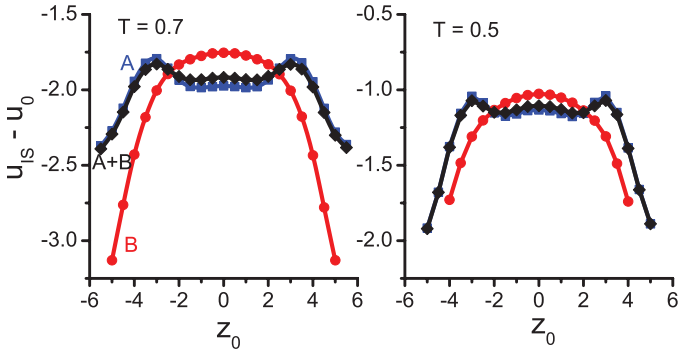

Figure 5.10: Average difference of the energy of an atom with respect to its corresponding inherent structure energy, as a function of the initial position before minimization, z_0, for atoms of type A and B. It can be seen that atoms initially at the surface descend deeper down their portion of the energy landscape upon energy minimization.

tion of the molecular mechanisms underlying the enhanced stability of slow-grown vapor-deposited glasses[29, 30]. It suggests that particles at the surface are able to explore the energy landscape more efficiently, and points to the pronounced basin anharmonicity introduced by the presence of free surfaces; if the system were harmonic, $u_0 - u_{IS}$ would equal $\frac{3}{2}k_BT$, independent of z.

The difference $|u_{IS} - u_0|$ is also a measure of how far energetically an atom is from its underlying single-particle inherent structure energy. This can be interpreted as a measure of stability, i.e., a region of lower $|u_{IS} - u_0|$ is more stable, in the sense that its energy differs by a comparatively smaller amount from that corresponding to the mechanically stable state (inherent structure). We see that as we move away from the center, $|u_{IS} - u_0|$ does not increase monotonically, and the region slightly under the interface, where the absolute difference attains a minimum, is then the most energetically stable region of the film. This non-monotonic behavior is observed at all temperatures examined.

We also plot the average displacement of atoms upon descending down the energy landscape towards the closest local minimum. Figure 5.11 shows the average lateral and normal displacement as a function of z_0. In both directions, the average physical distance to the inherent structure minimum increases as we move outward from the center of the film. This result, combined with the increased diffusion rate at the surface, shows the more efficient landscape sampling at the free surface.

5.4 Conclusions

In this chapter we have investigated the properties of an atomic free-standing film. The 80%(A)-20%(B) binary Lennard-Jones glass-forming mixture considered here exhibits substantial compositional inhomogeneity, with weaker A-A interactions favored at the free surface and stronger A-B contacts favored inside the film. This preferential enrichment of surface and "bulk" in A and B, respectively, reflects primarily the energetics of free surface stabilization. Over the range of temperatures explored herein, we observe a substantial enhancement of lateral mobility at the surface with respect to the film's interior. In agreement with theoretical predictions[39], particles residing at the free surface are able to descend deeper down the energy landscape than particles in the film's interior. Since the difference between equilibrium and inherent structure energy should be independent of position for a harmonic system, this behavior is an indication of the strong basin anharmonicity introduced by the free surfaces.

Our observations suggest several avenues for future inquiry. The possible relevance of our two key observations (enhanced diffusion at the surface, deeper descent down the energy landscape for

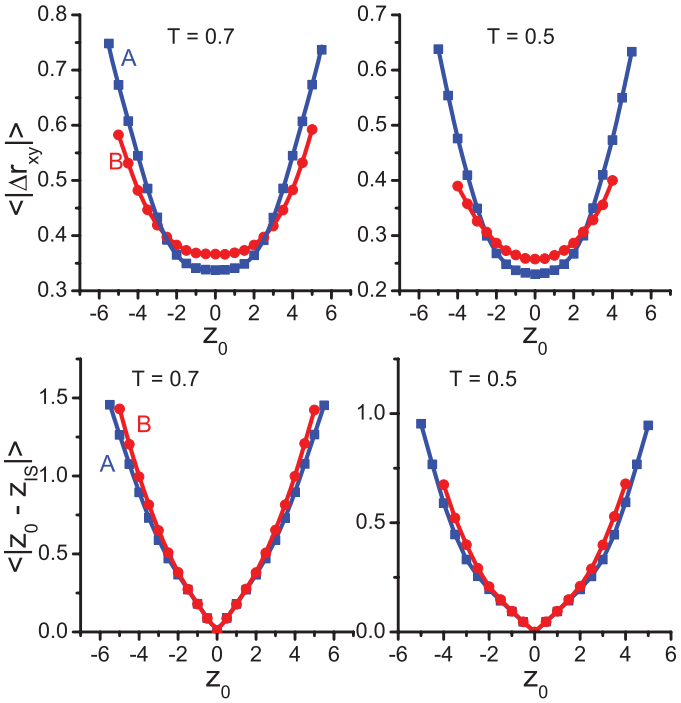

Figure 5.11: The average lateral and normal displacement that an atom undergoes during energy minimization as a function of its initial position z_0. It can be seen that atoms near the surface suffer larger lateral and normal displacements upon energy minimization than their counterparts located in the film's interior.

surface particles) to the recent discovery by Ediger and coworkers of stable glasses formed by slow vapor deposition[29–35] remains to be established. In light of recent reports of surface anisotropy in vapor-deposited stable glasses[70], simulation of model molecular systems that are capable in principle of adopting different orientations at the surface and in the bulk would be informative. The substrate temperature was shown by Ediger *et al.*[30] to be an important variable for controlling the stability of vapor-deposited glasses. The corresponding computational studies remain to be done. Also of interest would be an investigation of the relative importance of surface mobility and anharmonicity in causing surface particles to descend deeper down the energy landscape. Finally, we have described surface particles as being able to sample the energy landscape more efficiently, and providing a general quantitative definition of this idea would be useful.

5.5 Acknowledgments

PGD gratefully acknowledges the support of the Princeton Center for Complex Materials (National Science Foundation Materials Research Science and Engineering Center Grant DMR-0819860) and of the National Science Foundation (Grant CHE-0908265).

Bibliography

[1] M. Alcoutlabi and G. B. McKenna, J. Phys. Condens. Matter **17**, R461 (2005).

[2] C. Y. Kwong, A. B. Djurisic, V. A. L. Roy, P. T. Lai, and W. K. Chan, Thin Sol. Films **458**, 281 (2004).

[3] S. O. Kim *et al.*, Nature **424**, 411 (2003).

[4] A. N. Khramov, N. N. Voevodin, V. N. Balbyshev, and M. S. Donley, Thin Sol. Films **447-448**, 549 (2004).

[5] Y. Huang and D. R. Paul, Polymer **45**, 8377 (2004).

[6] M. Mu, A. M. Walker, J. M. Torkelson, and K. I. Winey, Polymer **49**, 1332 (2008).

[7] J. M. Kropka, V. Pryamitsyn, and V. Ganesan, Phys. Rev. Lett. **101**, 075702 (2008).

[8] A. Bansal *et al.*, Nature Materials **4**, 693 (2005).

[9] R. D. Priestley, C. J. Ellison, L. J. Broadbelt, and J. M. Torkelson, Science **309**, 456 (2005).

[10] C. J. Ellison and J. M. Torkelson, Nature Materials **2**, 695 (2003).

[11] R. D. Priestley, Soft Matter **5**, 919 (2009).

[12] J. Matthiesen, R. S. Smith, and B. D. Kay, Phys. Rev. Lett. **103**, 245902 (2009).

[13] Z. Fakhraai and J. A. Forrest, Phys. Rev. Lett. **95**, 025701 (2005).

[14] Z. Fakhraai and J. A. Forrest, Science **319**, 600 (2008).

[15] D. Qi, Z. Fakhraai, and J. A. Forrest, Phys. Rev. Lett. **101**, 096101 (2008).

[16] B. M. Besancon, C. L. Soles, and P. F. Green, Phys. Rev. Lett. **97**, 057801 (2006).

[17] H. Bodiguel and C. Fretigny, Phys. Rev. Lett. **97**, 266105 (2006).

[18] W. Zheng and S. L. Simon, J. Chem. Phys. **127**, 194501 (2007).

[19] M. K. Mukhopadhyay *et al.*, Phys. Rev. Lett. **101**, 115501 (2008).

[20] A. Serghei, M. Tress, and F. Kremer, J. Chem. Phys. **131**, 154904 (2009).

[21] T. Koga *et al.*, Phys. Rev. Lett. **104**, 066101 (2010).

[22] S. Xu, P. A. O'Connell, and G. B. McKenna, J. Chem. Phys. **132**, 184902 (2010).

[23] A. K. Kandar, R. Bhattacharya, and J. K. Basu, J. Chem. Phys. **133**, 071102 (2010).

[24] M. Sikorski, C. Gutt, Y. Chushkin, M. Lippmann, and H. Franz, Phys. Rev. Lett. **105**, 215701 (2010).

[25] Z. Yang, Y. Fujii, F. K. Lee, C. H. Lam, and O. K. C. Tsui, Science **328**, 1676 (2010).

[26] O. K. C. Tsui, Anomalous dynamics of polymer films, in *Polymer Thin Films*, edited by O. K. C. Tsui and T. P. Russell, pp. 267–294, World Scientific, Singapore, 2008.

[27] Z. Jiang *et al.*, Phys. Rev. Lett. **98**, 227801 (2007).

[28] Y. Chushkin, C. Caronna, and A. Madsen, Europhys. Lett. **83**, 36001 (2008).

[29] S. F. Swallen *et al.*, Science **315**, 353 (2007).

[30] K. L. Kearns, S. F. Swallen, M. D. Ediger, T. Wu, and L. Yu, J. Chem. Phys. **127**, 154702 (2007).

[31] K. L. Kearns *et al.*, J. Phys. Chem. B **112**, 4934 (2008).

[32] K. J. Dawson, K. L. Kearns, M. D. Ediger, M. J. Sacchetti, and G. D. Zografi, J. Phys. Chem. B **113**, 2422 (2009).

[33] K. J. Dawson, K. L. Kearns, L. Yu, W. Steffen, and M. D. Ediger, Proc. Natl. Acad. Sci. U.S.A. **106**, 15164 (2009).

[34] K. L. Kearns, M. D. Ediger, H. Huth, and C. Schick, J. Phys. Chem. Lett. **1**, 388 (2010).

[35] K. L. Kearns, T. Still, G. Fytas, and M. D. Ediger, Adv. Materials **22**, 39 (2010).

[36] E. León-Gutierrez, G. Garcia, M. Clavaguera-Mora, and J. Rodríguez-Viejo, Thermochim. Acta **492**, 51 (2009).

[37] E. León-Gutierrez, G. Garcia, A. F. Lopeandia, M. T. Clavaguera-Mora, and J. Rodríguez-Viejo, J. Phys. Chem. Lett. **1**, 341 (2010).

[38] E. León-Gutierrez, A. Sepúlveda, G. Garcia, M. Clavaguera-Mora, and J. Rodríguez-Viejo, Phys. Chem. Chem. Phys. **12**, 14693 (2010).

[39] J. D. Stevenson and P. G. Wolynes, J. Chem. Phys. **129**, 234514 (2008).

[40] T. M. Truskett and V. Ganesan, J. Chem. Phys. **119**, 1897 (2003).

[41] J. Mittal, J. R. Errington, and T. M. Truskett, Phys. Rev. Lett. **96**, 177804 (2006).

[42] J. Ghosh and R. Faller, J. Chem. Phys. **125**, 044506 (2006).

[43] J. Ghosh and R. Faller, J. Chem. Phys. **128**, 124509 (2008).

[44] F. Calvo and D. J. Wales, J. Chem. Phys. **131**, 134504 (2009).

[45] T. G. Lombardo, N. Giovambattista, and P. G. Debenedetti, Faraday Discuss. **141**, 359 (2008).

[46] K. Binder, A. Milchev, and J. Baschnagel, Annu. Rev. Mater. Sci. **26**, 107 (1996).

[47] C. Mischler, J. Baschnagel, and K. Binder, Adv. Coll. Interf. Sci. **94**, 197 (2001).

[48] F. Varnik, J. Baschnagel, and K. Binder, Phys. Rev. E **65**, 021507 (2002).

[49] Q. Wang, Q. Yan, P. F. Nealey, and J. J. de Pablo, J. Chem. Phys. **112**, 450 (2000).

[50] J. A. Torres, P. F. Nealey, and J. J. de Pablo, Phys. Rev. Lett. **85**, 3221 (2000).

[51] D. S. Fryer *et al.*, Macromol. **34**, 5627 (2001).

[52] R. S. Tate *et al.*, J. Chem. Phys. **115**, 9982 (2001).

[53] T. S. Jain and J. J. de Pablo, Macromol. **35**, 2167 (2002).

[54] T. S. Jain and J. J. de Pablo, Phys. Rev. Lett. **92**, 155505 (2004).

[55] K. Yoshimoto, T. S. Jain, P. F. Nealey, and J. J. de Pablo, J. Chem. Phys. **122**, 144712 (2005).

[56] R. A. Riggleman, K. Yoshimoto, J. F. Douglas, and J. J. de Pablo, Phys. Rev. Lett. **97**, 045502 (2006).

[57] S. Peter, H. Meyer, and J. Baschnagel, J. Chem. Phys., 131 **131**, 014902 (2009).

[58] S. Peter, H. Meyer, and J. Baschnagel, J. Chem. Phys. **131**, 014903 (2009).

[59] S. Léonard and P. Harrowell, J. Chem. Phys. **133**, 244502 (2010).

[60] W. Kob and H. C. Andersen, Phys. Rev. E **51**, 4626 (1995).

[61] F. H. Stillinger and T. A. Weber, Phys. Rev. A **25**, 978 (1982).

[62] F. H. Stillinger and T. A. Weber, Science **225**, 983 (1984).

[63] F. H. Stillinger, Science **267**, 1935 (1995).

[64] F. H. Stillinger, Phys. Rev. E **59**, 48 (1999).

[65] W. G. Hoover, Phys. Rev. A **31**, 1695 (1985).

[66] R. Godawat, S. N. Jamadagni, J. R. Errington, and S. Garde, Ind. Eng. Chem. Res. **47**, 3582 (2008).

[67] R. Fletcher and C. M. Reeves, Computer Journal **7**, 149 (1964).

[68] J. S. Rowlinson and B. Widom, *Molecular Theory of Capillarity* (Dover, New York, 2002).

[69] W. Smith, Calculating the pressure, Collaborative Computational Projects 5 (CCP5): `http://www.ccp5.ac.uk/ftpfiles/ccp5.newsletters/39/pdf/smith.pdf`, 1993.

[70] K. J. Dawson, L. Zhu, L. Yu, and M. D. Ediger, J. Phys. Chem. B (in press).

Chapter 6

Interface Induced Processes: A Study of Free Standing Films Composed of Rigid Molecules

6.1 Introduction

The effects of surfaces and interfaces, and of the inherent spatial heterogeneity that they create, on the structural, dynamic and thermodynamic properties of amorphous materials, have been investigated extensively both in experiments[1–12] and simulations[13–32]. One particularly noteworthy recent experimental discovery is that thin glassy films with exceptional kinetic and thermodynamic stability can be formed by vapor deposition[33–41]. Compared to ordinary glass of the same material formed by bulk phase quenching, these vapor deposited films have higher density, lower enthalpy, and a higher glass transition temperature. These films also exhibit enhanced mobility at the free surface[42, 43] and anisotropic molecular packing[44, 45]. The underlying mechanism causing the enhanced kinetic stability is still being actively researched[46–48]. In our prior computational study of free-standing films composed of binary Lennard-Jones particles in Chapter 5[32], we observed a substantial enhancement of lateral mobility at the surface with respect to the film's interior, and found that, upon potential energy minimization, particles residing at the free surface are able to descend deeper down the energy landscape than particles in the film's interior. Here, we present a follow up study of free-standing films composed of a model molecular system, namely the Lewis and

Wahnström model for *ortho*-terphenyl molecules.

Ortho-terphenyl (1,2-diphenylbenzene, OTP) is a well-known glass forming substance and has been extensively studied[49–57] as a canonical example of a fragile system in the Angell strong-fragile classification scheme[58]. For computational studies, Lewis and Wahnström (LW) introduced a greatly simplified model of the full *ortho*-terphenyl structure[59–61], where each phenyl ring is represented by a Lennard-Jones site, and the three sites constitute a rigid triangle. This model does not crystallize easily[59, 60], and has subsequently been used in a number of computational studies on glassy behavior[62–71]. We note, however, that Pedersen *et al.*[71] reported crystallization in this model in μs-long simulations. In the present chapter, we introduce orientational degrees of freedom in a simple and straightforward way by considering the LW-OTP system.

The additional rotational degrees of freedom inherent in a molecular system allow us to explore a number of properties that are inaccessible to an atomic system, such as spatially-dependent molecular orientation and rotational diffusion. Furthermore, in our previous study presented in Chapter 5, a binary Lennard-Jones system was chosen to avoid crystallization. This, however, resulted in a significant compositional inhomogeneity across the film, with the larger and compositionally more numerous particles enriched at the surface with respect to the mixture's overall composition[32]. The inherent compositional difference of the surface compared to the interior complicates the understanding of the surface effects observed for these binary films: are these effects due to the presence of an interface, or do they simply result from a difference in composition? In the present study, we seek to clarify this question, among others, by considering films composed of only one species (the LW-OTP molecule). Thus, by definition, the composition is uniform throughout, and any properties that differ at the surface when compared to the interior can be attributed directly to the presence of the interface.

In this chapter, we expand on the study presented in Chapter 5[32], and investigate the extent to which the results from the binary Lennard-Jones films extend to a single-component molecular system. In Section 6.2 we describe our molecular model and the numerical techniques employed in this investigation. Results on the film's structure, molecular orientational ordering, layer-by-layer dynamics, and energetics, including an analysis of minimum-energy configurations (inherent structures)[72–75], are presented in Section 6.3. The major conclusions as well as suggestions for further investigation are the subject of the concluding Section 6.4.

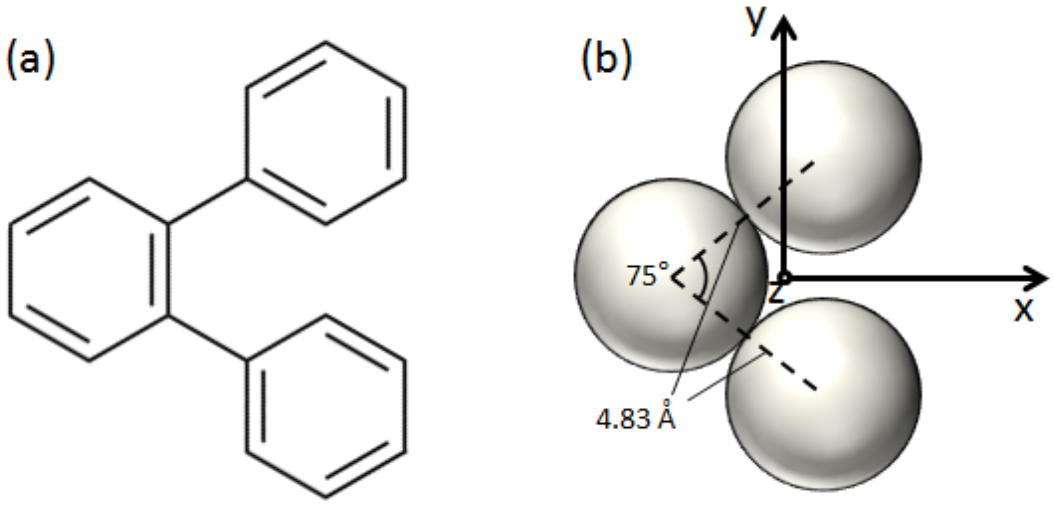

Figure 6.1: Comparison of the chemical structure of *ortho*-terphenyl (a) and the Lewis and Wahnström model (b), where each phenyl ring is represented by a Lennard-Jones site. For panel (b), the z axis points out of the page, and the origin coincides with the center of mass of the molecule. The coordinate axes correspond to the three rotational axes of the molecule.

6.2 Methods

The molecular system used for this study is the Lewis and Wahnström model for *ortho*-terphenyl[61] (LW-OTP). In this model, each phenyl ring is represented by a Lennard-Jones site ($\epsilon = 5.276$ kJ/mol, $\sigma = 4.83$ Å), and the three sites constitute a rigid isosceles triangle, with a vertex angle of 75° and a bond length of 4.83 Å for the two equal sides (Figure 6.1). In order to ensure continuity of the potential and its first derivative at a cutoff distance r_c, we use a shifted force (sf) Lennard-Jones potential for intermolecular interactions between "atomic" sites (force centers):

$$\phi^{sf}(r) = \begin{cases} \phi(r) - \phi(r_c) - (r - r_c)\phi'(r_c) & r \leq r_c \\ 0 & r > r_c \end{cases}, \tag{6.1}$$

where $\phi(r)$ is the Lennard-Jones $(12, 6)$ potential, and the cutoff distance used here is $r_c = 2.5\sigma$. For simplicity, each site is assigned the same mass $m = 78$ g/mol. The rigid bond constraints are maintained by the SHAKE[76] algorithm. This model for OTP, while simplistic, allows us to study films composed of simple rigid bodies with orientational degrees of freedom.

To simulate the free-standing film, we use a computational cell with periodic boundary conditions that is stretched in the z direction, with dimensions ($100 \times 100 \times 200$ Å^3). We consider two film

thicknesses in this study: "thin" films composed of 1014 molecules (thickness $\sim 7\sigma$), and "thick" films composed of 2028 molecules (thickness $\sim 13\sigma$). The simulation length along the z-axis is large enough such that the film does not interact with its periodic images in the z direction. The entire simulation is run at fixed particle number, total volume, and temperature (N, V, T), with a Nosé-Hoover thermostat[77]. To initialize these films, we first place an OTP molecule, by replication, on each point of a $13 \times 13 \times 6$ or $13 \times 13 \times 12$ cubic lattice, respectively for thin and thick films, spanning the entire xy plane and centered in the z direction. These lattice dimensions are chosen so that the resulting spacings between molecules do not result in large repulsions. This crystal structure is then allowed to relax, and the attractive forces between molecules result in a film-like structure. The system is then equilibrated for 50 ns, after which a production run of 1 μs is used for analysis. Across all simulations in this study, no molecules are ever observed to be ejected from the surface of the film. Thus, the center of mass of the film remains fixed throughout a given simulation.

Because the LW-OTP model does not crystallize easily, we note that, when compared to our previous study of atomic based films, we are able to simulate at a lower reduced temperature, $T^* = k_B T/\epsilon$. The highest temperature used in this study, 300 K, corresponds to a reduced temperature of 0.473, whereas the lowest reduced temperature used in the previous study[32] was 0.5.

6.3 Results and Discussion

6.3.1 Film Structure

We calculated the density profile using two different criteria: One, which we will refer to as the "atomic density profile", is based on the position of the individual atomic sites; the other, which we will call the "molecular density profile", is based on the position of the molecular center of mass. In each case, we divide the film into 1 Å-thick slices in the z direction, and then count the resulting number of atomic sites or molecular centers of mass in each slice, from which a mass density is calculated. The red lines of Figure 6.2 show the atomic density profile for both thin and thick films at $T = 270$ K and $T = 300$ K[78]. The atomic density is uniform throughout the interior of the film, while across the interface it can be fitted to a hyperbolic tangent curve:

$$\rho(z) = \frac{1}{2}\rho_L \left[1 - \tanh\left(\frac{2(|z| - z_e)}{d}\right)\right]. \tag{6.2}$$

Equation 6.2 provides us with a set of parameters to characterize the physical properties of a film: ρ_L represents the interior density, z_e gives the location where the density decays to half the interior

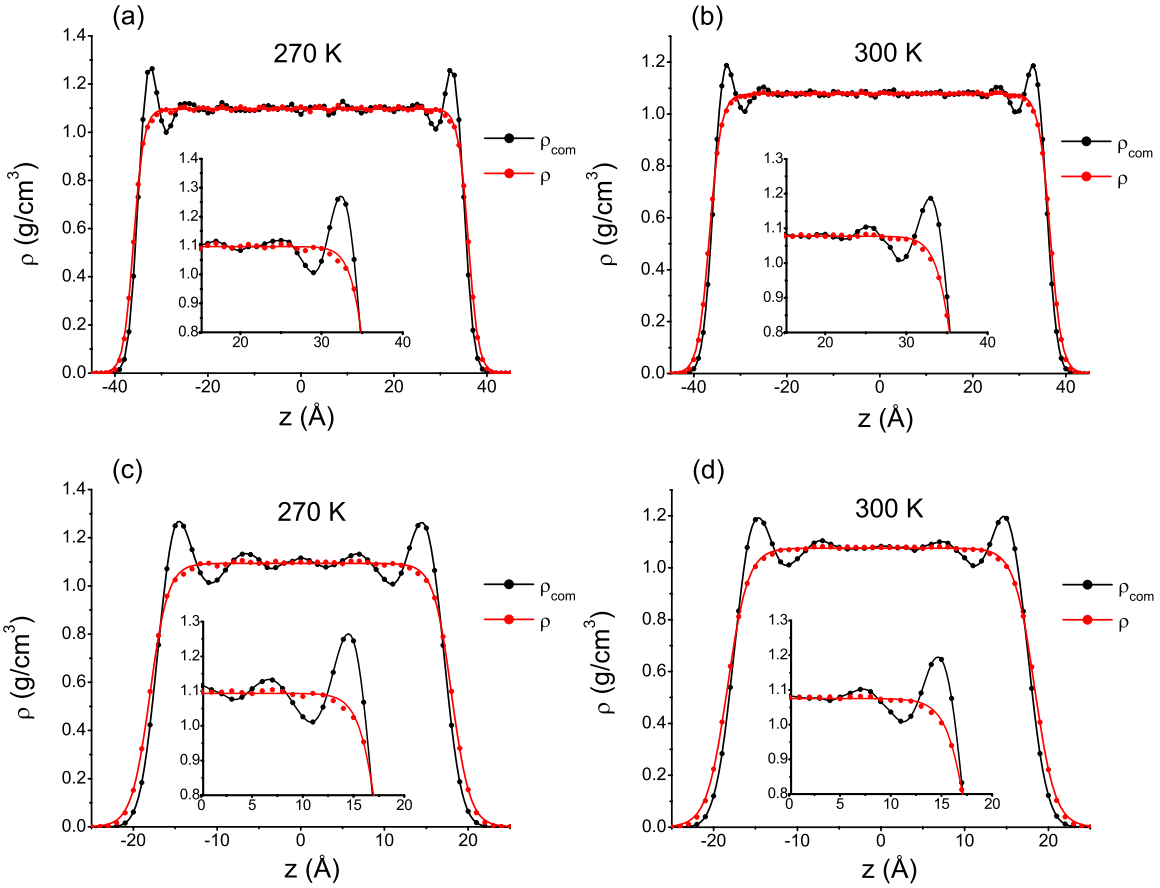

Figure 6.2: Density profiles for thick (a, b) and thin (c, d) films, at two different temperatures. The red points, ρ, are calculated by counting the number of atomic sites within a given Δz, while the black points, ρ_{com} result from counting the number of centers of mass. The red line is a hyperbolic tangent fit of the form given by Eq. 6.2. The black line is a spline that serves as a guide to the eye. The insets are close-ups of the interfacial region of each film. The data points in the insets are averaged over the z direction symmetry of the film.

value, and d is a characteristic length that defines the width of the interface. The range described by $|z| \in [z_e - d, z_e + d]$ corresponds to regions of the film where the density profile decreases from 98.2% of the interior value to 1.8%; hence, we will define the width of an interface to be $w = 2d$, and, because there is no vapor phase, we call the regions $|z| > z_e - d$ the "interfaces" of the free-standing film. Accordingly, we will refer to the region $|z| < z_e - d$, where the density remains essentially constant, as the "interior" of the film. Table 6.1 lists the parameters ρ_L, z_e, and d for both thick and thin films at 270 K and 300 K. We note that, at constant temperature, adding molecules to a film only changes the thickness of the interior, and does not appreciably change the interior density or the thickness of the interface.

These atomic density profiles directly reflect the distribution of matter within the films, and are

Film	ρ_L(g/cm^3)	z_e(Å)	d(Å)
Thick 270 K	1.096	35.981	4.352
Thin 270 K	1.094	18.047	4.336
Thick 300 K	1.078	36.615	4.933
Thin 300 K	1.075	18.362	4.861

Table 6.1: Fitted values of the interior density, ρ_L, location of the point where the density decreases to half its bulk value, z_e, and half interface thickness, d, for various free-standing films.

similar to the density profiles observed in previous studies[32, 79] of free-standing films consisting of monatomic systems. Indeed, we can consider our molecular system as a set of interacting atoms, with additional forces constraining the triplet of atoms that constitute a molecule. However, these additional intra-molecular forces make the films appreciably cohesive, and no molecules escape the film to form a vapor phase. This is in contrast to our purely atom-based film, where although at a slightly higher reduced temperature, a measurable vapor phase was found to be present[32].

The black lines of Figure 6.2 show the molecular density profile, where the location of each molecule is considered to be at its center of mass. The interface now exhibits significant damped density oscillations. These oscillations, present in the molecular density profile, but not in the atomic one, suggest orientational ordering at the film's surface.

We now define the orientation of a particular molecule with respect to the film by the angle, θ, between the unit vector normal to the plane containing the three atomic sites ($\hat{n}$), and the unit vector normal of the surface of the film, which in this case is the z direction. Thus, $\cos\theta = \hat{n}\cdot\hat{z}$, and $\theta \in [0, \pi/2]$. With this definition, a value of $\theta = 0$ indicates a molecule lying flat in the plane of the film, while a value of $\theta = \pi/2$ corresponds to a molecule oriented perpendicular to the film. If the molecules have no orientational preference, such as in a bulk system, the probability distribution function of the orientational angle θ is

$$P_{bulk}(\theta)\,\mathrm{d}\theta = \frac{2\pi\sin\theta\,\mathrm{d}\theta}{\int_0^{\pi/2} 2\pi\sin\theta\,\mathrm{d}\theta} = \sin\theta\,\mathrm{d}\theta. \tag{6.3}$$

Thus, the expectation value of θ, for a system with no orientational bias, is then

$$\langle\theta\rangle_{bulk} = \int_0^{\pi/2} \theta P_{bulk}(\theta)\,\mathrm{d}\theta = \int_0^{\pi/2} \theta\sin\theta\,\mathrm{d}\theta = 1. \tag{6.4}$$

For our systems, Figure 6.3 shows the average orientational angle of molecules for a given center-of-mass position z. Once again, a damped oscillatory trend appears. Moving from the surface to the bulk, the average angle alternates between overshooting and undershooting the average bulk value

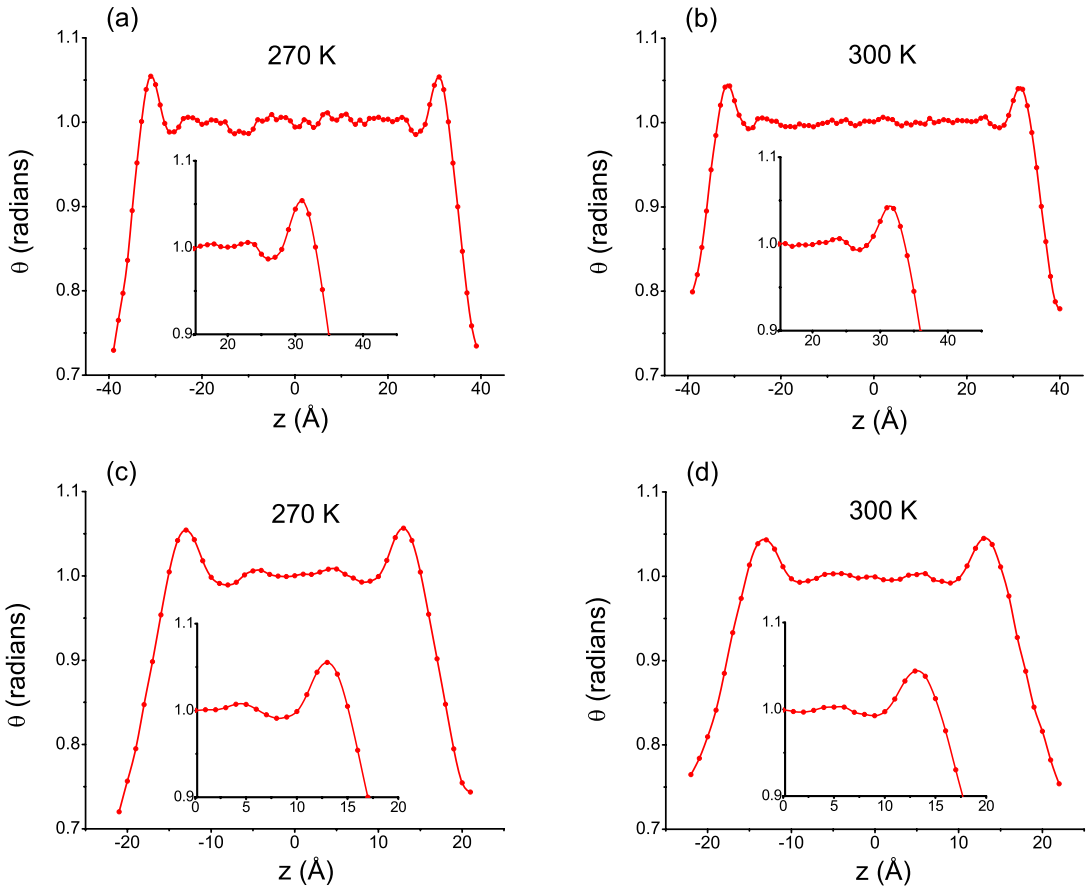

Figure 6.3: Profiles of the average value of the angle, θ, spanned by the unit vector normal to the plane containing the three Lennard-Jones centers for a given OTP molecule, and the unit vector normal to the film interface ($\hat{z}$). Data are shown for thick (a, b) and thin (c, d) films, at two different temperatures. The bulk value, with completely random angular orientational preference, corresponds to $\langle\theta\rangle_{bulk} = 1$. The insets are close-ups of the interfacial region of each film, and the data points in the insets are averaged over the z direction symmetry of the film. The damped oscillatory surface-induced ordering is evident.

of 1. These fluctuations correlate with the oscillations of the molecular density profile, and suggest that a particular orientational ordering of molecules in a layer induces an opposite ordering in the layers adjacent to it. In this case, at the surface of the film, the molecules experience intermolecular attractive forces from only one direction, and are more likely to lie flat on the film surface, i.e., $\theta < 1$. The layer below instead has a preference to be orientationally biased in the perpendicular direction ($\theta > 1$), and the layer below that once again has a slight preference to lie flat ($\theta < 1$), and so on.

This "surface induced ordering" is further illustrated in Figure 6.4, where we show a normalized

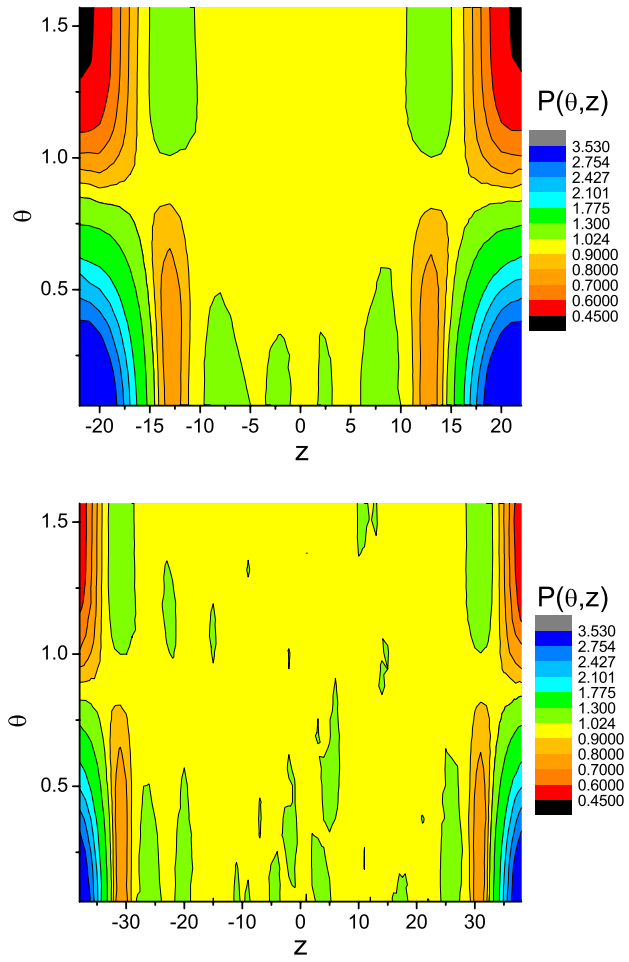

Figure 6.4: Probability distribution contour plot for molecular orientations, $P(\theta, z)$ for thin (top) and thick (bottom) films at $T = 270$ K. $P(\theta, z)$ is normalized with respect to a bulk distribution, i.e., $P(\theta, z) > 1$ indicates an occurrence more likely than the bulk average, while $P(\theta, z) < 1$ indicates less likelihood of occurrence. While the surface regions [$|z| > 13.6$ Å(top), 31.6 Å(bottom)] vividly show a molecular orientational preference, the areas of green in the center of the film [$|z| < 13.6$ Å(top), 31.6 Å(bottom)] suggest that the surface induces an ordering that penetrates deep into the film. The contour plots at $T = 300$ K are qualitatively similar, although the contour lines are not as smooth due to increased thermal fluctuations.

probability distribution function, $P(\theta, z)$, defined by

$$P(\theta, z) = \frac{P_{film}(\theta, z)}{P_{bulk}(\theta)} = \frac{P_{film}(\theta, z)}{\sin\theta}, \tag{6.5}$$

where $P_{film}(\theta, z)$ is the orientational probability distribution function at a given film depth z. $P_{film}(\theta, z)$ is normalized on the interval $\theta \in [0, \pi/2]$ for any particular value of z, i.e., at a given film depth $z = z'$,

$$\int_0^{\pi/2} P(\theta, z)\Big|_{z=z'} \, \mathrm{d}\theta = 1. \tag{6.6}$$

The value of $P(\theta, z)$, when compared to unity, then directly reflects whether a particular value of θ is more or less favored relative to an orientationally unbiased (bulk) system, for molecules located at a depth of z. Note the alternating coloring as a function of z for fixed values of θ, which shows the alternating orientational ordering preference of the molecules.

Based on the atomic density profile hyperbolic tangent fits, the films reach a bulk density at $|z| = z_e - d$, where the density profile begins to plateau. This corresponds to $|z| \approx 13.5$ Å for thin films and $|z| \approx 31.6$ Å for thick films. Strikingly, the oscillations of the molecular density profile, while most prominent at the interface of the film, continue in regions where the atomic density essentially is constant. From the insets of Figure 6.2, these oscillations persist well into the interior of the thin films, and are visible until roughly $|z| = z_e - 4d \approx 18$ Å for the thicker films. This suggests that the effects of the surface induced ordering can extend deep below the surface; if $w = 2d$ is the width of the interface, then the orientational oscillations are detectable until a depth of $1.5w$ into the interior.

6.3.2 Stress

Similar to our previous study[32], we calculated the pressure normal and parallel to the xy plane, $P^{\perp} = P_{zz}$ and $P^{\parallel} = (P_{xx} + P_{yy})/2$, respectively, as a function of z. The atom-based virial expression[80–82], which takes into account both intermolecular and intramolecular forces on each atom, is used to compute the three diagonal components of the stress tensor in slices of thickness $\Delta z = 1$ Å. Figure 6.5 shows the lateral and normal stress profiles for thin films at $T = 270$ K and 300 K. These stress profiles are similar to those of films composed of binary atomic Lennard-Jones spheres[32]. Both the lateral and normal stresses predominantly occur at the interfaces, defined by $|z| > z_e - d \approx 13.6$ Å for thin films. In particular, the region of appreciable tensile lateral stress is nearly entirely contained within the two interfaces. The film's interfaces are also under tensile

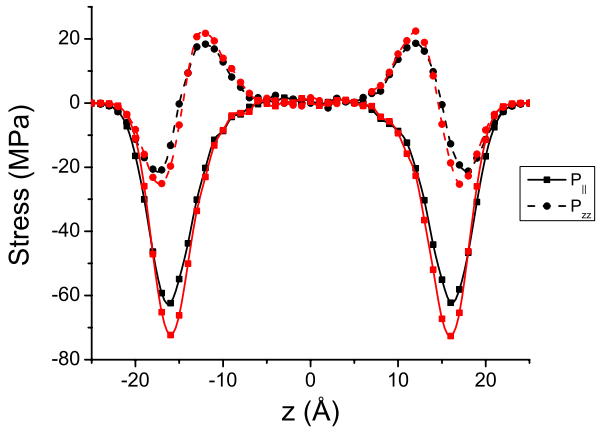

Figure 6.5: The lateral (solid) and normal (dashed) stress profiles plotted as a function of film depth z for a film of $T = 300$ K (black) and 270 K (red). Here, positive values correspond to compression, and negative values to tension.

normal stress, but appreciable normal compression develops in a region closer to the center.

For a free-standing film perpendicular to the z axis, the surface tension γ can be expressed as[83, 84]

$$\gamma = \frac{1}{2}\int_{-\infty}^{\infty}[P^{\perp}(z) - P^{\parallel}(z)]\mathrm{d}z, \tag{6.7}$$

where 1/2 prefix arises due to each film having two interfaces. This results in a calculated surface tension of 43.7 and 40.43 dyne/cm at 300 and 270 K respectively for the LW-OTP model. The surface tension for real OTP, obtained by using a functional fit to experimental data[85], is 42.1 dyne/cm at 300 K. We note that the Lewis and Wahnström model for OTP, although greatly simplified, predicts a surface tension that is with 5% of the experimental value.

The variation of stresses across the depth of the film indicates that the predominant contribution to the film's mechanical properties is configurational. The magnitude of all stresses also increases upon lowering the temperature. The stress profiles for the thick films are similar to the thin ones, with the only difference being an extended interior region where both the lateral and normal stresses are negligible.

6.3.3 Dynamics

Due to the anisotropic nature of the film, particle motion differs in the normal and lateral directions. In this study, we focus on the lateral translational diffusion, and on the rotational diffusion of each molecule, both as a function of z_{com}, where z_{com} is the z value of the center-of-mass location of a

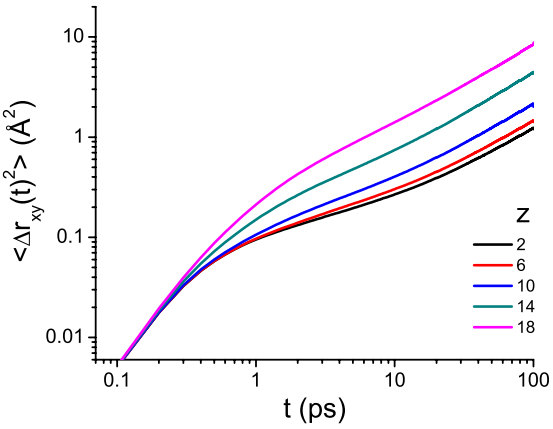

Figure 6.6: The lateral mean squared displacement, for a thin film equilibrated at $T = 300$ K for a representative set of z values (in Å).

given molecule. To calculate the lateral translational center-of-mass diffusion, $D_{||}$, we define the diffusion coefficient with the following modified Einstein diffusion equation:

$$D_{||} = \frac{1}{4} \lim_{\tau \to \infty} \frac{d}{d\tau} \left\langle \Delta r_{||}(\tau)^2 \right\rangle_{\text{slice}} . \tag{6.8}$$

$\left\langle \Delta r_{||}(\tau)^2 \right\rangle_{\text{slice}}$ is the mean squared displacement of the particles that remain "in slice" after an interval duration of τ. Here, the "slice" condition means that the center of mass of a given molecule, at the end of the interval under consideration, is within a vertical displacement of 2 Å of its initial position, i.e., $|z_{i,com}(t) - z_{i,com}(t_0)| < 2$ Å. With this definition, a molecule is allowed to leave a given slice and return later. The resulting mean squared displacement trajectories are then averaged over bins of $\Delta z = 1$ Å. Figure 6.6 shows an example of the resulting mean squared displacement trajectories for a representative set of values of z. The lateral translational diffusion coefficient is then calculated from the slope of the region where $\left\langle \Delta r_{||}(\tau)^2 \right\rangle$ becomes linear. For all mean squared displacement trajectories, the time interval used to calculate these linear fits is $t \in [80, 120]$ ps.

Figure 6.7 shows the resulting diffusion coefficients as a function of z. As with the previous atomic system study[32], the molecules at the surface are more mobile than those in the bulk. In this case, the surface molecules have a diffusivity that is eight times that of the bulk at $T = 300$ K, and eighteen times the bulk at $T = 270$ K (compared to three times as much in the atomic case). As we approach the surface from the center of the film, the lateral diffusivity begins to slowly increase near $z = 6$ Å, and appreciably increase near $z = 11$ Å. When we compare z dependence of the lateral diffusion coefficients to the atomic density profile plots from the previous section, the increase in

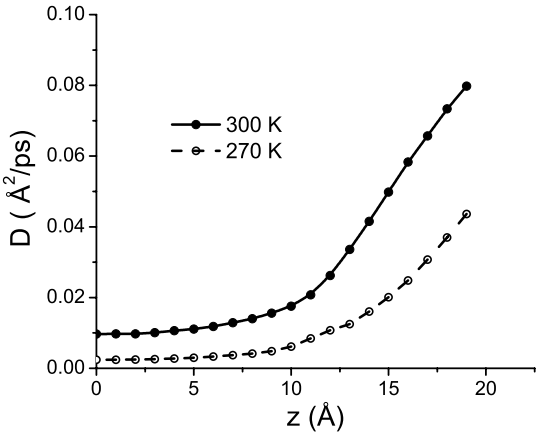

Figure 6.7: Lateral diffusion coefficients for a film equilibrated at $T = 300$ K (closed circles, solid line) and $T = 270$ K (open circles, dashed line). The diffusion rate at the surface is roughly eight times that of the interior at 300 K, and eighteen times the corresponding interior value at 270 K. The lines are guides to the eye.

diffusivity occurs well within the interior region of the film (defined by $|z| < z_e = d \approx 13.6$ Å), and where the density still remains constant. This again shows that surface induced effects can extend far below the interface; in this case, molecules have an appreciable increase in mobility even in the bulk-like density regions of the film.

We can further investigate the mobility of the molecules by calculating the rotational diffusion coefficient using an Einstein formulation similar to the translational diffusion equation[67]:

$$D_r^\alpha = \frac{1}{2} \lim_{\tau \to \infty} \frac{d}{d\tau} \left\langle \Delta\varphi^\alpha(\tau)^2 \right\rangle_{\text{slice}}, \tag{6.9}$$

where $\alpha \in [x, y, z]$ corresponds to the three principal axes of rotation in the molecular frame (Figure 6.1 shows how the axes of rotation are defined). $\varphi^\alpha(\tau)$ represents the integral of the rotations a molecule undergoes in time τ, and is calculated by summing the angular displacements about each axis of rotation between successive time steps. With this convention, we do no apply the 2π rotational periodicity, i.e., one full rotation about an axis corresponds to an angular displacement of 2π instead of 0. Using a similar "slice" constraint as for translational diffusion, we can then plot the resulting rotational mean squared displacements (Figure 6.8) and calculate the corresponding rotational diffusion coefficients (Figure 6.9). Note that the axis with the largest rotational diffusion rate, the y axis, corresponds to the one with the smallest moment of inertia. Overall, we see that rotational diffusion is also much higher at the surface than in the interior, further demonstrating that surface molecules have higher mobility than those in the bulk.

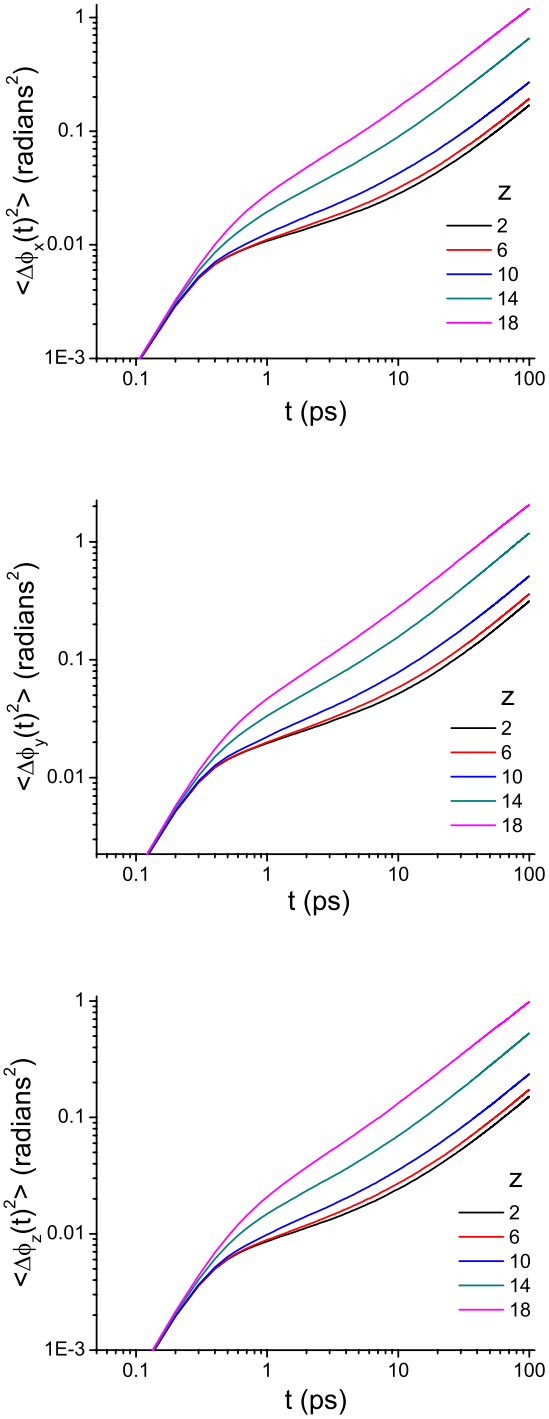

Figure 6.8: Rotational mean squared displacement, for a thin film equilibrated at $T = 300$ K for a representative set of z values (in Å).

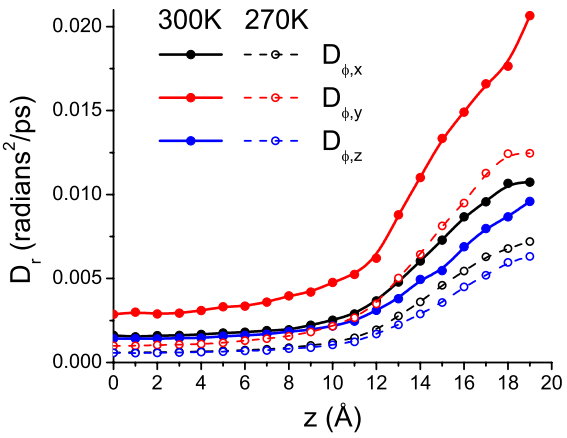

Figure 6.9: Rotational diffusion coefficients for a film equilibrated at $T = 300$ K (closed circles, solid lines) and $T = 270$ K (open circles, dashed lines) as a function of film depth. The three principal axes of rotation, x (black), y (red), and z (blue), are defined in Figure 6.1. The lines are guides to the eye.

At any given film depth, as the temperature is lowered, both translational and rotational diffusivity decrease. This is simply a result of reduced thermal fluctuations. However, when we scale each diffusion coefficient to the corresponding value in the center of the film (Figure 6.10), we see that the diffusivity at the interface *relative* to the interior instead becomes *greater* as the temperature is decreased. Thus, this mobility enhancement due to the presence of an interface, when defined relative to the corresponding interior value, *increases* upon cooling.

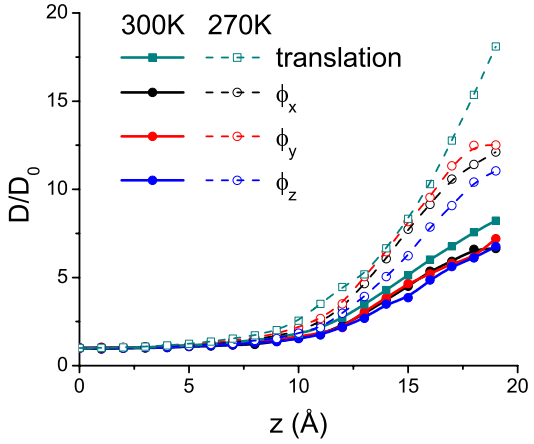

Figure 6.10: Translational (squares) and rotational (circles) diffusion coefficients scaled to their corresponding values at the center of the film, for films equilibrated at $T = 300$ K (filled symbols, solid lines) and 270 K (open symbols, dashed lines).

We also note that all the diffusion coefficients increase at roughly the same rate in the interior of

the film, and are thus coupled. However, as we approach the interfacial region ($|z| > 13.6$ Å) from the interior, the translational diffusion coefficients increase at a much faster rate than the corresponding three rotational diffusion coefficients. This indicates a decoupling of the rotational and translation motion, and suggests that in addition to being spatially heterogeneous, the interfacial region and the interior of a film are also inherently dynamically heterogeneous.

Although Figures 6.7, 6.9, and 6.10 show the translational and rotational diffusion coefficients for thin films composed of 1014 molecules, these figures are also representative for the thick films composed of 2028 molecules. At constant temperature, an increase in thickness does not appreciably change the interfacial region of a film. Because the change in diffusivity, across the depth of a film, occurs at or near the interface, corresponding plots for a thicker film simply show an extended constant interior region where the diffusivity reaches the bulk limit, while the interfacial region is quantitatively similar to that of the thin films.

6.3.4 Inherent Structures

For each film, we performed an energy minimization[86] on 7000 coordinate snapshots, each spaced 50 ps apart, to study the underlying inherent structures (potential energy landscape minima)[72] of these films. For each snapshot, we apply the Fletcher and Reeves[86] method of conjugate gradients. The force and torque of each molecule are iteratively recalculated as the molecules are moved and rotated along the gradient of the film's $6N$-dimensional energy landscape. This process is continued until a minimum is reached; the criterion for convergence is when successive iterations reduce the system energy by less than one part in 10^{12}.

We define $u_i = \frac{1}{2}\Sigma_j \phi_{\alpha\beta}(r_{ij})$ as the potential energy attributed to an atom, i.e., for every pair interaction between two atoms, half of the potential energy is assigned to one atom and half to the other. We will also denote by z_0 the z coordinate of a particle before minimization. Similarly, let u_0 denote average potential energy per atom before minimization, while u_{IS} is the corresponding inherent structure quantity. We plot the difference $u_{IS} - u_0$ as a function of z_0 (Figure 6.11). These results are analogous to those of the binary Lennard-Jones atomic films[32]. At the film interface, the quantity $|u_{IS} - u_0|$ is much larger than in the interior. In other words, on average, the particles at the surface of the film descend more deeply down their portion of the energy landscape than particles in the film's interior. This is in agreement with theoretical predictions[87], and with the interpretation of the molecular mechanisms underlying the enhanced stability of slow-grown vapor-deposited glasses[33, 34]. It further suggests that particles at the surface are able to explore the

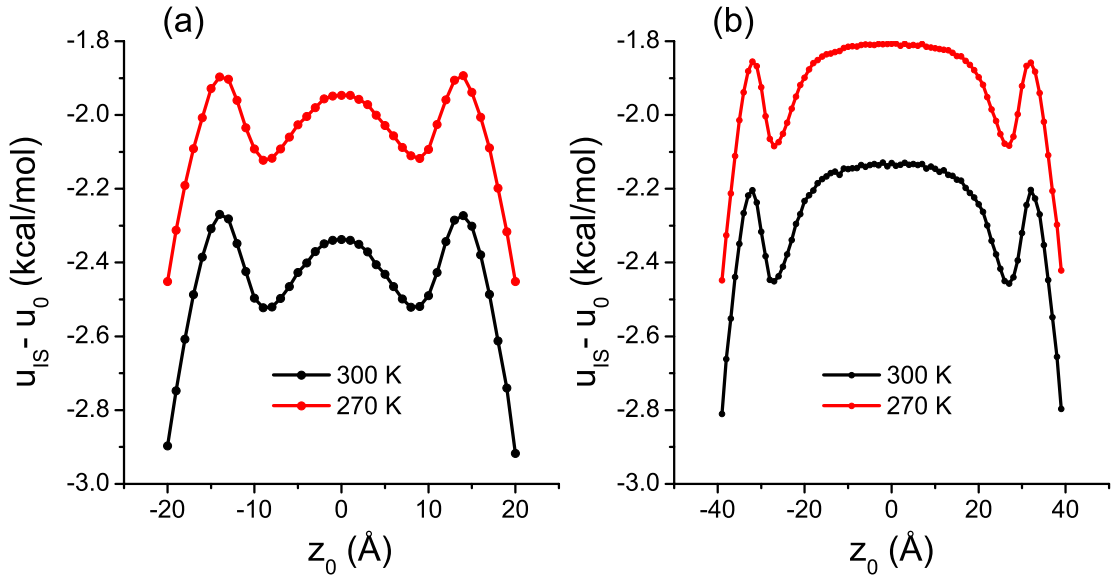

Figure 6.11: Average difference of the energy of an atom with respect to its corresponding inherent structure energy, as a function of the initial position before minimization, z_0, for thin (a) and thick (b) films equilibrated at $T = 300$ K and 270 K. Note that $u_{is} - u_0$ is negative, thus $|u_{is} - u_0|$ is greatest at the surface, which indicates that the molecules initially at the surface descend deeper down the energy landscape upon energy minimization.

energy landscape more effectively, and points to the pronounced basin anharmonicity introduced by the presence of free surfaces; if the system were harmonic, $u_0 - u_{IS}$ would equal $\frac{3}{2}k_BT$ on a per-particle basis, independent of z.

The difference $|u_{IS} - u_0|$ is also a measure of how far energetically an atom is from its underlying inherent structure energy. This can be interpreted as a measure of stability, i.e., a region of lower $|u_{IS} - u_0|$ is more stable, in the sense that its energy differs by a comparatively smaller amount from that corresponding to the mechanically stable state (inherent structure). We see that as we move away from the center, $|u_{IS} - u_0|$ does not increase monotonically, and near the boundary of the film interior and the film interface ($|z| \approx 13.6$ Å), there is a notable minimum in the absolute difference. In this interpretation, this region is then the most energetically stable region of the film. This non-monotonic behavior, first observed in our previous study of atomic based free-standing films[32], and now reproduced for a molecular system, suggests that this is a surface-induced effect, largely insensitive to system composition.

6.4 Conclusions

In this chapter, we investigated the properties of films composed of model rigid molecules. This project complements an earlier study of thin films composed of atomic particles. We used a three site model of OTP constrained by rigid bonds. Compared to the atomic binary Lennard-Jones case of Chapter 5[32], the films are more cohesive, with no molecules ever being ejected into the vapor phase at $T \leq 300\ K$. We do, however, observe a higher mobility of the molecules near the surface of the film when compared to the bulk. Furthermore, as we approach the surface from the bulk, the rate of increase in translational and rotational diffusivity become decoupled, suggesting the presence of dynamic heterogeneities[88] in the system. We also observe a similar inherent structure energy difference profile when compared to the binary Lennard-Jones study, which suggests that particles residing at the free surface are able to descend deeper down the energy landscape than particles in the film's interior, and indicates the strong basin anharmonicity introduced by the free surfaces.

One notable different feature with respect to the atomic study is the dampened oscillatory center-of-mass density profile. This oscillatory behavior is also evident in the average orientation of molecules within the film. Given a characteristic interfacial width w, the orientational oscillations are noticeable until a depth of $1.5w$ into the film's interior. This strongly suggests that the orientational ordering of molecules, while induced by the presence of an interface, extends well below the interface.

It would be interesting to investigate whether this "sub-surface region" of surface-induced ordering, and the decoupling of translation and rotational diffusion, appear in films composed of other non-spherical molecules, such as rod-like molecules or chains. Additionally, it would be useful to understand how this orientational ordering applies to surface effects observed experimentally. Finally, most experiments are conducted on supported films, whereas our simulations have so far explored free-standing films. We believe it is important to understand the effects of a substrate on the dynamic and structural phenomena reported here and in the previous chapter[32].

6.5 Acknowledgments

The financial support of the National Science Foundation is gratefully acknowledged (Grant CHE-1213343 to PGD). Calculations were performed at the Terascale Infrastructure for Groundbreaking Research in Engineering and Science (TIGRESS) at Princeton University.

Bibliography

[1] R. D. Priestley, C. J. Ellison, L. J. Broadbelt, and J. M. Torkelson, Science **309**, 456 (2005).

[2] Z. Fakhraai and J. A. Forrest, Phys. Rev. Lett. **95**, 025701 (2005).

[3] Z. Fakhraai and J. A. Forrest, Science **319**, 600 (2008).

[4] D. Qi, Z. Fakhraai, and J. A. Forrest, Phys. Rev. Lett. **101**, 096101 (2008).

[5] B. M. Besancon, C. L. Soles, and P. F. Green, Phys. Rev. Lett. **97**, 057801 (2006).

[6] H. Bodiguel and C. Fretigny, Phys. Rev. Lett. **97**, 266105 (2006).

[7] W. Zheng and S. L. Simon, J. Chem. Phys. **127**, 194501 (2007).

[8] M. K. Mukhopadhyay *et al.*, Phys. Rev. Lett. **101**, 115501 (2008).

[9] A. Serghei, M. Tress, and F. Kremer, J. Chem. Phys. **131**, 154904 (2009).

[10] T. Koga *et al.*, Phys. Rev. Lett. **104**, 066101 (2010).

[11] S. Xu, P. A. O'Connell, and G. B. McKenna, J. Chem. Phys. **132**, 184902 (2010).

[12] A. K. Kandar, R. Bhattacharya, and J. K. Basu, J. Chem. Phys. **133**, 071102 (2010).

[13] K. Binder, A. Milchev, and J. Baschnagel, Annu. Rev. Mater. Sci. **26**, 107 (1996).

[14] C. Mischler, J. Baschnagel, and K. Binder, Adv. Coll. Interf. Sci. **94**, 197 (2001).

[15] F. Varnik, J. Baschnagel, and K. Binder, Phys. Rev. E **65**, 021507 (2002).

[16] Q. Wang, Q. Yan, P. F. Nealey, and J. J. de Pablo, J. Chem. Phys. **112**, 450 (2000).

[17] J. A. Torres, P. F. Nealey, and J. J. de Pablo, Phys. Rev. Lett. **85**, 3221 (2000).

[18] D. S. Fryer *et al.*, Macromol. **34**, 5627 (2001).

[19] R. S. Tate *et al.*, J. Chem. Phys. **115**, 9982 (2001).

[20] T. S. Jain and J. J. de Pablo, Macromol. **35**, 2167 (2002).

[21] T. S. Jain and J. J. de Pablo, Phys. Rev. Lett. **92**, 155505 (2004).

[22] K. Yoshimoto, T. S. Jain, P. F. Nealey, and J. J. de Pablo, J. Chem. Phys. **122**, 144712 (2005).

[23] R. A. Riggleman, K. Yoshimoto, J. F. Douglas, and J. J. de Pablo, Phys. Rev. Lett. **97**, 045502 (2006).

[24] S. Peter, H. Meyer, and J. Baschnagel, J. Chem. Phys., 131 **131**, 014902 (2009).

[25] S. Peter, H. Meyer, and J. Baschnagel, J. Chem. Phys. **131**, 014903 (2009).

[26] T. M. Truskett and V. Ganesan, J. Chem. Phys. **119**, 1897 (2003).

[27] J. Mittal, J. R. Errington, and T. M. Truskett, Phys. Rev. Lett. **96**, 177804 (2006).

[28] J. Ghosh and R. Faller, J. Chem. Phys. **125**, 044506 (2006).

[29] J. Ghosh and R. Faller, J. Chem. Phys. **128**, 124509 (2008).

[30] F. Calvo and D. J. Wales, J. Chem. Phys. **131**, 134504 (2009).

[31] T. G. Lombardo, N. Giovambattista, and P. G. Debenedetti, Faraday Discuss. **141**, 359 (2008).

[32] Z. Shi, P. G. Debenedetti, and F. H. Stillinger, J. Chem. Phys. **134**, 114524 (2011).

[33] S. F. Swallen *et al.*, Science **315**, 353 (2007).

[34] K. L. Kearns, S. F. Swallen, M. D. Ediger, T. Wu, and L. Yu, J. Chem. Phys. **127**, 154702 (2007).

[35] K. L. Kearns *et al.*, J. Phys. Chem. B **112**, 4934 (2008).

[36] K. J. Dawson, K. L. Kearns, M. D. Ediger, M. J. Sacchetti, and G. D. Zografi, J. Phys. Chem. B **113**, 2422 (2009).

[37] K. J. Dawson, K. L. Kearns, L. Yu, W. Steffen, and M. D. Ediger, Proc. Natl. Acad. Sci. U.S.A. **106**, 15164 (2009).

[38] K. L. Kearns, M. D. Ediger, H. Huth, and C. Schick, J. Phys. Chem. Lett. **1**, 388 (2010).

[39] K. L. Kearns, T. Still, G. Fytas, and M. D. Ediger, Adv. Materials **22**, 39 (2010).

[40] M. Ahrenberg *et al.*, J. Chem. Phys. **138**, 024501 (2013).

[41] K. R. Whitaker, M. Ahrenberg, C. Schick, and M. D. Ediger, J. Chem. Phys. **137**, 154502 (2012).

[42] A. Sepúlveda, S. F. Swallen, and M. D. Ediger, J. Chem. Phys. **138**, 12A517 (2013).

[43] A. Sepúlveda, S. F. Swallen, L. A. Kopff, R. J. McMahon, and M. D. Ediger, J. Chem. Phys. **137**, 204508 (2012).

[44] S. S. Dalal and M. D. Ediger, J. Phys. Chem. Lett. **3**, 1229 (2012).

[45] K. Dawson *et al.*, J. Chem. Phys. **136**, 094505 (2012).

[46] Z. Chen and R. Richert, J. Chem. Phys. **135**, 124515 (2011).

[47] Z. Chen, A. Sepúlveda, M. D. Ediger, and R. Richert, J. Chem. Phys. **138**, 12A519 (2013).

[48] S. Singh and J. J. de Pablo, J. Chem. Phys. **134**, 194903 (2011).

[49] J. N. Andrews and A. R. Ubbelohde, Proc. R. Soc. A **228**, 435 (1955).

[50] P. K. Dixon and S. R. Nagel, Phys. Rev. Lett. **61**, 341 (1988).

[51] G. Meier, B. Gerharz, D. Boese, and E. W. Fischer, J. Chem. Phys. **94**, 3050 (1991).

[52] F. Fujara, B. Geil, H. Sillescu, and G. Fleischer, Zeit. Phys. B **88**, 195 (1992).

[53] W. Petry *et al.*, Zeit. Phys. B **83**, 175 (1991).

[54] M. T. Cicerone and M. D. Ediger, J. Chem. Phys. **103**, 5684 (1995).

[55] B. Schiener, R. Bhmer, A. Loidl, and R. V. Chamberlin, Science **274**, 752 (1996).

[56] C. Hansen, F. Stickel, T. Berger, R. Richert, and E. W. Fischer, J. Chem. Phys. **107**, 1086 (1997).

[57] H. Sillescu, J. Non-Cryst. Solids **243**, 81 (1999).

[58] C. A. Angell, Science **267**, 1924 (1995).

[59] L. J. Lewis and G. Wahnström, Solid State Commun. **86**, 295 (1993).

[60] L. J. Lewis and G. Wahnström, J. Non-Cryst. Solids **172-174**, 69 (1994).

[61] L. J. Lewis and G. Wahnström, Phys. Rev. E **50**, 3865 (1994).

[62] G. Wahnström and L. J. Lewis, Physica A **201**, 150 (1993).

[63] C. M. Roland, K. L. Ngai, and L. J. Lewis, J. Chem. Phys. **103**, 4632 (1995).

[64] S. Mossa *et al.*, Phys. Rev. E **65**, 041205 (2002).

[65] S.-H. Chong and F. Sciortino, Phys. Rev. E **69**, 051202 (2004).

[66] E. La Nave, S. Mossa, F. Sciortino, and P. Tartaglia, J. Chem. Phys. **120**, 6128 (2004).

[67] T. G. Lombardo, P. G. Debenedetti, and F. H. Stillinger, J. Chem. Phys. **125**, 174507 (2006).

[68] U. R. Pedersen, N. Gnan, N. P. Bailey, T. B. Schrøder, and J. C. Dyre, J. Non-Cryst. Solids **357**, 320 (2011).

[69] T. B. Schrøder, N. P. Bailey, U. R. Pedersen, N. Gnan, and J. C. Dyre, J. Chem. Phys. **131**, 234503 (2009).

[70] T. B. Schrøder, U. R. Pedersen, N. P. Bailey, S. Toxvaerd, and J. C. Dyre, Phys. Rev. E **80**, 041502 (2009).

[71] U. R. Pedersen, T. S. Hudson, and P. Harrowell, J. Chem. Phys. **134**, 114501 (2011).

[72] F. H. Stillinger and T. A. Weber, Phys. Rev. A **25**, 978 (1982).

[73] F. H. Stillinger and T. A. Weber, Science **225**, 983 (1984).

[74] F. H. Stillinger, Science **267**, 1935 (1995).

[75] F. H. Stillinger, Phys. Rev. E **59**, 48 (1999).

[76] J.-P. Ryckaert, G. Ciccotti, and H. J. C. Berendsen, J. Comput. Phys. **23**, 327 (1977).

[77] W. G. Hoover, Phys. Rev. A **31**, 1695 (1985).

[78] We do not observe cystallization at these temperatures in our free standing films. For bulk LW-OTP systems [from U. R. Pedersen, T. S. Hudson, and P. Harrowell, J. Chem. Phys. **134**, 114501 (2011)], crystallization is observed at 250 K and 1.0937 g/cm^3; 260 K and 1.09272 g/cm^3; 275 K and 1.09285 g/cm^3; 370 K and 1.14888 g/cm^3.

[79] J. S. Rowlinson and B. Widom, *Molecular Theory of Capillarity* (Dover, New York, 2002).

[80] W. Smith, Calculating the pressure, Collaborative Computational Projects 5 (CCP5): `http://www.ccp5.ac.uk/ftpfiles/ccp5.newsletters/39/pdf/smith.pdf`, 1993.

[81] D. N. Theodorou, T. D. Boone, L. R. Dodd, and K. F. Mansfield, Makromol. Chem., Theory Simul. **2**, 191 (1993).

[82] A. P. Thompson, S. J. Plimpton, and W. Mattson, J. Chem. Phys. **131**, 154107 (2009).

[83] A. G. McLellan, Proc. R. Soc. London, Ser. A **217**, 92 (1953).

[84] A. Ghoufi, F. Goujon, V. Lachet, and P. Malfreyt, Phys. Rev. E **77**, 031601 (2008).

[85] L. R. Grzyll, C. Ramos, and D. D. Back, J. Chem. Eng. Data **41**, 446 (1996).

[86] R. Fletcher and C. M. Reeves, Computer Journal **7**, 149 (1964).

[87] J. D. Stevenson and P. G. Wolynes, J. Chem. Phys. **129**, 234514 (2008).

[88] M. S. Shell, P. G. Debenedetti, and F. H. Stillinger, J. Phys. Condens. Matter **17**, S4035 (2005).

Chapter 7

Conclusions

In this dissertation, we examined a number of model supercooled and glass-forming systems. The first three studies focused on isotropic systems, and investigated the bulk thermodynamic and dynamic properties of different models: Chapter 2 presented a family of systematically softened potentials based on the well-known Lennard-Jones potential; Chapter 3 provided an analysis on the validity of using relaxation times as a substitute for viscosity when studying Stokes-Einstein violation in simulations; and Chapter 4 investigated the viscosity properties of SPC/E water in the low temperature liquid regime. In contrast, the last two studies focused on the properties of free-standing films: Chapter 5 considers films composed of binary Lennard-Jones atoms, while the films of Chapter 6 consist of Lewis and Wahnström *ortho*-terphenyl molecules. In this concluding chapter, we again summarize the main conclusions of each of these studies, and provide suggestions for future work. Note that the contents of the following sections are the same as the concluding sections in each of the proceeding chapters, and these conclusions are provided here for the convenience of the reader.

7.1 A Family of Systematically Softened Potentials

In Chapter 2 we investigated numerically the structural, thermodynamic and dynamic properties of a family of potentials of variable softness, and fixed well depth and well depth location. In order to explore the low-temperature non-crystalline behavior we considered, for each value of the repulsive exponent, a Kob-Andersen glass-forming binary mixture[1]. Simulations were conducted at a single density, chosen to be high enough to prevent cavitation even for the softer version of the potential investigated here.

Liquid structure, as described by the pair correlation functions, is only moderately sensitive to

constrained variations in softness, and inherent structure radial distribution functions are remarkably insensitive to such a perturbation. In sharp contrast, both dynamics and thermodynamics exhibit marked sensitivity to softness. Upon decreasing the repulsive exponent from 12 to 7, the translational diffusion coefficient increases by as much as two orders of magnitude, and liquids interacting via softer potentials remain diffusive down to appreciably lower temperatures. The average configurational energy per particle is larger in magnitude for the softer ($n = 7$) equilibrium liquid mixture than for the Lennard-Jones ($n = 12$) counterpart by more than two full well depths, reflecting the progressively stronger attractions that ensue upon constrained softening, while satisfying the fixed well depth and location constraints (Figure 2.1). Accordingly, the average inherent structure energies are appreciably more negative for the softer mixtures. The lowest-energy mechanically stable packings (inherent structures) that we were able to form, corresponding to the softer extreme considered here ($n = 7$), possess on average an additional cohesive energy of roughly 1.7 well depths per particle relative to their $n = 12$ counterparts (Figure 2.5). This is a consequence of the stronger attractive energies (more negative attractive tails) at separations greater than the well depth that arise as a result of softening.

Progressive softening also results in an increase in entropy, a decrease in the Kauzmann temperature, and a marked extension towards lower temperatures of the conditions at which equilibrium liquid behavior can be observed. Constrained softening, in other words, leads to enhanced entropy and mobility, more stable particle packings, and diffusive behavior at lower temperatures. We find only a modest increase in fragility upon softening, and in order to uncover this trend it is necessary to use both extrapolated relaxation times and extrapolated characteristic temperatures. This points to the challenge of calculating fragilities by molecular-based computer simulation, a challenge that originates with the difficulty of sampling low enough temperatures.

The rich behavior identified in the course of this research suggests several directions for future work. In light of the contrast of our results with experimental observations for colloidal particles[2] in which softening leads to a progressive decrease in fragility, it would be interesting to extend the present fragility calculations to other densities. This would allow exploration of regimes in which particles sample different regions of their respective pair potentials. More generally, extending the present structural, dynamic and thermodynamic calculations to a broader range of conditions, including low-density states leading to cavitation in the softer models (Figure 2.2), is important in order to acquire a fuller picture of this family of potentials. It is also of interest to explore the possibility of scaling behavior, whereby physical properties for the various models may be collapsed into a single curve by appropriate scaling of temperature and/or density. The pronounced sensitivity

of inherent structure energy to softness (Figure 2.5) may be of relevance in optimization problems, where strategies involving appropriately-chosen cycles of softness perturbations might be useful for locating deep potential energy minima. Other families of models can be formulated, with an eye to introducing similar systematic perturbations of alternative aspects of the interaction potential, such as attractions.

7.2 The Stokes-Einstein Equation in Computational Studies

In Chapter 3, we have examined three variants of the Stokes-Einstein ratio, namely $D\eta/T$, $D\tau$, and $D\tau/T$, for model atomic and molecular systems, over a broad range of temperatures and densities.

For the family of atomic binary systems of variable softness investigated, with τ a structural relaxation time, the ratio $D\tau/T$, based on the approximation $\tau \sim \eta$, increases upon cooling much faster than the true Stokes-Einstein ratio $D\eta/T$. The product $D\tau$, based on the approximation $\tau \sim \eta/T$, exhibits negative Stokes-Einstein violation at moderate temperatures, approaching the true Stokes-Einstein ratio as the repulsive component of the potential becomes progressively steeper. The increase upon cooling exhibited by the three Stokes-Einstein variants occurs at progressively higher temperatures as the fluids are compressed. As can be seen from Figures 3.1 and 3.2, the Stokes-Einstein ratio $D\eta/T$ is constant, to a very good approximation, over a broad range of thermodynamic conditions.

The molecular system we studied, the Lewis-Wahnström model of OTP, exhibits similar behavior, with one important difference: the product $D\tau$ is a reasonably accurate proxy for the Stokes-Einstein ratio across the conditions investigated here, and does not show negative violation of Stokes-Einstein behavior. This is consistent with the trend observed in the atomic systems, where the approximation $\tau \sim \eta/T$ gets better as the close range repulsion becomes steeper, since this OTP model consists of three Lennard-Jones sites connected by rigid bonds. For this system, too, $D\eta/T$ = constant is satisfied over an appreciable range of thermodynamic conditions: $300 \leq T \leq 400$ K at 1.0746 g/cm^3 and $280 \leq T \leq 400$ K at 1.0578 g/cm^3.

Different choices of relaxation times can affect the behavior of the Stokes-Einstein variants in non-trivial ways. In this work we considered two relaxation times. One, denoted simply by τ in this paper, is a structural relaxation time obtained from the decay of the self-intermediate scattering function; the other, τ^{GK}, is a stress relaxation time obtained from the Green-Kubo stress autocorrelation integral. While both relaxation times lead to similar behavior for the atomic binary mixtures, especially for the softer potentials, for the OTP system τ^{GK} leads to negative Stokes-Einstein violations

in $D\tau^{GK}$, in contrast to $D\tau$ which does not show negative violations. Furthermore, the relationship between these two relaxation times displays a non-trivial temperature dependence, especially at low temperatures.

The often-invoked simple proportionality between viscosity and relaxation time is predicated on the assumed constancy of the instantaneous shear modulus, G_∞. Our numerical study of this quantity based on the Green-Kubo formalism reveals an appreciable temperature dependence for the two classes of systems investigated here, and G_∞ increases with temperature for both the atomic binary mixtures and OTP.

In this study, we have explored the effects of temperature changes under constant density conditions. Most experiments, on the other hand, are performed under isobaric conditions. It would be interesting to investigate numerically the extent to which the main observations reported here remain valid under the more experimentally-relevant isobaric conditions. Recent experiments suggest that in some glass-forming alloys the product $D\eta$ is constant while Stokes-Einstein violation occurs[3]; it would be interesting to explore computationally the extent to which this scaling applies more broadly to other systems.

The present calculations suggest that commonly-invoked assumptions, such as $\tau \sim \eta$ and $\tau \sim \eta/T$, deserve critical scrutiny when used to construct Stokes-Einstein variants. The behavior of $D\eta/T$, $D\tau$ and $D\tau/T$ needs to be investigated for a wider range of systems than the two considered here, and across as broad a range of temperatures and densities as possible. It is also of interest to explore numerically the behavior of different relaxation times, only two of which have been considered here. It is hoped that such systematic numerical investigation will lead to a deeper understanding of relaxation processes in liquids at both supercooled and ambient conditions. Our approach in this work has been phenomenological. Numerical studies of the microscopic mechanisms underlying the rich behavior presented here constitute a natural direction for future studies.

We wish to stress in closing the remarkably broad range of conditions across which the Stokes-Einstein equation, meant to apply to supermolecular objects suspended in a fluid continuum, is also valid at the molecular level.

7.3 Anomalies of Water: Viscosity and Stokes-Einstein Violation

We presented in Chapter 4, to our knowledge, the first comprehensive analysis of viscosity for SPC/E water over a wide range of thermodynamic conditions. At low enough temperatures, we observe anomalous behavior, where viscosity *decreases* upon compression. When mapped onto the (ρ, T) plane, the region of the viscosity anomaly is comparable to that of diffusivity, and both of these regions are contained within the region of structural anomalies. This suggests that in the anomalous region for viscosity and diffusivity, the mobility increase is caused by pressure-induced distortions of the hydrogen bond network.

We also investigated the Stokes-Einstein behavior for this system. Similar to many liquids, at higher temperatures, SPC/E water is well described by the Stokes-Einstein equation, while at low enough temperatures strong violation is observed. However, the temperature at which violation occurs exhibits anomalous behavior, as for the density range $0.9 \leq \rho \leq 1.15$ g/cm^3, the onset temperature of violation *decreases* upon compression.

We observe anomalous behavior for both the structural and stress relaxation times, which occurs at similar state conditions as the viscosity and diffusivity anomalies. When used as a substitute to study Stokes-Einstein behavior, the relaxation times based upon $\tau \propto \eta/T$ and $\tau^{GK} \propto \eta$ are reasonable approximations for η at high and low temperatures, respectively. However, neither structural or stress relaxation times adequately describe the true Stokes-Einstein behavior over the full temperature range explored in this investigation. We also find that no trivial proportionality exists between τ and τ^{GK}. These results reinforce those of Chapter 3, and further demonstrate that the structural relaxation time and the stress relaxation time are distinct quantities, and are not equivalent or interchangeable.

For our study, we used the SPC/E model of water, one of the many molecular water models currently available for use in computer simulations. While SPC/E shows prominently the structural, kinetic, and thermodynamic anomalies of water, it would be useful to compare the anomalous domains of various water models. When considered together with the results of the earlier study by Errington and Debenedetti[4], the region of anomalous behavior for kinetic processes (viscosity, diffusivity, and relaxation times) is consistently contained within the region of structural anomalies, suggesting that the anomalous increase in mobility upon compression is the result of the distortion of the tetrahedral hydrogen bond structure. Although we can understand the relationship between the structural and kinetic anomalies, the relationship of these anomalies to the corresponding ther-

modynamic anomaly is a topic of active ongoing investigation[5], and provides a natural direction for future studies.

7.4 Model Free-Standing Films

In Chapters 5 and 6 we investigated the properties of free-standing films. The 80%(A)-20%(B) binary Lennard-Jones glass-forming mixture considered in Chapter 5 exhibits substantial compositional inhomogeneity, with weaker A-A interactions favored at the free surface and stronger A-B contacts favored inside the film. This preferential enrichment of surface and "bulk" in A and B, respectively, reflects primarily the energetics of free surface stabilization. Over the range of temperatures explored herein, we observe a substantial enhancement of lateral mobility at the surface with respect to the film's interior. In agreement with theoretical predictions[6], particles residing at the free surface are able to descend deeper down the energy landscape than particles in the film's interior. Since the difference between equilibrium and inherent structure energy should be independent of position for a harmonic system, this behavior is an indication of the strong basin anharmonicity introduced by the free surfaces.

In Chapter 6, we investigated the properties of films composed of model rigid molecules. We used a three site model of OTP constrained by rigid bonds. Compared to the atomic binary Lennard-Jones case[7], the film is more cohesive, with no molecules ever being ejected into the vapor phase at $T \leq 300\ K$. We do, however, observe a higher mobility of the molecules near the surface of the film when compared to the bulk. Furthermore, as we approach the surface from the bulk, the rate of increase in translational and rotational diffusivity become decoupled, suggesting the presence of dynamic heterogeneities[8] in the system. We also observe a similar inherent structure energy difference profile when compared to the binary Lennard-Jones study, which again suggests that particles residing at the free surface are able to descend deeper down the energy landscape than particles in the film's interior. One notable different feature with respect to the atomic study is the dampened oscillatory center-of-mass density profile. This oscillatory behavior is also evident in the average orientation of molecules within the film. Given a characteristic interfacial width w, the orientational oscillations are noticeable until a depth of $1.5w$ into the film's interior. This strongly suggests that the orientational ordering of molecules, while induced by the presence of an interface, extends well below the interface.

It would be interesting to investigate whether this "sub-surface region" of surface-induced ordering, and the decoupling of translation and rotational diffusion, appear in films composed of other

non-spherical molecules, such as rod-like molecules or chains. Additionally, it would be useful to understand how this orientational ordering applies to surface effects observed experimentally. Finally, most experiments are conducted on supported films, whereas our simulations have so far explored free-standing films. We believe it is important to understand the effects of a substrate on the dynamic and structural phenomena reported in these two chapters.

Bibliography

[1] W. Kob and H. C. Andersen, Phys. Rev. E **51**, 4626 (1995).

[2] J. Mattsson *et al.*, Nature **462**, 83 (2009).

[3] J. Brillo, A. I. Pommrich, and A. Meyer, Phys. Rev. Lett. **107**, 165902 (2011).

[4] J. R. Errington and P. G. Debenedetti, Nature **409**, 318 (2001).

[5] J. R. Errington, P. G. Debenedetti, and S. Torquato, Phys. Rev. Lett. **89**, 215503 (2002).

[6] J. D. Stevenson and P. G. Wolynes, J. Chem. Phys. **129**, 234514 (2008).

[7] Z. Shi, P. G. Debenedetti, and F. H. Stillinger, J. Chem. Phys. **134**, 114524 (2011).

[8] M. S. Shell, P. G. Debenedetti, and F. H. Stillinger, J. Phys. Condens. Matter **17**, S4035 (2005).